

Cosmic Infrared Background Fluctuations in Deep *Spitzer* IRAC Images: Data Processing and Analysis

Richard G. Arendt^{1,2,3}, A. Kashlinsky^{1,2}, S. H. Moseley^{1,4}, J. Mather^{1,4}

ABSTRACT

This paper provides a detailed description of the data reduction and analysis procedures that have been employed in our previous studies of spatial fluctuation of the cosmic infrared background (CIB) using deep *Spitzer* IRAC observations. The self-calibration we apply removes a strong instrumental signal from the fluctuations which would otherwise corrupt our results. The procedures and results for masking bright sources, and modeling faint sources down to levels set by the instrumental noise are presented. Various tests are performed to demonstrate that the resulting power spectra of these fields are not dominated by instrumental or procedural effects. These tests indicate that the large scale ($\gtrsim 30'$) fluctuations that remain in the deepest fields are not directly related to the galaxies that are bright enough to be individually detected. We provide the parameterization of these power spectra in terms of separate instrument noise, shot noise, and power law components. We discuss the relationship between fluctuations measured at different wavelengths and depths, and the relations between constraints on the mean intensity of the CIB and its fluctuation spectrum. Consistent with growing evidence that the $\sim 1 - 5 \mu\text{m}$ mean intensity of the CIB may not be as far above the integrated emission of resolved galaxies as has been reported in some analyses of DIRBE and *IRTS* observations, our measurements of spatial fluctuations of the CIB intensity indicate the mean emission from the objects producing the fluctuations is quite low ($\gtrsim 1 \text{ nW m}^{-2} \text{ sr}^{-1}$ at $3 - 5 \mu\text{m}$), and thus consistent with current γ -ray absorption constraints. The source of the fluctuations may be high- z Population III objects, or a more local component of very low luminosity objects with clustering properties that differ from the resolved galaxies. Finally, we discuss the prospects of the upcoming space-based surveys to directly measure the epochs inhabited by the populations producing these source-subtracted CIB fluctuations, and to isolate the individual fluxes of these populations.

Subject headings: cosmology: observations — diffuse radiation — early universe

¹Observational Cosmology Laboratory, Code 665, Goddard Space Flight Center, 8800 Greenbelt Road, Greenbelt, MD 20771; Richard.G.Arendt@nasa.gov, Alexander.Kashlinsky@nasa.gov, Harvey.Moseley@nasa.gov, John.C.Mather@nasa.gov

²Science Systems & Applications Inc.

³University of Maryland – Baltimore County

⁴NASA

1. Introduction

The cosmic infrared background (CIB) is comprised of radiation emitted throughout the entire history of the Universe (e.g. Bond, Carr & Hogan 1986). The CIB contains emission from objects which may be too faint to be individually detected or too numerous to be individually resolved with current (or even future) instruments. However, since the collective emission is detectable, the CIB provides unique information on the history of the Universe at very early times. Analogous to studying the brightness and structure of individual galaxies in which the stars cannot be resolved, in recent years we have witnessed new CIB measurements identifying and constraining both its mean level (isotropic component) and spatial fluctuations (see Kashlinsky 2005a for a recent review). The near-IR CIB (hereafter taken to span wavelengths from $1 - 10\mu\text{m}$) probes stellar emission, whereas at longer wavelengths the CIB is generated by dust. Foregrounds, such as Galactic stars, interstellar dust emission (cirrus), zodiacal light, and atmospheric emission, represent formidable obstacles to isolating the true CIB (see review by Leinert et al 1998). Significant progress in CIB research was made possible due to dedicated space experiments conducted by COBE/DIRBE (Hauser et al. 1998; see review by Hauser & Dwek 2001) and *IRTS* (Matsumoto et al. 2005).

Theoretically, the most plausible candidates for the bulk of the near-IR CIB are evolving stellar populations in galaxies. These nucleosynthetic energy sources would include the first generation of stars, known as Population III. A fraction of the CIB must also be generated by accretion onto black holes in active galactic nuclei (AGN) rather than by stellar nucleosynthesis. It is now thought that the first stars were very massive (see review by Larson & Bromm 2004), in which case theoretical models indicate they may produce a detectable contribution to the mean level of the near-IR CIB (Santos et al. 2002, Salvaterra & Ferrarrra 2003; Kashlinsky 2005b, Dwek, Arendt & Krennich 2005, Fernandez & Komatsu 2005). They are also expected to have left a measurable imprint in CIB anisotropies (Cooray et al. 2004, Kashlinsky et al. 2004). The intuitive reasons why these fluctuations would be significant are: 1) if massive, such stars would emit at light to mass ratios $\sim 10^4 - 10^5$ higher than the present-day stellar populations leading to significant CIB flux levels; 2) assuming that the Pop III era occupied a comparatively narrow epoch in time (say $\Delta t \sim$ a few hundred million years) there should be a higher amplitude of relative CIB fluctuations ($\propto 1/\sqrt{\Delta t}$); and 3) it is expected that within the framework of the concordance Λ CDM model the first stars formed out of rare high peaks of the underlying density field and, hence, their correlation properties would be amplified. The CIB fluctuations from such early populations are distinguishable from those produced by more recent populations. Their spatial spectrum should reflect the Λ CDM matter spectrum rising to a peak at $\sim 0.3^\circ - 0.5^\circ$ and its spectral energy distribution should be cutoff due to the Lyman break at wavelengths $\lesssim 1[(1+z)/10]\mu\text{m}$ (Cooray et al. 2004, Kashlinsky et al. 2004).

Present measurements of the mean CIB levels are based on the DIRBE and *IRTS* data and suggest a substantial excess over the contribution from known galaxy populations (Dwek & Arendt 1998, Gorjian et al. 2001, Arendt & Dwek 2003, Matsumoto et al. 2005). This excess of $\sim 30 \text{ nW m}^{-2} \text{ sr}^{-1}$ at $\lambda \gtrsim 1\mu\text{m}$ (Kashlinsky 2005a) is commonly known as the NIRBE (Near-IR Background

Excess). If produced by the first massive stars, it is proportional to the fraction of baryons processed through these stars; a fraction of $\sim 2 - 4\%$ is necessary to explain the levels claimed in the above studies. On the other hand, much of this excess may be due to inaccurate zodiacal light modeling (Dwek et al. 2005) and the remaining NIRBE may be much smaller, in agreement with the recent analysis of the deep *HST* NICMOS data at $1.6 \mu\text{m}$ (Thompson et al. 2007a). Further limits on the CIB come from the amount of photon absorption at γ -ray energies in blazars at moderate $z \sim 0.2$ (Dwek et al. 2005, Aharonian et al. 2005). However such limits are sensitive to the assumptions on the intrinsic unabsorbed blazar spectrum and the fine details of the CIB spectral distribution (Kashlinsky & Band 2007); they are discussed later in the paper.

At certain wavelengths CIB fluctuations can be more readily measurable than the mean levels. As differential rather than absolute measurements, the study of fluctuations places different requirements on instrument capabilities and calibration, and on the precision of removal of foreground emission (zodiacal and Galactic). Shectman (1974) applied fluctuations analysis to constrain the diffuse light in the optical bands. Kashlinsky et al. (1996a,b) have pioneered such studies in the IR using DIRBE data with a further analysis by Kashlinsky & Odenwald (2000) isolating the degree-scale CIB fluctuation at $1-5 \mu\text{m}$. The *IRTS* results on CIB fluctuations at $\sim 2 \mu\text{m}$ agree with the latter study and extend to larger angular scales (Matsumoto et al. 2005). Because of their wide beams the DIRBE- and *IRTS*-based data sets did not allow the removal of many foreground galaxies and the isolation of the contribution from fainter sources. Using ground-based deep 2MASS measurements in the J,H,K photometric bands enabled removal of galaxies to $m_{\text{Vega}} \sim 18 - 19$ and led to detecting the CIB fluctuations signal from galaxy populations below that magnitude threshold on subarcminute scales (Kashlinsky et al. 2002, Odenwald et al. 2003). However, all of these studies involved data sets with either low angular resolution and/or relatively shallow integrations so that the CIB fluctuations from the remaining galaxies and instrument noise prevented isolating any signal arising from the first stars epochs.

In the past several years we have used deep-integration *Spitzer* data to measure the CIB fluctuations component (Kashlinsky, Arendt, Mather & Moseley 2005, 2007a,b,c - hereafter KAMM1, KAMM2, KAMM3, KAMM4). They revealed significant CIB fluctuations at the IRAC wavelengths (3.6 to $8 \mu\text{m}$) which remain after removing galaxies down to very faint levels (KAMM1, KAMM2). These fluctuations must arise from populations that have a significant clustering component, but only low levels of shot noise (KAMM3). Furthermore, it was shown that there are no correlations between source-subtracted IRAC maps and the corresponding fields observed with the *HST* ACS at optical wavelengths (KAMM4), which means that the sources producing these CIB fluctuations are *not* in the ACS source catalog extending to $m_{\text{AB}} \lesssim 28$ at wavelengths $\lesssim 0.9 \mu\text{m}$.

KAMM found statistically significant cross-correlations between the different IRAC channels, indicating the presence of a common component in all the channels, and determined the color of unresolved fluctuations (KAMM1). Their analysis allowed the separation of various noise and systematic effects individually in each IRAC channel (KAMM1, KAMM2), thus characterizing the statistical uncertainties and systematic errors in fluctuation measurements. The results were

further verified with simulated patterns of first star galaxies (KAMM1). The simulations recovered the input fluctuations and established the good accuracy of the determined diffuse backgrounds in the assembled images. These techniques directly showed that our existing procedure based on Fourier transforms *and* correlation function analysis does not lead to biased estimates of the CIB fluctuations (see also Kashlinsky 2007).

In this paper we describe, illustrate, and further verify many details of our analysis efforts. In §2, we describe the *Spitzer* data sets we have analyzed and the self-calibration procedures we have applied in order to generate maps with accurate large scale structure. Section 3 details the steps used in the analysis of the power spectra of the backgrounds. Section 4 illustrates the extent to which the derived CIB power spectra depend on the details of the analysis steps, particularly the masking and removal of resolved foreground sources. Section 5 discusses the results, with future prospects described in Section 6. The paper concludes with a summary (§7).

2. Data Processing and Mosaic Construction

In this section we present the steps taken to process the individual frames of IRAC data into integrated mosaicked images for each field, wavelength and epoch (see also the Supplementary Information of KAMM1). This is the first stage of the overall data processing and analysis which is shown schematically in Figure 1. Discussion of the effects that the data reduction may have on the results, and of the comparison of results between different fields and different epochs is deferred to §4, after we present the analysis procedures in §3.

2.1. *Spitzer's* Infrared Array Camera (IRAC)

Our research has used data from *Spitzer's* IRAC instrument. This camera contains two parallel optical systems. Each system images a separate $5' \times 5'$ field of view, with the fields separated by $\sim 6'$. Using beam splitters, each optical system collects images in two channels (at two wavelengths) simultaneously. So while one field of view is being observed at 3.6 and 5.8 μm , a nearly adjacent field is being observed at 4.5 and 8 μm . The detector for each channel is a 256×256 pixel array, with a scale of $\sim 1.2''/\text{pixel}$. This pixel scale slightly undersamples the instrument point spread function at the shortest wavelengths. The paper by Fazio et al. (2004a) is the primary description of the IRAC instrument. Many other details are contained within the *Spitzer* Observer's Manual and the IRAC Data Handbook, which are found on the *Spitzer* Science Center website.¹

Normal observing procedures entail dithering the telescope pointing between successive exposures or frames. Altering the pointing by various fractions of the array size prevents any detector

¹<http://ssc.spitzer.caltech.edu>

defects (e.g. bad pixels) from completely eliminating data from a particular point on the sky. Dithering also serves to alter the pattern of stray light artifacts (most prominently occurring near bright sources that lie just outside the field of view). Most importantly, dithered data can be used to derive the relative detector offsets (and gains) as the sky itself can serve as a stable relative calibration source. Mapping fields larger than the instantaneous $5' \times 5'$ field of view is usually done by stepping through a rectangular grid of $N \times M$ positions separated by $\lesssim 5'$, with many dithered frames collected at each raster position. Because of the offset between the two instrument fields of view, the overall coverage at 3.6 and 5.8 μm is displaced from that at 4.5 and 8 μm by $\sim 6'$. In some programs, the field is re-observed after 6 months have elapsed. At that time the relative locations of the two fields of view are transposed, and thus if both epochs of data are combined then the same area can be covered equally in all four channels (wavelengths).

The properties of the IRAC data sets we have examined are listed in Table 1.

2.2. IOC Deep Image = QSO 1700 Field

The IRAC IOC Deep Image observations were a test to verify that a deep (close to confusion-limited) integration could detect moderately high redshift sources. They were also intended to verify that the noise in an image would scale inversely with the square root of the integration time, even for very deep integrations. A secondary goal of these observations was to investigate the effects of different dither patterns and observing strategies on the results. Analyses of the resolved sources in this field have been published by Fazio et al. (2004b) and Barmby et al. (2004).

The nominal target field for these observations was a field including the quasar HS 1700+6416 and several known Lyman break galaxies. Each channel observed a $\sim 11' \times 5'$ field, or 2×1 IRAC fields of view. The field observed at 3.6 and 5.8 μm only overlaps with the field covered at 4.5 and 8 μm in a $5' \times 5'$ region. The dithering used during the observations extended the coverage over a wider region than the $\sim 5' \times 5'$ IRAC field of view, but this coverage is at a lower depth than the center of the field.

Scheduling constraints required that the observations be broken up into several astronomical observation requests (AORs), so each AOR employed a different dithering or coverage strategy. The observations were carried out over an interval of less than 2 days. Therefore any changes in the zodiacal light were small, e.g. the 8 μm zodiacal light intensity changes from 4.595 MJy sr^{-1} to 4.600 MJy sr^{-1} between the start of the first and last AORs according to the Spitzer Science Center’s zodiacal light model.

At the time we began this project (KAMM1), the basic calibrated data (BCD) pipeline was not so well developed, and calibration observations had not been accumulated over a long enough time to provide the best flat field and dark frame calibration. Therefore we performed our own data reduction beginning with the raw data. We applied the least-squares self-calibration procedure as described by Fixsen, Moseley & Arendt (2000). The approach formalizes the calibration procedure

by describing the data with a model whose parameters include both the detector characteristics and the true sky intensity. The derivation of the model parameters via a least-squares algorithm yields an optimal solution for the calibration and the sky intensity. In this case our chosen model is given by

$$D^i = S^\alpha G^p + F^p + F^q \quad (1)$$

where D^i represents the raw data from a single pixel of a single frame, S^α is the sky intensity at location α , G^p and F^p are the gain and offset for detector pixel p , and F^q is a variable offset for each of the 4 readouts (alternate vertical columns of the detector) and each frame. This model assumes that the sky intensity (S^α) and the detector gains and offsets (G^p and F^p) are invariant during the course of the observations. For a data set with fixed frame times (as our IRAC data), the detector dark current is included in the F^p term as it is indistinguishable from an offset. For data sets with multiple frame times, a relatively simple extension of this data model could be applied. The variable offset F^q can absorb time-dependent behavior of the detector, but only to the extent that it can be characterized with a single value frame, or in some cases, a single value per readout per frame.

In order to be able to self-calibrate the raw data for both gain and offset effects, the procedure requires a higher intensity contrast than is found in the QSO 1700 data alone. Therefore additional AORs taken at low ecliptic latitude (and hence high zodiacal brightness) were combined with the IOC Deep Image AORs for the self-calibration. Ideally, these “hizodi” observations would have been performed just before or after the QSO 1700 observations. However in fact, the nearest suitable 200-sec frame time data for Channels 1 – 3 (3.6 – 5.8 μm) were observed over a month later, although suitable 100-sec (2 \times 50sec) frame time data for Channel 4 (8 μm) were observed shortly prior to the QSO 1700 AORs.

The self-calibration was initially applied to each of the QSO 1700 AORs (combined with the hizodi AOR) separately. However, as variations proved to be relatively small, our final results were obtained by running the self-calibration on the complete set of 200-sec frame time data at each wavelength. In the case of the 8 μm data, which used four 50-sec frames for each 200 sec frame in the other channels, we self-calibrated the data in 4 subsets, which were combined as a weighted average of the resulting mosaics.

After the derived gain and offset calibrations are applied to the individual frames and before they are mosaicked, each frame at 3.6 and 4.5 μm is corrected for the “column pulldown” effect in the columns of bright point sources (see the IRAC Data Handbook) using a version of the algorithm that is available from the SSC as a user-contributed tool². For 8 μm frames we applied a similar correction of our own development to correct for the “banding” artifact which affects detector rows containing bright sources. No artifact correction was applied for 5.8 μm data, as its banding is less severe than at 8 μm , and it is not substantially improved by our procedure. We have also not made

²<http://ssc.spitzer.caltech.edu/irac/pulldown/>

any extra corrections for 3.6 and 4.5 μm muxbleed artifacts (see the IRAC Data Handbook), which appear as a decaying excess intensity in consecutive detector pixels sampled by a readout after sampling a very bright (saturated) source (i.e. in every 4th pixel of a detector row following the saturated source). Because the muxbleed effect is strictly periodic, i.e. a shah function (Bracewell 1986) in the spatial domain, it transforms to another shah function in the frequency domain. Thus excess power is found at the fundamental frequency (0.25 pixels^{-1}), and at the first harmonic which corresponds to the Nyquist frequency (0.5 pixels^{-1}). These spikes are evident at spatial scales of $\sim 4.8''$ and $\sim 2.4''$ in the power spectra which are shown below. The slow decay of the muxbleed effect transforms to a slight broadening of the spikes in the power spectra. Power at these scales is not important to the present research, in which the primary signal of interest is found at scales $\gtrsim 40''$.

This first step in the overall data processing flow is indicated in Figure 1. Subsequent processing steps of source modeling and source masking (see §3), will additionally affect the photometry of the images to be analyzed.

Continued improvements to the BCD pipeline since the KAMM1 analysis now allow good results when starting with the BCD (or corrected BCD, cBCD) rather than the raw data. Verification that similar power spectra are derived from either data set is presented in §4.3.

2.3. Extended Groth Strip

The Extended Groth Strip observations are part of a large extragalactic GTO project (Spitzer Program ID number 8). The full observations cover a $10' \times 125'$ region with a depth of 26 200-sec frames (1.4 hr), repeated after a 6-month interval. The data are well-dithered for our purposes, using the medium-scale cycling pattern³, which is based on a 2-dimensional gaussian distribution ($\sigma = 32 \text{ pixels}$) of dither positions with a maximum offset of 119 pixels $\approx 145''$. Our data reduction did not include the full data set, but only two $10' \times 5'$ portions of the strip, at both epochs. Data from the two epochs were reduced separately.

The data reduction was similar to that described above for the QSO 1700 field, except that for these data (and all subsequent data sets) our analysis began with the individual BCD frames rather than the raw data. If an imperfect calibration, designated by $\{G'^p, F'^p, F'^q\}$ is applied to the raw data, D^i , then equation (1) becomes

$$\frac{D^i - F'^p - F'^q}{G'^p} = \frac{S^\alpha G^p + (F^p - F'^p) + (F^q - F'^q)}{G'^p} \quad (2)$$

$$D_{\text{BCD}}^i = S^\alpha + \frac{S^\alpha \delta G^p + \delta F^p}{G'^p} + \frac{\delta F^q}{G'^p} \quad (3)$$

$$D_{\text{BCD}}^i = S^\alpha + \Delta F^p + \Delta F^q \quad (4)$$

³<http://ssc.spitzer.caltech.edu/irac/dither.html>

where D_{BCD}^i is the BCD data, $\delta G^p \equiv G^p - G'^p$, $\delta F^p \equiv F^p - F'^p$ and $\delta F^q \equiv F^q - F'^q$. In the last equation we make the approximations that $S^\alpha \sim \text{constant}$ so that we can ignore any dependence of ΔF^p on α , and that $G'^p \sim \text{constant}$ so that we can ignore any dependence of ΔF^q on p . Thus the “delta corrections” to be derived and applied to the BCD data can be represented as simple offset terms, as in equation (1), but now without a gain term in the equation. The data model that is applied when starting with the IRAC BCD frames can be represented as a slight variation on equation (1):

$$D^i = S^\alpha + F^p + F^q . \quad (5)$$

With no gain term, this model has the advantage that no contrasting data set (e.g. the high zodiacal brightness field used with the QSO 1700 data) is required to separate degeneracies between gain and offset. Any true gain errors that are present in the BCD data will be absorbed in the offset term F^p , by assuming that S^α is constant. The size of the errors made by approximating gain errors as offset errors are of order $\delta S^\alpha \delta G^p$ in a single BCD frame, where $\delta S^\alpha \equiv S^\alpha - \langle S^\alpha \rangle$. The errors are reduced further by the square root of the number of dithered frames (\sqrt{N}) at each location ($N > 100$ frames for the deeper GOODS and QSO 1700 fields). The fluctuations, δS^α , in the dominant zodiacal light and cirrus foregrounds are already estimated to be at or below the residual fluctuations (see Figure 1 of KAMM1). Further reduction of these fluctuations by factors of δG^p ($< 1\%$, IRAC Data Handbook) and $1/\sqrt{N}$ means that the approximation of gain errors as offset errors only affects results at levels $\ll 1\%$ of the detected signal. We note that the approximation would be more problematic if we were interested in accurate photometry of the brighter resolved sources, for which δS^α would be very large.

2.4. GOODS HDFN and CDFS

The GOODS Legacy program (Program ID numbers 169 & 194) is designed to obtain very deep, confusion-limited observations over small ($10' \times 15'$) fields. The chosen fields are the Hubble Deep Field – North (HDFN) and the Chandra Deep Field – South (CDFS), which is also the location of the Hubble Ultra Deep Field.

These observations also used 200-sec frame times, and were carried out at two epochs separated by ~ 6 months. At the first epoch (HDFN-e1, CDFS-e1), the two IRAC fields of view cover partially overlapping $10' \times 10'$ fields. At the second epoch (HDFN-e2, CDFS-e2) the IRAC fields of view are reversed, thus providing complementary coverage.

For each channel, the BCD frames of each of the ~ 20 AORs were processed separately to determine preliminary calibration factors, F_1^p and F_1^q . Maps made from these calibrated data would show large systematic errors because there is no constraint between the AORs to produce the same mean sky intensity. Therefore, at each epoch, we also performed the self-calibration on the entire data set, but after downsizing the data set by performing 2×2 pixel-averaging on each BCD frame (resulting in 128×128 pixel frames). The derived calibration parameters F_2^p and

F_2^q produce consistency across the entire data set, but with limited spatial resolution and with averaging over some real temporal variations (between AORs) in the detector offsets (F_2^p). Thus, we calibrated the frames of each AOR using $F^p = F_1^p + \nabla(F_2^p - F_1^p)$ and $F^q = F_2^q$, where $\nabla(F_2^p - F_1^p)$ is the 2-dimensional linear gradient in the difference between the derived detector offsets. This combines the individual detail of the detector offsets (F_1^p) derived for each AOR, with the overall consistency provided (via F_2^q) by simultaneous self-calibration of all AORs.

2.5. Extragalactic First Look Survey

The Extragalactic First Look Survey (FLS; Program ID number 26) is a shallow survey covering a $2^\circ \times 2^\circ$ field. Observations used 12-sec frame times with a depth of 5 exposures dithered with the small-scale Gaussian pattern. These data were examined to explore larger spatial scales than the deeper data sets, despite the fact that the depth and the dithering are not especially well-suited for self-calibration.

2.6. Final Images

For each of the data sets described above we mapped the artifact-corrected and self-calibrated BCD frames into final mosaics. The mapping procedure we used is an interlacing algorithm, where each pixel of the BCD frame is mapped into the pixel in the sky map that contains the center of the BCD pixel. This is similar to a drizzle algorithm with the “pixfrac” parameter set to zero (Fruchter & Hook, 2002). A desirable aspect of this mapping procedure is that it does not induce any pixel-to-pixel correlations in the noise, which does occur with procedures that map the flux of a single input pixel into multiple sky map pixels. Another asset of this procedure is that it can easily create sky maps with pixel scales and orientations that are independent of the scale and orientation of the detector pixels. In general we prepared several variations of the final images. The most basic images are generated by mapping the entire data set into images with a scale of $1''/2/\text{pixel}$ (the detector pixel scale). For the deeper data sets, we also produced images with scales of $0''/6/\text{pixel}$. This allows slightly better discrimination of resolved point sources. For the GOODS and EGS data sets, the data from each epoch (~ 6 months apart) were mapped into separate images. These images are useful as a check for systematic errors. Finally, for all data sets we created “A” and “B” images by mapping all the even numbered frames from the sequence of exposures into the “A” image, and the odd numbered frames into the “B” image. Any systematic errors should be manifested very similarly in the A and B images, and thus the (A-B)/2 difference images provide a useful means of characterizing the random (noise) properties of the data sets.

3. Fluctuation Analysis

In this section we present the analysis procedures that are applied to the mosaicked IRAC images to derive the power spectra of the background. The analysis consist of two main parts: (1) removal of individually resolved sources via modeling and masking, and (2) calculation of the power spectra of the remaining background. These stages are shown in the overall data processing and analysis schematic flow chart in Figure 1. For clarity, this section is restricted to a direct description of the processes. There are several aspects of the analyses which can have significant effects on the results. Tests of the effects that these processing details have on the final derived power spectra will be presented in §4.

3.1. Source Removal

In order to study the spatial fluctuations of the unresolved extragalactic background emission, we must have a means of removing or ignoring the influence of the brighter, resolved galaxies and foreground stars. One such method is that the sources can be individually fit with a model and subtracted. Practical difficulties with this approach are (a) limitations in the accuracy of the point response functions⁴ (PRFs), and (b) limitations in the modeling of sources that have resolved extended structure. Small fractional errors in the PRF or source model can result in large residuals at very bright sources. Furthermore, the power spectrum of the residuals can exhibit different behavior than the power spectra of the original sources or the PRF. A complementary approach is to mask the bright resolved sources in the images. Depending on the type of analysis to be performed, the masked regions can either be ignored (e.g. when computing correlation functions) or else filled with zeros or noise at the appropriate level (e.g. when computing power spectra). The difficulties in the masking approach are (a) for deep observations, masking all resolved sources including their extended wings (both due to the PRF and any extended emission) can leave little or no data left for analysis, and (b) the masking will likely alter the shape of the calculated power spectrum of the image.

In our studies, we apply both techniques. A source modeling procedure is used to ensure that the faintest resolved point sources and extended sources are removed from the images. Masking is then applied to eliminate artifacts in the modeling and subtraction of only the brighter emission, thus minimize the influence of the masking on the power spectra. These steps are shown schematically in Figure 1.

⁴The PRF includes the sampling of the detector pixels as well as the point spread function (PSF) which describes the light incident at the surface of the detector. Description of the IRAC PRF, and the most current PRFs, are found at: <http://ssc.spitzer.caltech.edu/irac/psf.html>.

3.1.1. Source Modeling

Our source modeling procedure is conceptually similar to the CLEAN algorithm, which is used to remove the effects of beam sidelobes in radio images (Högbom 1974). We start with the original image and a corresponding model image which is set to zero. The first step is to locate the brightest pixel in the original image. At that location, we subtract the IRAC PRF, normalized such that the peak is a specified fraction f of the pixel intensity. We *add* the same scaled PRF to the corresponding location in the model image. This process is iterated by locating the brightest pixel in the modified image. The scaled PRF is again subtracted from the image and added to the model. Because only a fraction f of a source (a “component”) is subtracted at each iteration, even a point source is modeled by multiple components. The residual flux of an ideal point source, matched by the PRF, will be proportional to $(1 - f)^n$ after subtraction of n components. For our analysis we used $f = 0.5$, as a compromise between speed (high values of f) and insensitivity to any PRF errors (low values of f ; discussed below). So for the faintest sources, the residual emission of the point source is lost in the noise with $n = 2 - 3$. Whereas for bright sources, several dozen components may be needed to reach the same level of residual emission. The loop of finding and subtracting components is repeated on order of 10^4 times, depending on the number of resolved sources, the size of the image, and the value of f . The total number of iterations is chosen so that the brightest pixels left in the image are approximately at the 3σ noise level. We save the model after every $\sim 10^3$ iterations, so that we have a series of ~ 10 models at various depths. These can be examined afterwards to determine how the model-subtracted image varies as a function of model depth, and determine the optimal model depth.

There are several important details to be noted in the modeling procedure. First is that the noise level is not completely uniform across the original image. Therefore, we actually model an image that is weighted by the exposure depth, which produces an image with flat noise properties. This is equivalent to searching for the most significant, rather than the brightest, pixel in the image at each iteration. The model thus produced needs to be deweighted before subtraction from the data. The second important detail is that the choice of PRF can be important. If the model PRF is sharper (narrower) than the actual PRF, then a point source will behave as an extended source, requiring subtraction of multiple components at slightly different positions, and thus the overall number of iterations would need to be increased. Despite being slower, a good result should still be attained. If the model PRF is too wide, however, the emission from point sources will be oversubtracted immediately around the source. This error is not recoverable, as we only are fitting components to the most significant positive pixels. Because we are interested in faint background fluctuations, it is also important that our modeling procedure uses PRFs that map the IRAC beam out to large angular distances, i.e. that it include the extended wings of the PRF. If the wings are not included in the model PRF, then the actual wings of sources in our image will not be modeled and removed, and may provide an undesired contribution to the power spectrum. The PRF used in these studies was described in the in the Supplementary Information of KAMM1. It consists of the core PSF (measured out to a radius of $12''$) which was made available by the SSC

following the in-orbit checkout (IOC), combined with the broad wings (measured out to $\sim 150''$) that were observed in long frame time observations of Fomalhaut (AORID = 6066432). Tests on the sensitivity of the power spectra to details of the adopted PRF are presented in §4.2. The third detail of the procedure is that it is important to set the correct background level in the original image. If the background level is set too low, then the apparent brightness of the sources will be set too high and sources may be oversubtracted, unless the parameter f is set to a relatively small value. If the background is set too high, then sources will tend to be undersubtracted. In this case, combined with relatively small values of f , the model-subtracted data will appear to have had sources removed by truncation at a particular brightness level.

3.1.2. Source Masking

The source masking of KAMM1 was calculated iteratively from the original image. The mask is initially defined as all pixels with intensity more than $N_{clip}\sigma$ above the mean intensity, and all pixels surrounding these within a square $N_{mask} \times N_{mask}$ window. (The primary results of KAMM1 used $N_{mask} = 3$.) The process is then repeated with σ being replaced by $\sigma_{unmasked}$ (derived only from the unmasked data), and newly identified pixels being added to the mask. After several iterations the procedure will converge and no unmasked pixels with intensities $> N_{clip}\sigma_{unmasked}$ remain. The final result is very similar to masking the image at a fixed surface brightness threshold, and then expanding (dilating or growing) the mask to include the N_{mask} neighboring pixels.

An additional detail of the masking procedure is that we also construct masks from the models (described above), and then apply the union of both masks to the data analysis. This is done primarily to eliminate artifacts from ghost images. Ghost images are generally weak in our images because of dithering combined with the fact that the position of the ghost image will shift as a function of the location of the source on the detector array. Using the model to help insure they are masked increases the masked area by $\sim 2\%$.

Throughout the study we compute the power spectrum from Fourier transforms for fields in which $\sim 20 - 25\%$ of the pixels are masked and set to 0.0.

3.2. Power Spectra and Fluctuation Spectra

As presented here, the two dimensional power $P(u, v)$ of the model-subtracted and masked background intensity $\delta F(x, y)$ is simply derived from the discrete fast Fourier transform (FFT) of the image

$$P(u, v) = |FFT[\delta F(x, y)]|^2 = \left| \frac{1}{M} \frac{1}{N} \sum_{x=0}^{M-1} \sum_{y=0}^{N-1} \delta F(x, y) \exp[-2\pi i(ux/M + vy/N)] \right|^2. \quad (6)$$

This is reduced to a power spectrum, $P(q)$, where $q = 2\pi[(u/N)^2 + (v/M)^2]^{0.5}/\theta_{pixel}$, by averaging $P(u, v)$ in bins with spatial frequencies in the ranges $[q, q + \delta q]$, where the bin width $\delta q = 2\pi/[\theta_{pixel} \max(N, M)]$. For the binned power spectra, uncertainties estimated for $P(q)$ are calculated as the standard deviation of the mean for each bin. At the largest spatial scales, both the power and its estimated uncertainty are subject to large errors due to the small number (sometimes only 2) of independent measurements on these scales. We divide our power spectra by the fraction of pixels in the image that have not been masked (masked areas are set to zero intensity). Masking in the image domain corresponds to a convolution in the Fourier transformed domain. If the power spectrum is a flat function of frequency, then its convolution with the FFT of the mask will also be flat and unchanged (after rescaling for the fractional area masked). For power spectra that are strongly peaked at low frequencies (large spatial scales), the convolution produced by the masking shifts some of the power to higher frequencies, leading to underestimates of the large scale power. In §4.2 we show that this shift in power does not qualitatively affect our results, with the largest change being a reduction in power at the largest spatial scales by approximately the same fraction as the masked area of the image. Our power spectra are plotted as a function of $2\pi/q$ which is the spatial wavelength.

Because of the constrained detector orientation (position angle) during any given set of *Spitzer* observations, the self-calibration procedure cannot distinguish between strictly linear gradients in the sky and correlated gradients in the detector offsets F^p and F^q . Such gradients can be caused by calibration errors, zodiacal light, or the true astronomical background. In any case, to ensure that they have no effect, we omit the data along the x and y axes of the Fourier transformed image when calculating $P(q)$. This is done by simply omitting measurements $P(u, v)$ where $|u| \leq \delta q$ or $|v| \leq \delta q$ when constructing $P(q) = \langle P(u, v) \rangle_{[q, q+\delta q]}$ as described above. Doing so means that we obtain no result for the largest spatial scale (smallest q) that could be measured in principle, and the results at other large spatial scales are made slightly more uncertain. Omitting the power measured along the axis also eliminates the effects of many systematic errors, which tend to be aligned with the detector and thus are preferentially found along the axes of the 2-dimensional Fourier transform of the image. This is illustrated in Figure 2. Unless otherwise noted, all power spectra shown in this paper do not include power on the axes.

For comparison with the original images and the brightnesses of the resolved sources in the images, it is sometimes convenient to display the fluctuation spectrum, which is defined as $[q^2 P(q)/(2\pi)]^{0.5}$.

4. Test Cases and Results

In this section we present several tests aimed at identifying possible problems in the analysis of the clipped and model-subtracted background fluctuation. Table 2 is provided as a summary of the tests presented below and in our prior reports.

4.1. Self-calibration vs. GOODS processing

An assessment of the usefulness of the self-calibration can be made by examining images of the derived array offsets F^p and the temporal trends of the variable offsets F^q . Figure 3 shows the array offsets F^p derived at $3.6 \mu\text{m}$ for each of the AORs of the CDFS–e1 observations. These offsets display a relatively constant pattern of dark features. These represent long–term changes in the detector response compared to the standard gains and offsets applied by the BCD pipeline. There are both spotty features that likely represent long term latent images from previous observations, and a horizontal linear feature (about 64 pixels from the bottom of the detector array) that is more directly related to the hardware. Additionally, there are short–term detector changes that appear as white spots and lines. These are caused by staring at or slewing over bright sources in the time preceding the AOR where they appear. These features decay relatively quickly, affecting no more than 3 consecutive AORs. The detectors at 4.5 and $5.8 \mu\text{m}$ are not strongly affected by latent images, but at all wavelengths the self–calibration does find array offsets with fairly fixed patterns along with variable features that can change from one AOR to another. Thus with the self–calibration, we remove these artifacts as appropriate for each AOR.

The self–calibration also derives variable offset terms F^q . Example of these offsets at each wavelength are shown for the CDFS–e1 observations in Figure 4. In this figure, each of the four F^q values per frame is plotted (dots) as a function of time (in days) since the start of the observations of this field. The self-calibration assumes that the sky is a stable calibration source. However, since the zodiacal light intensity does change on a time scale of days, this variation is absorbed by the F^q term in the self-calibration. Thus, the figure shows a steady drift in F^q which is well–correlated with the change in the zodiacal light intensity (solid line). The infrequent but nearly periodic outliers are evidence of incomplete correction of the offsets in the initial frame of each observing sequence (the “first frame effect”). Other smaller scale ($\lesssim 1\text{d}$) drifts and jumps with respect to the zodiacal light trend are likely caused by instrumental changes, because their strength does not vary with wavelength as would be expected if they were caused by short-term variations in the zodiacal light. The clustering of points in time simply reflects the scheduling of the observations.

The differences made by application of the self-calibration to the data are often small compared to the brightness of typical sources in the images. Therefore, it is difficult to see the effect of self-calibration on a full-intensity image. However, the effects become very evident when examining certain processed results in which the appearance of the point sources is minimized. Ratio images between our self–calibrated mosaics, and those prepared by the GOODS team show evident differences, but in such images it can be difficult to determine which of the original images is causing which artifacts in the ratio. A more decisive comparison can be made by examining the ratio of mosaics at two wavelengths for the self-calibration, and the corresponding ratio for the GOODS pipeline processed data. Artifacts in these ratio maps are definitely the fault of the corresponding data reduction, although here it may be ambiguous as to which wavelength (if not both) contains the flaws. In constructing these ratios, we add small offsets (~ 3 times the noise level) to the data such that the ratios are always positive and the noise does not dominate the appearance. Figure

5 shows the ratio images of $4.5 / 3.6 \mu\text{m}$ mosaics for our self-calibrated data, and for the GOODS processed data (v0.3). Also shown are the median intensities of each ratio, taken across rows and columns. Masking is applied to the bright sources to eliminate the distraction of the intrinsic color variations of some of these sources. The comparison shows that while neither ratio is perfectly flat, the self-calibrated data show significantly less large-scale structure. Here it is very clear that the GOODS result contains an artifact related to the coverage of the field, whereas the self-calibrated result is much flatter. This difference can be traced to a gradient in the detector offset that we identify and remove through the self-calibration process (see §4.3). The corresponding ratio images for $8 / 5.8 \mu\text{m}$ are shown in Figure 6.

4.2. Modeling and clipping

An important aspect of the source modeling procedure (§3.1.1) is the determination of the optimal depth of the model. For the results presented here, we have chosen the optimal depth to be that where the residual intensities (after clipping and subtraction of the model) exhibit zero skewness [i.e. the normalized third moment of the distribution: $\langle(x - \bar{x})^3\rangle/\sigma^3$]. This is because any true sky sources contribute to the positive tail of the distribution, whereas the noise is expected to have zero skewness. We note, however, that the final results are very similar if we use our prior criteria, such as either the iteration where negligible correlation with removed emissions is reached, or when the shot noise from the remaining sources is sufficiently larger than the $A - B$ estimate of the instrument noise so that no significant amount of the instrument noise is removed in the modeling. Figure 7 shows the change in skewness of the pixel intensities for our modeled fields as function of the mean density of components. The density of components is the number of components subtracted by the model, divided by the area of the field. This quantity is related to the density of sources in the field, however because multiple components are required to model each source (§3.1.1), the actual density of sources in the images is several times lower. If the modeling is not sufficiently deep, remaining point sources leave a positive skew in the distribution of the residual intensities. If the model is too deep, the highest noise peaks begin to get subtracted, and the residual intensities develop a negative skew.

Figures 8-13 show the changes in the fluctuation spectra as a function of model depth for several fields. At 3.6 and $4.5 \mu\text{m}$, there are large changes in the residual fluctuation as a function of model depth on medium and large scales. Changes are small at the smallest angular scales ($\lesssim 4''$), which are instrument noise dominated. At these wavelengths it is relatively difficult for the models to fit the fluctuations down to the noise level on all scales. This indicates significant structure in the images, but does not reveal whether the structure is astronomical, or rather an instrument or data artifact. At 5.8 and $8 \mu\text{m}$ changes in the fluctuations with model depth are less pronounced. The noisier fields (EGS and QSO 1700) can be modeled down to the $(A-B)/2$ noise level (§2.5) and lower. In the GOODS fields, after approximately zero skewness is reached, power at intermediate scales ($4 - 10''$) begins to rise, as the model starts to imprint a (negative) PRF into a formerly

random unstructured noise background.

We tested several other criteria for selection of the optimal model depth. These included the correlation coefficients between (a) the model M_i at iteration i and the residual intensity δF_i , (b) the change in the models $M_i - M_{i-1}$ and the residual intensity δF_i , (c) the model M_i at iteration i and the original intensity F , (d) the change in the models $M_i - M_{i-1}$ and the original intensity F . The former two correlation coefficients generally change from positive to negative at approximately the same depth as the skewness. However, these correlations are more strongly affected than the skewness by the initial zero level used in the modeling procedure. The latter two criteria are less suitable as they tend to asymptotically approach 1 and 0 respectively. We emphasize again that for the final iterations there are negligible correlations between the modeled sources and the source-subtracted maps.

Another important aspect of the modeling procedure is that the correct PRFs are used. If the PRF core or wings are too broad, point sources will be poorly fit, generally oversubtracted in the outer portions and undersubtracted in the inner portions. A too narrow PRF core is less of a problem, but will require a larger number of model components to fit each source. If the PRF wings are too weak compared to the true PRF, then it will be impossible to remove faint large-scale structure of bright point sources. To investigate the sensitivity of the residual emission to the PRF shape, we constructed models for the CDFS fields at 3.6 and 4.5 μm using PRFs that are raised to the 0.95 and 1.05 powers to effectively widen and narrow the PRF respectively. Figure 14 shows that using the narrower PRF has little effect on the results, but does require additional model iterations ($\sim 20\%$ more). At 3.6 μm , the models using the wider PRF require ($\sim 20\%$) fewer iterations, but leave an increased level of fluctuations in the residual intensity. However, at 4.5 μm the wider PRF produces similar results to those obtained with the nominal PRF. This indicates that our nominal 4.5 μm PRFs are slightly too narrow and/or have somewhat weaker wings than the true 4.5 μm PRF.

To investigate the effect that the source masking has on the derived power, we constructed a set of 160 simulations of fields the same size as the HDFN and CDFS. The simulated fields include: (1) a flat instrument noise component, (2) a shot noise component (flat at large scale and rolled off at small scale by the PRF) representing faint unresolved sources, and (3) a structured background (a power law at large scales, but also rolled off by the PRF at small scales). Individually resolved sources were omitted from the simulation so that the effects on the structured background would be more clearly displayed. One example of a simulated image is shown in Figure 15. The figure also shows the same simulation after masking roughly 5, 10 and 25% of the area. The latter mask is taken from the actual data. The other masks are versions that are processed to reduce to masked area. These masks were applied to each of the 160 simulations, and the power spectra were calculated. The mean of these power spectra are shown in Figure 16. When the power spectra are plotted on logarithmic axes, the effects of the masking appear to be very minor. When the power spectra of the masked simulations are normalized by those of the unmasked simulations, the differences become more apparent. Increased masking reduces the power at the largest scales by

approximately the same fraction as the masked area. There is a less significant increase in the power at small spatial scales. The figure also shows that the masking is not the cause of any excess power along the axes of the Fourier transformed images.

Other tests of the effects of the clipping were performed using the actual images. Figures 17-20 show the fluctuation spectra for the CFDS epoch 1 and epoch 2 fields, for several variations of the clipping mask at a fixed model depth. When the clipping mask is expanded by one or two pixels (i.e. the clipped regions are increased in size) using a mathematical erosion operator, there is very little change in the fluctuation spectrum. In most cases the largest changes are less than the 1σ uncertainties. The changes are similarly small when the clipping mask is reduced in size by 1 pixel using a mathematical dilation operator, with the exception of a small but significant increase in the fluctuation amplitude at scales $\lesssim 10''$. When the clipping mask is reduced in size by 2 pixels, many faint sources are no longer subject to any blanking at all. This creates large increases in the signal at the smaller angular scales, especially at 3.6 and $4.5 \mu\text{m}$ where the faintest sources blanked by the standard masking are well above the instrument noise limits.

The final masking test involved the additional masking by randomly located 3×3 pixel patches. Such masks were generated in which 10, 20, 30, 40, or 50% of the pixels were masked. These masks were applied in addition to the standard clipping masks. The results (shown in the right-hand panels of Figures 17-20) are similar to those of the simulations above. As the total area masked is increased, the power at the largest spatial scales decreases proportionally with the fractional area that is not masked, while the power at small spatial scales remains unaffected.

4.3. Constructed tests

As a check on the possible systematic errors in the power (or fluctuation) spectra of the data, we have calculated power (or fluctuation) spectra for various artificial images that are related to different aspects of the analysis. Similarities between the measured and artificial power spectra can indicate possible errors.

In Figure 21, we present the power spectra of the IRAC PRFs that we used in the source modeling procedure. Any real signal from the sky will be convolved by the PRF and thus its power spectrum will be multiplied by those shown here. The PRF will reduce power by factors larger than 2 on scales $\lesssim 10''$ at $3.6 \mu\text{m}$ to $\lesssim 20''$ at $8 \mu\text{m}$. Power arising from other sources (e.g. instrumental noise) will not be modulated (multiplied) by the PRF power spectra.

Figure 22 shows artificial images constructed by distributing delta functions in the same pattern as the dithering and the (2×2) raster mapping used for the CFDS-e1 field at 3.6 and $4.5 \mu\text{m}$. If power along the axes were included, the corresponding power spectra of these images would show a strong feature at $\sim 100 - 300''$, corresponding to the offset between the 4 raster pointings of the map. When the power on the axes is excluded (as in the figure), excess power is eliminated at $\sim 300''$, and is reduced at smaller spatial scales. This sort of feature is not directly present in the

power spectra of any field. However, most instrumental errors will be much more highly structured than a delta function. As an example of such an error we took the detector offsets (F^p and F^q) derived from the self-calibration of the full data set at half-resolution, and repeatedly added them to a blank sky in the same pattern as the dithering. This creates images representing the errors that would be present had we not removed the detector offsets via the self-calibration. These are shown in Figure 23 along with the corresponding power spectra. Both power spectra can be approximated as the sum of a flat white-noise component and a steeply rising power law component with an index of 2.3 - 2.4. This rising component is steeper than that seen in the power spectra of the actual sky. At $4.5 \mu\text{m}$, the turnover at $200''$ is hidden by large scale power represented in the F^q offsets. The amplitudes of these power spectra are large enough that they would contribute significantly to the result if we had not self-calibrated the data. In fact the pattern seen here in the $3.6 \mu\text{m}$ offsets is largely responsible for that seen in the ratio of the $3.6/4.5 \mu\text{m}$ data reduced by the GOODS team (see Figure 5).

Other artificial images that we have examined are based on the actual sky instead of the instrument and observing strategy. The first of these test images is constructed by applying the complement of the clipping mask to the original sky map. This creates an image consisting of only the bright sources, with the background set to 0.0 between them. The power spectrum of this image serves as a check on any large scale structure that may be intrinsic to the distribution of the bright sources. The results are shown in Figures 24-29 (blue lines), where we have renormalized these power spectra to match the observed spectra at $8 - 15''$. In all cases, there is no excess power at large spatial scales. The second sky-based test is to calculate the power spectrum of the mask itself. This is similar to the previous test, but it removes the effective weighting with source brightness, which is present in the previous test. The results are shown as the red lines in Figures 24-29, where they have been arbitrarily normalized to the observed power spectra at angular scales $> 30''$. While the power spectrum of the mask has a large scale shape similar to the data, the mask is uncorrelated with the residual fluctuations, and subtracting any scaled version of the mask only *increases* the large scale power. A more complex test image was created by setting the intensity to be the inverse of the distance from the nearest blanked region of the mask. This “halo” image simulates the extended wings of bright sources that would remain after the application of a simple masking defined strictly by a surface brightness threshold. Removal of such wings, whether intrinsic to the source or caused by the PRF, are a large part of the motivation for the model we subtract. This simulated image can test whether the model over- or under-subtracts such features. We scaled these test images using the slopes of linear correlations between these and the model-subtracted images. Correlations were generally weak, though statistically significant. The power spectra of the test images are shown as green lines in Figures 24-29. In all cases the power is not more than $\sim 10\%$ of the power of the actual background. (In some cases the power is below the minimum range in the plots.)

One additional check illustrated in Figure 28 is the comparison of the $3.6 \mu\text{m}$ power spectrum derived when starting with the raw data (as described in §2.2) and the power spectrum derived when

the processing starts with the latest version (S18.7.0) of the BCD data. The two power spectra show only small differences ($\lesssim 2\sigma$) at the smallest angular scales and at large angular scales ($2\pi/q > 10''$). More significant, though still small, differences occur at angular scales $2'' < 2\pi/q < 10''$. These scales are typically dominated by the shot noise (see next section), which is sensitive to the depth of the source model that is subtracted. The source models were calculated independently for the mosaics derived from the raw and the BCD data.

5. Characterization of Power in Different Fields

In this section we characterize the final power spectra for each field and each wavelength by fitting the power spectra with empirical models with 3 or 4 free parameters. To the extent that these models provide good fits, the derived parameters may provide a simpler means of representing the power spectra.

Our idealized model of the power spectrum includes three components: instrument noise, shot noise, and a power law. For this model we assume instrument noise has a flat spectrum, with the normalization as its only free parameter. This is expected if there are no correlations in the response of the detector pixels. The shot noise is intended to represent the random Poisson statistics of sources below the confusion limit. Intrinsically this component is also flat. However, as the observed sky is unavoidably convolved by the PRF, this component is correspondingly modulated by the power spectrum of the PRF, which greatly reduces power at small angular scales. This component also has only its normalization as a free parameter. The power-law component is included to represent any excess power at large angular scales. It is also modulated by the power spectrum of the PRF, and contains two free parameters: a normalization and the power law index. This flat noise model can be expressed as:

$$P(q) = a_0(2\pi/q/100'')^{a_1} P_{PRF}(q) + a_2 P_{PRF}(q) + a_3. \quad (7)$$

A slightly different model was also fit, in which the flat noise was replaced by the measured A-B noise spectrum. In this case the normalization is fixed, and there is no free parameter associated with this component.

$$P(q) = b_0(2\pi/q/100'')^{b_1} P_{PRF}(q) + b_2 P_{PRF}(q) + P_{A-B}(q) \quad (8)$$

Using the A-B noise spectrum instead of a flat instrument noise (assumed above) is an improvement if the structure in the A-B spectrum is purely instrumental, and does not include any astronomical component or systematic errors.

The parameters (and formal uncertainties) derived via these fits are presented in Tables 3 and 4. Figures 30 - 33 show the results graphically. The uncertainties listed in Table 3 are the formal uncertainties for the given parameters. However, Table 4 shows that in many cases there is

significant covariance between parameters, and thus assessing agreement or disagreement of results in different fields requires caution.

At 3.6 and 4.5 μm , the limiting factor in the results is the instrument noise, as characterized by a_3 . As the instrument noise decreases from field to field, the shot noise (after subtracting the source model to reach zero skewness) decreases correspondingly. The EGS and FLS fields differ from the overall trend because they have been mapped with 1.2'' pixels, rather than 0.6'' pixels. Therefore, the noise at the pixel scale is reduced by a factor of 2. This allows the pixel-based source modeling to run to fainter levels, leading to a corresponding decrease in the shot noise in the residual image. The amplitude of the power law component decreases as the shot noise decreases. This indicates that a large fraction of the power seen in the shallower fields (QSO 1700, and EGS) arises from faint sources, which are modeled and removed in the deeper GOODS fields. If the GOODS fields are only model-subtracted to the same shot noise level as the QSO 1700 or EGS fields, then they have a power law component with a comparable amplitude to the shot noise in the QSO 1700 and EGS fields.

Results at 5.8 and 8 μm , are more erratic because in some cases the best-fit parameters include a negligible amplitude for one of the components. In such cases there are also extremely large covariances between the parameters. Aside from the anomalous cases, it is apparent that the power law component at these wavelength is steeper than that at 3.6 and 4.5 μm .

Final power spectra are compared in Figure 34, and in Figure 35 the spectra are all normalized to match that of CDFS-e1 at $2\pi/q > 5''$. These figures provide a more visual comparison, as an alternative to the quantitative details of Tables 3 and 4. The reduced χ^2_ν values for the comparison of these normalized power spectra are given in Table 5. The largest discrepancy amongst the GOODS fields is seen to be the HDFN-e2 field at 3.6 and 5.8 μm . This is a result of residual detector artifacts induced by the $K_S = 10.2$ magnitude star 2MASS 12373797+6216308, which is present in this field. It is ~ 2 magnitudes brighter than any other star in any of the GOODS fields. When the 3.6 μm HDFN-e2 field is cropped to a smaller size to exclude this star's artifacts, the large scale power spectrum becomes more similar to those of the other GOODS fields. As discussed in §2.2, spikes in the power spectra caused by the detector muxbleed artifact are visible at $2\pi/q = 4.8''$ and $2.4''$. These are only present at 3.6 and 4.5 μm , and are strongest in the QSO 1700 data. At these specific frequencies the power is factors of 2-4 higher than adjacent frequencies, but there is no expected or apparent effect on the power spectrum at low frequencies.

6. Discussion

The preceding discussion detailed the analysis of CIB fluctuations in the source-subtracted deep *Spitzer* data. We have shown that after removing foreground sources there remains a significant CIB fluctuations component. This component exceeds the instrument noise and is approximately isotropic on the sky consistent with its cosmological origin. This section is devoted to discussing

the implications of the KAMM results. We start with summing up the requirements that any qualified source-subtracted CIB data analysis must meet, following which we discuss the cosmological implications of our results. We conclude this section with a comprehensive comparison between our results and the various other measurements/constraints of the CIB.

6.1. Requirements for CIB fluctuations studies: a summary

By design, CIB fluctuations studies are necessary in order to uncover populations which cannot be resolved because they are *fainter than either the sensitivity limit or the confusion limit of the present-day instruments*. Recent years have seen increased interest and activity in measuring CIB fluctuations. We feel it is important to summarize a *minimal* set of requirements any quality study of CIB fluctuations should meet. These requirements cover three major aspects of the problem: I) preparing the maps that accurately isolate the source-subtracted CIB fluctuations down to the (faint) levels expected from first stars; II) tools required to correctly analyze the processed (and clipped) data; and III) details required for robust cosmological interpretation of the results.

- I. *Map assembly:*

1. Maps of diffuse emission should be constructed carefully removing artifacts down to levels well *below* those of the expected cosmological signal. In practice, this means that the maps should not have any structure at levels above $\delta F \sim 0.01 \text{ nW m}^{-2} \text{ sr}^{-1}$ at \sim arcminute scales in IRAC channels.

2. No correlations should be introduced when constructing the maps.

3. Observations must be carried out in a way that enables spatial structure on the sky to be distinguished from structure of the telescope and instrument on the scales of interest. The images produced should not contain any direct or indirect spatial filtering that modifies the spatial structure of the sky in unknown ways.

4. Because of temporal variations of the zodiacal light, data should be collected in as short time intervals as possible. For the GOODS fields combining data separated by 6 months (E1 and E2) is not reliable when trying to measure fluctuations as faint as $\lesssim 0.1 \text{ nW m}^{-2} \text{ sr}^{-1}$.

- II. *Analysis tools:*

5. Instrument noise, both its amplitude and the power spectrum, must be estimated from $A - B$ maps. It is particularly necessary for shot noise estimates etc.

6. When removing foreground sources, one should be careful with the effects from the remaining mask. If the fraction of removed pixels is small (in the IRAC images we find that it is typically $\lesssim 30\%$) one can compute the power spectrum using FFTs; otherwise the correlation function must be evaluated instead. In any case, one must demonstrate that the power spectra recovered are consistent with the computed correlation function, which is immune to mask effects.

7. The instrument beam (PRF) must be reconstructed and its large- and small-scale properties must be understood.

8. Thorough checks must be done to verify that no artifacts mimic the signal found.

• III. *Interpretation:*

9. A cosmological signal must be isotropic on the sky; this must be demonstrated with data whenever possible.

10. Foreground contributions must be evaluated: cirrus emission via estimates and zodiacal emission via measurements at different epochs (e.g. E1–E2 in GOODS measurements).

6.2. Source-subtracted CIB fluctuations from *Spitzer*

Fig. 36 shows the final source-subtracted CIB fluctuations obtained by averaging over all four GOODS areas at the optimal Model iteration as discussed above. KAMM3 show that the signal is made of two components: 1) small scales are dominated by the shot noise component produced by the variance of the remaining sources with the beam, and 2) the large scale CIB fluctuations are produced by the clustering of the sources producing the CIB. At the two longest wavelength IRAC Channels (5.8 and 8 μm) the instrument noise does not allow us to eliminate foreground galaxies to a sufficiently interesting shot noise level, so only results at 3.6 and 4.5 μm are shown in the figure and discussed in this section.

The dashed lines show the shot noise fits obtained by linear regression to the data. The remaining shot noise level at 3.6 and 4.5 μm from the populations with counts dN/dm of AB magnitude m is:

$$P_{\text{SN}} = \int S_0^2 10^{-0.8m} \frac{dN}{dm} dm \simeq (1.4 - 1.7) \times 10^{-11} \text{nW}^2 \text{m}^{-4} \text{sr}^{-1} \quad (9)$$

Here $S_0 = 3631$ Jy and the RHS gives the numerical values of the remaining shot noise at both Channels of Fig. 36. More generally Equation (9) can be rewritten as $P_{\text{SN}} \simeq S_0 10^{-0.4m} F_{\text{CIB}}(m)$, where $F_{\text{CIB}}(m)$ is the mean CIB produced by the sources with typical magnitude m . For dN/dm with power law slopes as observed at 3.6, and 4.5 μm , and at near-IR wavelengths (e.g. Fazio et al. 2004, Thompson et al. 2007a), the shot noise of Equation (9) will be dominated by the brightest of the sources that are not excluded, i.e. the extrapolation of the normal galaxy counts. Thus, the observed shot noise level is a strong upper limit on the shot noise that is associated with the sources that produce the large scale CIB fluctuations.

Fig. 1 of KAMM3 shows the shot noise expected from the observed source counts at 3.6 and 4.5 μm ; the residual shot noise levels imply that we have removed galaxy populations to at least AB $m \sim 26.5 - 27$. The large-scale CIB fluctuations must thus arise in fainter sources. KAMM4 show that the correlations between the ACS galaxies and the source-subtracted CIB maps are very

small and, on arcminute scales, are within the statistical noise. Thus, at most, the remaining ACS sources contribute to the shot noise levels in the residual KAMM maps, but not to the large scale correlations. In other words, the sources that produce the large-scale CIB fluctuations detected at *Spitzer* IRAC wavelengths are not present in the ACS source catalog. At the same time, there are excellent correlations between the ACS source maps and the sources *removed* by KAMM prior to computing the remaining CIB fluctuations, which testifies to the high accuracy of our Model subtraction procedure. Since the ACS galaxies do not contribute to the source-subtracted CIB fluctuations at 3.6 and 4.5 μm , the latter must arise at $z > 7$ as is required by the Lyman break (at rest, $\lambda \sim 0.1\mu\text{m}$) getting redshifted past the ACS z -band with a central wavelength $\simeq 0.9\mu\text{m}$. This would place the sources producing the KAMM signal within the first 0.7 Gyr. If the KAMM signal were to originate in lower z galaxies which escaped the ACS GOODS source catalog because they are below the catalog flux threshold, they would have to be extremely low-luminosity systems ($< 2 \times 10^7 h^{-2} L_{\odot}$ at $z=1$) and these galaxies would also have to cluster very differently from their ACS counterparts (KAMM4).

We now turn to estimating the levels of the CIB required by our results; the methodology of this follows KAMM3. We believe the absence of correlations between the source-subtracted IRAC maps and ACS maps places the sources responsible for the CIB fluctuations at $z > 7$. At $z = 5 - 10$ one arcminute subtends comoving scales of 2-3 h^{-1} Mpc. Such scales are in the linear regime at these epochs. So at $1+z > \Omega^{-1/3}$ in the flat Universe with cosmological constant, the amplitude of the density fluctuation is related to that at present via $\delta(z) \simeq \delta(z=0)1.3(1+z)^{-1}$. (The numerical factor of 1.3 for comes from the fact that density fluctuations grow very little at $(1+z) < \Omega^{-1/3}$). The present-day density field is normalized to the rms density contrast over a sphere with radius $r_8 = 8h^{-1}\text{Mpc}$ of $\sigma_8 \sim 1$ at the present epoch.

One can now estimate the order of magnitude of the relative CIB fluctuations. The cosmological parameters relevant to such an estimate are well approximated as: the comoving angular diameter distance, $d_A \simeq 5.4[(1+z)/6]^{0.3}h^{-1}\text{Gpc}$ and the cosmic time $t \simeq 1.2[(1+z)/6]^{1.5}$ Gyr. The normalization scale r_8 would thus subtend an angle of $\theta_8 \simeq 4'[(1+z)/6]^{-0.3}$ and fall in the middle of the angular scales where we detect the clustering component of the CIB fluctuations. The relative fluctuation in the projected 2-dimensional power spectrum, Δ , on that angular scale θ_8 , produced from sources located at mean value of \bar{z} and spanning the cosmic time Δt , would be

$$\frac{\delta F_{\text{CIB}}}{F_{\text{CIB}}}(\theta_8) \sim \sigma_8(1+\bar{z})^{-1}(r_8/c\Delta t)^{1/2} \simeq 0.02\sigma_8\left(\frac{\bar{z}}{10}\right)\left(\frac{\Delta t}{\text{Gyr}}\right)^{-1/2} \quad (10)$$

neglecting the amplification due to biasing. For the first star systems forming in the concordance ΛCDM Universe, biasing can amplify the fluctuations by a factor of $\sim (3 - 5)$ (Cooray et al. 2004, Kashlinsky et al. 2004), so the relative fluctuations are likely to be at most $\lesssim 10\%$. *Thus in order to produce a CIB fluctuation of amplitude $\delta F \sim 0.05 - 0.1 \text{ nW m}^{-2} \text{ sr}^{-1}$ at arcminute scales these populations had to produce at least $F_{\text{CIB}} \gtrsim 0.5 - 1 \text{ nW m}^{-2} \text{ sr}^{-1}$ in CIB flux.*

More generally, the fluctuations in the CIB generated by sources clustered with the 3-dimensional power spectrum P_3 is given by the Limber equation which can be written as follows (Kashlinsky

2005a):

$$\frac{q^2 P(q)}{2\pi} = \Delta t \int_{\Delta t} \left(\frac{dF}{dt} \right)^2 \Delta^2 (q d_A^{-1}) dt ; \Delta^2(k) \equiv \frac{1}{2\pi} \frac{k^2 P_3(k)}{c \Delta t} \quad (11)$$

where d_A is the comoving angular diameter distance to z , Δt is the cosmic time spanned by the emitters and Δ is the rms fluctuation in the emitters counts over a cylinder of length $c\Delta t$ and radius $\sim 2\pi/k$. Equation (11) shows that any given shape in $\Delta(k)$ does not necessarily translate into a similar shape in the angular spectrum of CIB fluctuations. It is important to bear in mind that the relation between the measured $P(q)$ and the underlying $P_3(k)$ can be quite convoluted and, in general, depends on the evolution of the CIB rate production, dF/dt , and other parameters.

It is of interest to consider how well populations described by a pure Λ CDM model at high z , with a power spectrum $P_{\Lambda\text{CDM}}$ deduced from WMAP observations, fit the KAMM measurements. In the case of the first stars, such populations are likely to be biased, i.e. the luminous sources form at the high peaks of the underlying density field. The relation between the underlying $P_{\Lambda\text{CDM}}$ and $P_3(k)$ is likely to be non-linear even on linear scales depending on the height of the peaks (Jensen & Szalay 1986, Kashlinsky 1998), but as a toy model we approximate here that $P_3(k) \propto P_{\Lambda\text{CDM}}$. We further assume that dF/dt does not vary significantly over the corresponding epochs, which can happen if the emitters span a narrow range of cosmic times. In this case the CIB fluctuations are reduced to $\sqrt{q^2 P/2\pi} = \Delta t dF/dt \bar{\Delta}$, where $\bar{\Delta}^2$ being the suitably averaged value of $(\Delta t)^{-1} \int \Delta^2 dt$ which we assumed dominated by a narrow range of epochs. The values of Δ for the concordance Λ CDM at high z collapse onto a line of universal shape whose amplitude is proportional to $\sigma_8(1+z)^{-1}(\Delta t)^{-1/2}$; this model spectrum, with an amplitude obtained by regression to the data, is shown with a thick solid line in Fig. 36. The shape of the Λ CDM model power spectrum dictates that the amplitude of that line does not change appreciably between $\sim 0.5'$ and $10'$ in approximate agreement with the data. Although this simple model (with the addition of a shot noise component) provides a decent fit to the data, one can notice, however, that it deviates at places from the measurements. This is not unexpected given the simplicity (and likely inaccuracy) of this toy model, and may be indicative of the particular form of dF/dt and/or biasing over the epochs of emissions contributing to these CIB fluctuations.

As we remove populations to progressively lower levels of P_{SN} , we should eventually remove also the populations producing the clustering CIB component. This shot noise level, at which the clustering component goes away (or is substantially reduced) will provide one with information on the typical fluxes of the sources. One can already set an *upper* limit (see KAMM3) from the current analysis where we reach the shot noise levels given in Table 3, whereas the levels of the residual fluctuations from clustering require CIB fluxes of $F_{\text{CIB}} \gtrsim 1 \text{ nW m}^{-2} \text{ sr}^{-1}$:

$$f_\nu(m) \leq 10 \left(\frac{P_{\text{SN}}}{10^{-11} \text{ nW}^2 \text{ m}^{-4} \text{ sr}^{-1}} \right) \left(\frac{F_{\text{CIB}}}{1 \text{ nW m}^{-2} \text{ sr}^{-1}} \right)^{-1} \text{ nJy} \quad (12)$$

The magnitude of $f_\nu(m)$ is already comparable to that expected for Population III systems (see Fig. 38 below - the first stars are expected to form in mini-haloes of a few million solar mass and convert a substantial fraction of that mass into stars.). At the same time, Table 1 and Fig. 1 of

KAMM2 possibly already show (modest) decrease in the levels of the clustering component of the CIB fluctuations.

Thus if we remove sources to the shot noise levels significantly lower than in the earlier analyses, we should reach into the shot noise produced by the first systems and characterize their individual flux levels. It is impossible to achieve that with the existing *Spitzer* deep fields because in any such analysis the instrument noise must be at least several times below the required shot noise (in order to have reliable source modeling for removal while keeping intact the underlying instrument noise structure). However, since the instrument noise amplitude scales $P \propto t_{\text{integration}}^{-1}$, in order to reach the shot noise levels required to identify what kind of populations produce the CIB anisotropies down to the nJy flux level, we would need to reduce the instrument noise by another factor of $\sim 4 - 5$ compared to the GOODS data. This can be achieved in approximately 100 hours per pixel integrations reaching the shot noise levels corresponding to an appreciable drop in the clustering component over a field of at least $5' \times 10'$ in size. The small Ultra-Deep field of the GOODS data located within the HDF-N region has, in principle, sufficient integration time for reaching the desired shot noise levels, but was obtained over several Epochs and only covers a region of $5'$ on the side. Our analysis of these data showed that we cannot extract the required large scale ($> 2'$) information reliably from these data. It also is in a region with cirrus emission estimated to be several times brighter than in the Lockman Hole.

Additional information on the populations responsible for these CIB fluctuations, can be obtained from the fact that the significant flux ($> 1 \text{ nW m}^{-2} \text{sr}^{-1}$) required to explain the amplitude of the fluctuations must be produced within the short time available at these high z (cosmic times $< 0.5\text{-}1 \text{ Gyr}$). This can be translated into the comoving luminosity density associated with these populations, which in turn translates into the fraction of baryons locked in these objects with the additional assumption of their $\Gamma \equiv M/L$ (KAMM3). The smaller the value of Γ , the fewer baryons are required to explain the CIB fluctuations detected in the KAMM studies. It turns out that in order not to exceed the baryon fraction observed in stars, the populations producing these CIB fluctuations had to have Γ much less than the solar value, typical of the present-day populations (KAMM3). This is consistent with the general expectations of the first stars being very massive.

Assuming the first stars were massive and radiating close to the Eddington limit, the level of the near-IR CIB is directly related to the fraction of baryons processed by these stars and for the integrated NIRBE levels of $\sim 30 \text{ nW m}^{-2} \text{sr}^{-1}$ claimed by the various *IRTS* and *DIRBE*-based analyses this fraction is $f_* \sim 2 - 3\%$ (Kashlinsky 2005b). The minimal CIB fluxes required to explain the clustering component of the KAMM measurements are, however, much smaller and *would require the baryon fraction to be as small as $f_* \gtrsim 0.1\%$.*

6.3. Source subtracted CIB fluctuations and comparison to other measurements

6.3.1. Comparison to earlier CIB fluctuation measurements

Previous detections of near-IR CIB fluctuations involved analysis based on DIRBE (Kashlinsky & Odenwald 2000), *IRTS* (Matsumoto et al. 2005) and deep 2MASS (Kashlinsky et al. 2002, Odenwald et al. 2003) data. None of these are directly comparable to the KAMM measurements because of the different wavelengths involved, different angular scales and most importantly different levels of source subtraction.

The DIRBE analysis of Kashlinsky & Odenwald (2000) measured the CIB fluctuations at $\sim 0.5^\circ$ at wavelengths overlapping with *Spitzer* (DIRBE bands L and M), while *IRTS* measurements were effectively done at $\lambda \sim 2 \mu\text{m}$. Neither the DIRBE nor *IRTS* analysis allowed for any significant source subtraction because of the poor angular resolution and large confusion noise, and thus both measured the total CIB fluctuations, making it impossible to isolate the high z contributions.

Analysis of deep 2MASS data (Kashlinsky et al. 2002, Odenwald et al. 2003) enabled more removal of foreground galaxy populations and measured CIB fluctuations out to $\sim 1'$ from remaining sources in J, H, K photometric bands (1.2, 1.6 and $2.2 \mu\text{m}$). This was because of the much better angular resolution, but atmospheric airglow and thermal fluctuations limited source removal to $m_{\text{Vega}} \sim 19 - 19.5$. As discussed explicitly by Kashlinsky et al. (2002), that analysis detected CIB fluctuations from ordinary galaxies at $z \gtrsim 1$; Fig. 2d,e there makes clear that their signal comes from sources at these redshifts and is not dominated by Population III sources (see also Fig. 5 of Kashlinsky et al. 2004).

To conclude, none of these earlier measurements allow for a model-independent analysis and robust comparison vis-à-vis the KAMM *Spitzer* measurements.

6.3.2. Comparison to γ -ray limits

Aside from direct determination of the CIB, indirect limits on it can be set by studying absorption of gamma-ray sources due to two-photon absorption. This reaction, $\gamma\gamma_{\text{CIB}} \rightarrow e^+e^-$, happens above a threshold $E_\gamma E_{\gamma_{\text{CIB}}} \geq (m_e c^2)^2$ and being electrodynamic in nature has cross section $\sim \sigma_{\text{Thomson}}$. Hence, for photons of the right energies it can provide efficient absorption over cosmological distances (Nikishev 1962). However, difficulties here are 1) interpretation usually requires assumptions about the original unabsorbed gamma-ray source spectrum and 2) the amount of absorption at each gamma-ray energy is not caused by a single energy IR photon, but is a complex integral over the entire range of CIB photons energies above the reaction threshold. Nevertheless, two recent studies (Dwek et al. 2005, Aharonian et al. 2006) suggested NIRBE levels significantly smaller than those indicated by the DIRBE and *IRTS* analyses.

The HESS team results (Aharonian et al. 2006) have received particular attention and we

address them below in light of the KAMM results. Their analysis involved modeling CIB with a scaled spectral template representing the CIB from normal galaxies, with or without the addition of a NIRBE component represented by the *IRTS* residual emission. Based on this model and assuming that the intrinsic hardness of the blazar spectra, $dN/dE \propto E^{-\Gamma}$, is $\Gamma \geq 1.5$, Aharonian et al. (2006) conclude that the full NIRBE suggested by *IRTS* would lead to more attenuation at $\sim 1 - 2$ TeV than the known blazar physics allows.

It is important to emphasize that even assuming the blazar physics limits adopted by Aharonian et al. (2006) the HESS data still permit significant CIB fluxes from the epochs identified with the Pop III era (Kashlinsky & Band 2007). A property of any such emission would be a part of the CIB with a Lyman break corresponding to (e.g.) $z \gtrsim 10$. As an example of such CIB we computed the intrinsic (corrected for absorption) blazar spectra assuming that the NIRBE contribution from Pop III scales as $\nu I_\nu \propto \lambda^{-\alpha}$ with $\alpha = 2$ and a Lyman limit cutoff corresponding to the Pop III era ending at $z_3=10$ and normalized to the shown levels of the integrated NIRBE flux, Δ_{NIRBE} in $\text{nW m}^{-2} \text{sr}^{-1}$ (Kashlinsky & Band 2007). The results are not sensitive to the assumed slope of νI_ν , which was adopted because it is in approximate agreement with the *IRTS* data as shown in Fig. 37 (see also e.g. Dwek et al. 2005). In addition we assumed the CIB from the observed galaxies populations to be given by that from the measured galaxy counts, as shown in Fig. 37. The figure shows that the attenuation due to CIB levels claimed by the *IRTS* and DIRBE measurements is probably too strong assuming $\Gamma \geq 1.5$, but *smaller levels of NIRBE are still allowed by the data* in that they lead to $\Gamma \leq 1.5$. In particular the HESS data require the levels of NIRBE due to Pop III (i.e. with Lyman cutoff in the CIB at $1 \mu\text{m}$) to be $\lesssim 5 \text{ nW m}^{-2} \text{sr}^{-1}$ leaving $\lesssim 1\%$ of the baryons to have gone through Pop III. The KAMM results, $\Delta_{\text{NIRBE}} \sim 1 \text{ nW m}^{-2} \text{sr}^{-1}$, are fully consistent with the HESS blazar data.

The HESS use of the blazar hardness index limit, $\Gamma \geq 1.5$, has been questioned by several authors who developed specific models that can reproduce much harder blazar spectra (Katarzynski et al. 2006, Stecker & Scully 2008, Krennrich et al. 2008). This could then allow much higher values of Δ_{NIRBE} . This situation is expected to be resolved with the data from the recently launched *Fermi* mission which should measure spectra of high- z gamma-ray bursts (GRBs) and blazars out to 300 GeV (Kashlinsky 2005b). Regardless of the precise amount of the near-IR CIB from them, Pop III objects likely left enough photons to provide a large optical depth for high-energy photons from high- z GRBs. Even if the NIRBE levels from Pop III were significantly smaller than claimed by the *IRTS* and DIRBE analysis, $\Delta_{\text{NIRBE}} \sim 30 \text{ nW m}^{-2} \text{sr}^{-1}$, there should still be almost complete damping in the spectra of high- z gamma ray sources at energies $\gtrsim 260(1+z)^{-2}$ GeV. Such damping should provide an unambiguous feature of the Pop III era and *Fermi* observations could provide important information on the emissions from the Pop III era (Kashlinsky 2005b).

6.3.3. Comparison to HST/NICMOS measurements and colors

Thompson et al. (2007a,b) have used very deep NICMOS data for a small ($\sim 144'' \times 144''$) field to study the contribution from resolved galaxies and conclude that the CIB at 1.1 and 1.6 μm is much smaller than the *IRTS* (Matsumoto et al. 2005) and the DIRBE (e.g. Cambresy et al. 2001) results suggest. From analysis of the NICMOS background fluctuations Thompson et al. (2007a,b) measure source-subtracted arcminute-scale fluctuations of $\delta F \lesssim 1 \text{ nW m}^{-2} \text{ sr}^{-1}$ at 1.1 and 1.6 μm . This is broadly consistent with our detected fluctuations of $\delta F(\sim 1') \sim 0.05 - 0.07 \text{ nW m}^{-2} \text{ sr}^{-1}$ at 3.6 and 4.5 μm (KAMM1-4 and above). Neither the IRAC nor NICMOS analyses provide direct measurements of the mean level of any unresolved background (including a NIRBE). The direct measurement of the mean NIRBE intensity with NICMOS is prevented by the fact that the zodiacal background subtraction is derived using a median image constructed from all individual exposures in the data set. The subtraction of the median image from each single image may not alter the fluctuations of any NIRBE, but it will remove the median intensities of any and all unresolved backgrounds. This includes the zodiacal light (as intended), but also includes any instrumental, geocentric, Galactic, or extragalactic components.

In principle, the colors of the source-subtracted CIB fluctuations provide additional information on the nature of the sources producing them. Thompson et al. (2007b) proposed that the NICMOS and NICMOS-to-IRAC colors are consistent with *normal* stellar populations originating at $z \lesssim 8$. At higher redshifts, the Lyman break begins to move through the F110W NICMOS filter, and the expected colors of galaxies begin to redden until $z \gtrsim 14.4$ when the sources completely drop out of the F110W filter. For sources with Pop III SEDs dominated by Ly α emission, such as the model shown in Fig. 38 (Santos et al. 2002), the expected colors would change more slowly with redshift, until a very abrupt drop off when Ly α shifts out of the F110W filter at $z \gtrsim 10.5$. In KAMM4, the lack of correlation between the IRAC fluctuations and faint sources in the ACS z band is presented as evidence that any high redshift contributors to the fluctuations are z -band dropouts, thus lying at $z \gtrsim 6.5$. However, beyond these robust constraints imposed by the Lyman break (and perhaps the Lyman α line), a detailed interpretation of the colors of the fluctuations requires assumptions about the intrinsic SEDs of contributing systems, *and* their abundance and evolution with z . Full analysis of the colors of the fluctuations should also include demonstration of a correlation of the fluctuations at different wavelengths, to ensure that the different wavelengths are not dominated by different populations of sources.

In the context of Pop III emission, such as discussed by Santos et al. (2002), the J and H band fluxes are dominated by Lyman α emission from the first stars that lie at $5.4 < z < 13.8$, whereas the IRAC filters would probe emission reprocessed by IGM and halo gas. Lyman α photons diffuse out of their original sources by scattering off neutral hydrogen before reionization (Loeb & Rybicki 1999). The density and structure of the halo gas and IGM are only weakly constrained at present, so the ratio of the J and H band emission to the mid-IR emission is very model- and epoch-dependent. Figure 36 shows that the clustering of the populations producing the KAMM signal at 3.6 and 4.5 μm is reasonably described by the concordance ΛCDM model with sources

at high z with the $3.6/4.5 \mu\text{m}$ color approximately expected for populations described by a model SED from Santos et al. (2002) as shown in Fig. 38. Because these particular Pop III models are dominated by Lyman α emission they could be made to fit a wide range of colors by placing the Population III systems at suitable redshift ranges and/or varying their abundances with z in a suitable fashion. For instance, such SEDs would lead to smaller $3.6/4.5 \mu\text{m}$ colors if there is strong evolution in the number density of the sources between $z \sim 15$ and $z \sim 10$. Mathematically, one can construct such evolution models as eq. 11 and Fig. 38 show.

7. Prospects for future measurements

This section discusses future prospects for isolating and identifying the nature of the populations responsible for the KAMM signal and their epochs. Progress in this can be achieved with the following three experiments which involve 1) large angular scales range, 2) larger wavelengths range, and 3) deeper integrations.

7.1. Larger Angular Scales

If the populations producing the KAMM signal lie at epochs of the first stars at high z , and assuming that the structures are seeded via the concordance ΛCDM model, the angular spectrum of source-subtracted CIB fluctuations should exhibit a peak at angular scales corresponding to the horizon scale at the matter-radiation equality projected to that redshift (Cooray et al. 2004, Kashlinsky et al. 2004, Kashlinsky 2005a). This peak should then subtend angular scales $\simeq 0.2^\circ - 0.3^\circ$ and can be identified with suitable mappings of regions covering sufficiently large areas.

Fig. 39 (left panel) shows the *expected* results that may be obtained by The *Spitzer* Extended Deep Survey (SEDS)⁵. This project will provide data to angular scales as large as 1 degree, with sufficient depth to detect foreground galaxies to $\sim 0.15 \mu\text{Jy}$ (5σ). The CIBER rocket experiment (Bock et al. 2005) is designed to detect spatial structure on scales up to 2 degrees, though with a much more limited capability for excluding faint foreground sources because of very shallow exposures.

7.2. Wider Range of Wavelengths

If these populations originate at high z their emissions below the Lyman break, at rest wavelengths $\lesssim 0.1 \mu\text{m}$, should effectively have been absorbed by the local IGM (Santos et al 2002, Schaerer 2002). Thus one should probe the level of residual diffuse light at wavelengths $\lesssim 1 \mu\text{m}$

⁵<http://ssc.spitzer.caltech.edu/geninfo/es/>

and see if they correlate with the source-subtracted CIB maps at IRAC bands. Progress here has been made by in KAMM4 where it was shown that the maps of deep ACS sources in GOODS observations exhibit completely negligible correlations with the source-subtracted maps at IRAC wavelengths. This likely places the sources producing the KAMM signal at $z \gtrsim 6.5$ unless they originate in extremely low-luminosity local galaxies with $m_{\text{AB}} \gtrsim 28 - 29$ that somehow escaped the ACS source catalog detection. Still, it would be desirable to compare directly the residual diffuse light maps in visible bands with those observed by IRAC. (The levels of residual maps artifacts in the ACS maps have prevented KAMM4 from doing such direct comparison).

Fig. 39 (right panel) shows the estimated ISM (cirrus) spectra in our deep fields and the Lockman Hole (a region of minimum H I column density). Emission from small grains and PAHs in the ISM rises sharply at wavelengths $> 5 \mu\text{m}$. At wavelengths of $\sim 0.7 \mu\text{m}$ the extended red emission (ERE; Gordon et al. 1998), is the likely limiting factor, with the directly scattered starlight being an underlying continuum at all wavelengths. Though *Spitzer* is incapable of observing at shorter wavelengths, CIBER will perform its fluctuation measurements at 0.8 and 1.6 μm , and also includes a low resolution spectrometer to search for a Lyman break redshifted into the CIB. The Wide Field Camera 3 on the *Hubble Space Telescope* and the NIRCAM instrument on the *James Webb Space Telescope (JWST)* should also provide good opportunities to extend CIB fluctuation studies to short wavelengths.

7.3. Deeper Integration

Finally, KAMM have already reached very low residual shot noise levels of $P_{\text{SN}} \simeq (1 - 2) \times 10^{-11} \text{ nW}^2 \text{ m}^{-4} \text{ sr}^{-1}$ at 3.6 and 4.5 μm and there is tentative evidence that the clustering signal already starts diminishing as lower levels of the shot noise are reached. This may imply that in our modeling we are already beginning to remove the very populations producing the large-scale fluctuations. This is not surprising since as shown in KAMM3 and discussed above, the low levels of the shot noise coupled with the relatively significant levels of the arcminute scales source-subtracted CIB fluctuations, imply that the sources producing the latter must have individual fluxes $\lesssim 20 - 30 \text{ nJy}$. This is already in the range of fluxes expected even for Population III systems as Fig. 38 shows. Hence, it is reasonable to expect that mapping a suitable region of up to $\lesssim 10'$ on the side with sufficiently long integrations ($\gtrsim 100 \text{ hr/pixel}$) should reach the shot noise levels, $P_{\text{SN}} \sim (\text{a few}) \times 10^{-12} \propto 1/t \text{ nW m}^{-2} \text{ sr}^{-1}$ where the clustering component of the CIB disappears completely, or is significantly diminished. This would then probe the flux levels of the individual sources producing the KAMM signal at arcminute scales. At this depth *Spitzer* becomes limited by confusion. However, with its much larger aperture, *JWST* will not be limited by confusion until much fainter levels, and should provide a much clearer picture of the clustering of very faint sources on angular scale $> 100''$.

8. Summary

This paper provides the details behind our prior analysis (KAMM1 – KAMM4) of the spatial fluctuations or power spectrum of the CIB. We show the extent to which the final results do or do not depend on the details of the data reduction and analysis.

For various deep *Spitzer* IRAC data sets, we show that the self-calibration that we apply to the data effectively removes spatial and temporal artifacts well enough to probe fluctuations in the source-subtracted CIB down to levels well below ~ 0.1 nW/m²/sr on arcminute angular scales. Some of the relatively strong and large-scale artifacts that we remove are seen to be present in the current v0.30 release of the independently processed GOODS data. The self-calibration procedure does not add artificial spatial correlations to the data.

We describe in detail the masking and modeling of the resolved sources. Various checks on these procedures involving either modest changes in their parameters, or the construction of test images demonstrate that the CIB fluctuations are not directly related to sources that could be identified above the sensitivity (or confusion) limits of the given observations. Table 2 itemizes the tests performed.

At 3.6 and 4.5 μ m the residual CIB fluctuations can be reasonably characterized using 2 components: shot noise, produced by the variance of sources too faint to be individually detected (dominant at small scales); and a clustered component which dominates on scales $\gtrsim 30'$. As a simplified representation of the power spectra of each field, we provide the parameters of fitting each power spectrum with these components, plus either a flat noise spectrum or an empirical estimate of the instrument noise.

We summarized the requirements that must be met by studies of such faint cosmological signals. We reiterate that the sources producing the large scale signal must have a very small shot noise component, while contributing significant fluctuations on arcminute scales. The latter component can be reasonably fit by a high- z population within a Λ CDM concordance model, with net CIB fluxes at 3.5 and 4.5 μ m of $\gtrsim 1$ nW/m²sr. The low levels of the shot noise imply that individual sources producing the large scale CIB fluctuations must be individually very faint, $\lesssim 20$ nJy. We then demonstrate that this population and its CIB level is consistent with the available data on high-energy γ -ray absorption, and HST NICMOS data on CIB and its colors.

Finally, we discuss future prospects for testing the nature of the CIB fluctuations: the currently approved SEDS survey in warm *Spitzer* mission would enable us to extend the measurements to sub-degree scales and probe the peak in the spatial spectrum of the fluctuations at $\sim 0.2^\circ$ expected from a high- z population in the Λ CDM concordance cosmology. Deeper IRAC integrations over a smaller region are recommended in that they could detect the shot noise levels where the clustering component disappears or is appreciably diminished; this would identify the flux range of the individual sources contributing to the latter. We point out that, while diffuse light measurements below 1 μ m could in principle probe the Lyman break of these populations, such measurements

may be limited by increased levels of scattered Galactic starlight light (and extended red emission) in the ISM.

Support was provided by the National Science Foundation through grant NSF AST 04-06587. This work is based on archival data obtained with the Spitzer Space Telescope, which is operated by the Jet Propulsion Laboratory, California Institute of Technology under a contract with NASA. Additional support for the First Look Survey (FLS) portion of this work was provided by an award issued by JPL/Caltech (NASA Spitzer NM0710076).

REFERENCES

- Aharonian, F., et al. 2006, *Nature*, 440, 1018
- Arendt, R. et al. 1998, *ApJ*, 508, 74
- Arendt, R. G. & Dwek, E. 2003, *ApJ*, 585, 305
- Barmby, P., et al. 2004, *ApJS*, 154, 97
- Bond, J. R., Carr, B. J. & Hogan, C. 1986, *ApJ*, 306, 428
- Bracewell, R. N. 1986, McGraw-Hill Series in Electrical Engineering, Networks and Systems, New York: McGraw-Hill, c1986, 2nd rev.ed., 77
- Bromm, V. & Larson, R.B. 2004, *ARA&A*, 42, 79
- Cambresy, L. et al. 2001, *ApJ*, 555, 563
- Cooray, A. et al. 2004, *ApJ*, 606, 611
- Cooray, A. et al. 2007, *ApJ*, 659, L91
- Dwek, E. & Arendt, R. 1998, *ApJ*, 508, L9
- Dwek, E., Arendt, R. & Krennrich, F. 2005, *ApJ*, 635, 784
- Dwek, E., Krennrich, F. & Arendt, R. 2005, *ApJ*, 634, 155
- Fazio, G. G., et al. 2004a, *ApJS*, 154, 10
- Fazio, G. G., et al. 2004b, *ApJS*, 154, 39
- Ferandez, E. & Komatsu, E. 2005, *ApJ*, 646, 703
- Fixsen, D. J., Moseley, S. H., & Arendt, R. G. 2000, *ApJS*, 128, 651
- Fruchter, A. S., & Hook, R. N. 2002, *PASP*, 114, 144

- Giavalisco, M., et al. 2004, *ApJ*, 600, L93
- Gorjian, V., Wright, E. L., & Chary, R. R. 2001, *ApJ*, 536, 550
- Gordon, K. D., Witt, A. N., & Friedmann, B. C. 1998, *ApJ*, 498, 522
- Guhathakurta, P., & Tyson, J. A. 1989, *ApJ*, 346, 773
- Haikala, L. K., Mattila, K., Bowyer, S., Sasseen, T. P., Lampton, M., & Knude, J. 1995, *ApJ*, 443, L33
- Hauser, M. et al. 1998, *ApJ*, 508, 25
- Hauser, M. & Dwek, E. 2001, *ARA&A*, 39, 249
- Högbom, J. A. 1974, *A&AS*, 15, 417
- Jensen, L. G., & Szalay, A. S. 1986, *ApJ*, 305, L5
- Kashlinsky, A. 1998, *ApJ*, 492, 1
- Kashlinsky, A. 2005a, *Phys. Rep.*, 409, 361
- Kashlinsky, A. 2005b, *ApJ*, 633, L5
- Kashlinsky, A. 2007, arXiv:astro-ph/0701147
- Kashlinsky, A., Odenwald, S., Mather, J., Skrutskie, M. & Cutri, R. 2002, *ApJ*, 579, L53
- Kashlinsky, A., Arendt, R. G., Gardner, J. P., Mather, J. & Moseley, S. H. 2004, *ApJ*, 608, 1
- Kashlinsky, A., Arendt, R. G., Mather, J., & Moseley, S. H. 2005, *Nature*, 438, 45 (KAMM1)
- Kashlinsky, A., Arendt, R. G., Mather, J., & Moseley, S. H. 2007, *ApJ*, 654, L5 (KAMM2)
- Kashlinsky, A., Arendt, R. G., Mather, J., & Moseley, S. H. 2007, *ApJ*, 654, L1 (KAMM3)
- Kashlinsky, A., Arendt, R. G., Mather, J., & Moseley, S. H. 2007, *ApJ*, 666, L1 (KAMM4)
- Kashlinsky, A. & Band, D. 2007, in "THE FIRST GLAST SYMPOSIUM", AIP Conference Proceedings, Volume 921, pp. 243
- Kashlinsky, A., Mather, J. C., Odenwald, S. & Hauser, M. 1996, *ApJ*, 470, 681
- Kashlinsky, A. & Odenwald, S. 2000a, *ApJ*, 528, 74
- Katarzynski, K. et al. 2006, *MNRAS*, 368, L52
- Krennrich, F., Dwek, E. & Imran, A. 2008, *ApJ*, 689, L93

- Leinert, C., et al. 1998, A&AS, 127, 1
- Loeb, A., & Rybicki, G. B. 1999, ApJ, 524, 527
- Matsumoto, T. et al. 2005, ApJ, 626, 31
- Mattila, K. 1990, in IAU Symposium 139, The Galactic and Extragalactic Background Radiation, ed. S. Bowyer & Ch. Leinert (Dordrecht, Netherlands: Kluwer Academic Publishers), 257
- Nikishov, A. I. 1962, Soviet Phys. JETP, 14, 393
- Odenwald, S., Kashlinsky, A., Mather, J. C., Skrutskie, M. & Cutri, R. 2003, ApJ, 583,535
- Salvaterra, R. & Ferrara, A. 2003, MNRAS, 339, 973
- Santos, M., Bromm, V. & Kaminowski, M. 2002, MNRAS, 336, 1082
- Schaerer, D. 2002, A&A, 382,28
- Shectman, S. A. 1974, ApJ, 188, 233
- Stecker, F. & Scully, S.T. 2008, ApJ, 691, L91
- Thompson, R., Eisenstein, D., Fan, X., Rieke, M. & Kennicutt, R. 2007a, ApJ, 659, 667
- Thompson, R., Eisenstein, D., Fan, X., Rieke, M. & Kennicutt, R. 2007b, ApJ, 666, 658
- Toller, G. N. 1981, Ph.D. Thesis, State University of New York at Stony Brook

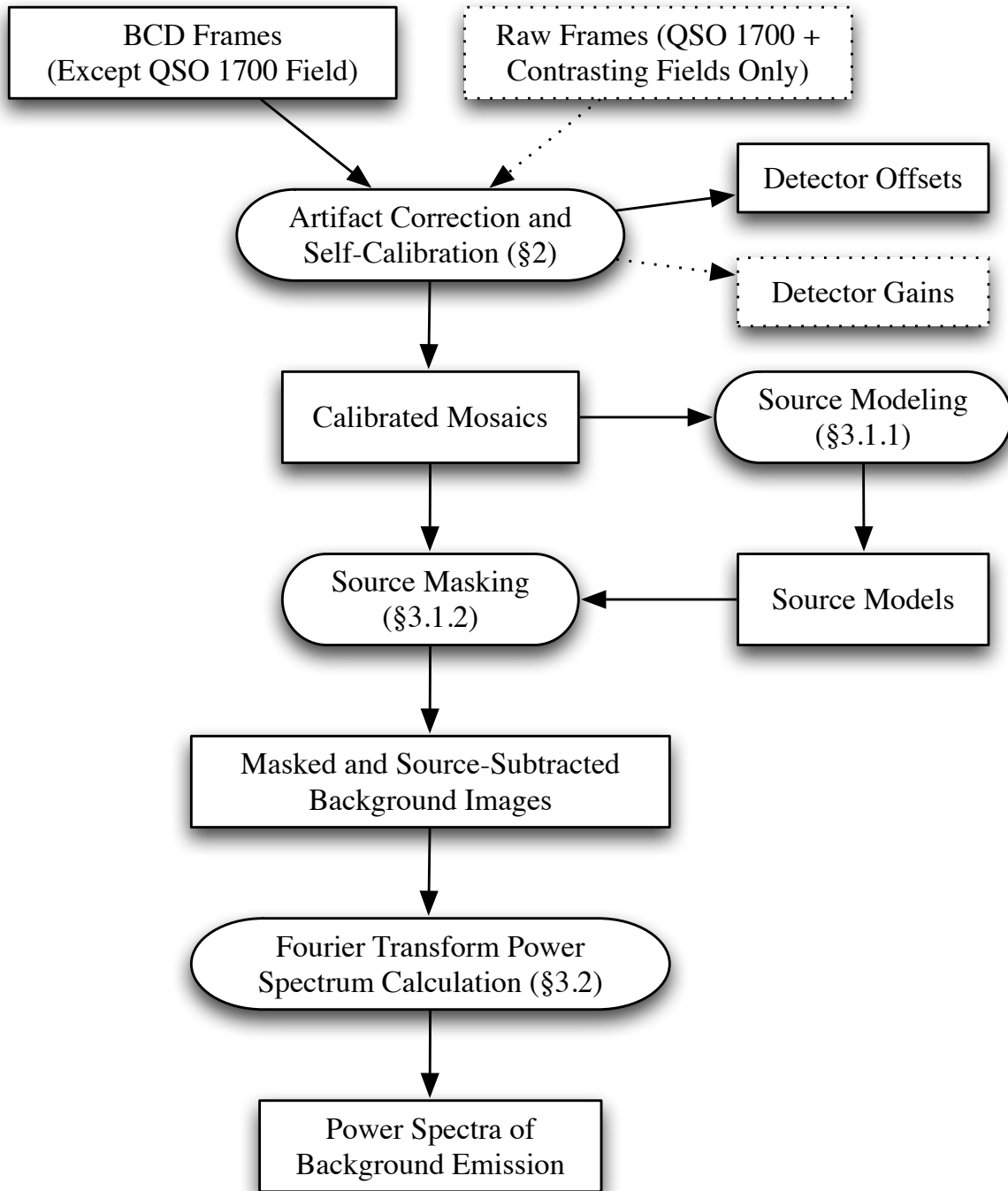


Fig. 1.— Flow chart of the data processing steps. Only for the QSO 1700 field was the process started with raw data rather than the BCD. This requires self-calibration for detector gains as well as offsets.

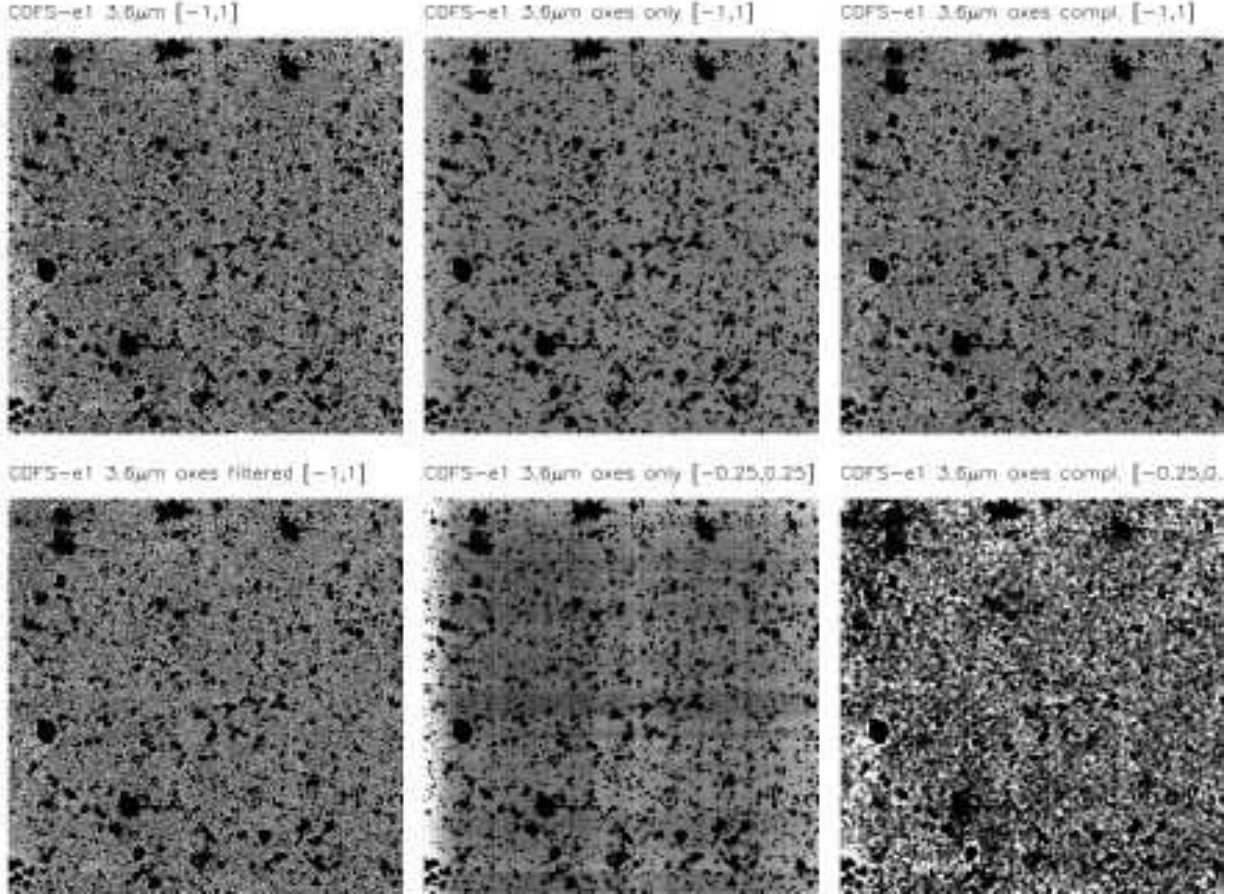


Fig. 2.— Illustration of systematic effects induced by artificial power on the axes of the Fourier transformed images. (top left) The blanked and model-subtracted CDFS epoch 1 field at 3.6 μ m, scaled from [-1,1] $\text{nW m}^{-1} \text{sr}^{-1}$. (bottom left) The same field after subtraction of power along the FFT axes and at scales $> 9.6''$. (top center) Image of the FFT power at scales $> 9.6''$ and on the axes of the FFT (i.e. the difference of the two images at left). (bottom center) Same image but on a narrower display range to better show structure related to the coverage of the observations. (top right) Image of the FFT power at scales $> 9.6''$, but *excluding* the axes of the FFT (i.e. this is the “complement” of the figure at top center). (bottom right) Same image as above, but on a narrower display range to show that the off axis power has little or no resemblance to the coverage or known detector artifacts.

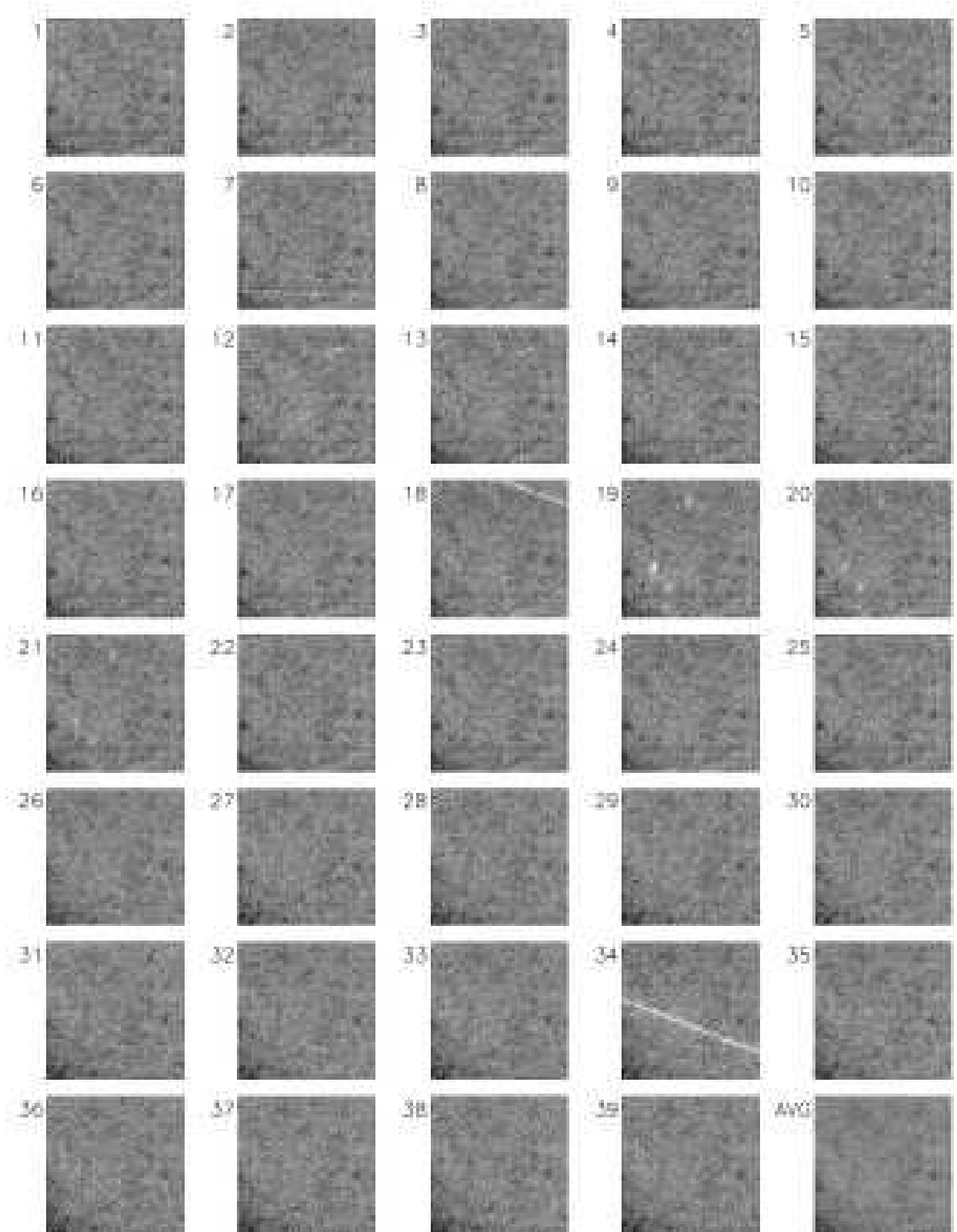


Fig. 3.— Array offset terms F^p at $3.6 \mu\text{m}$ derived for each AOR of CDFS-e1 from self-calibration. Note that some AORs (e.g. 19 – 21) contain latent images from intermixed observations of bright sources, or tracks from slewing across bright sources (e.g. 18, 34). Images are shown on a linear (black to white) stretch from $[-0.01, 0.01] \text{ MJy sr}^{-1}$ (or equivalently $[-8.33, 8.33] \text{ nW m}^{-2} \text{ sr}^{-1}$).

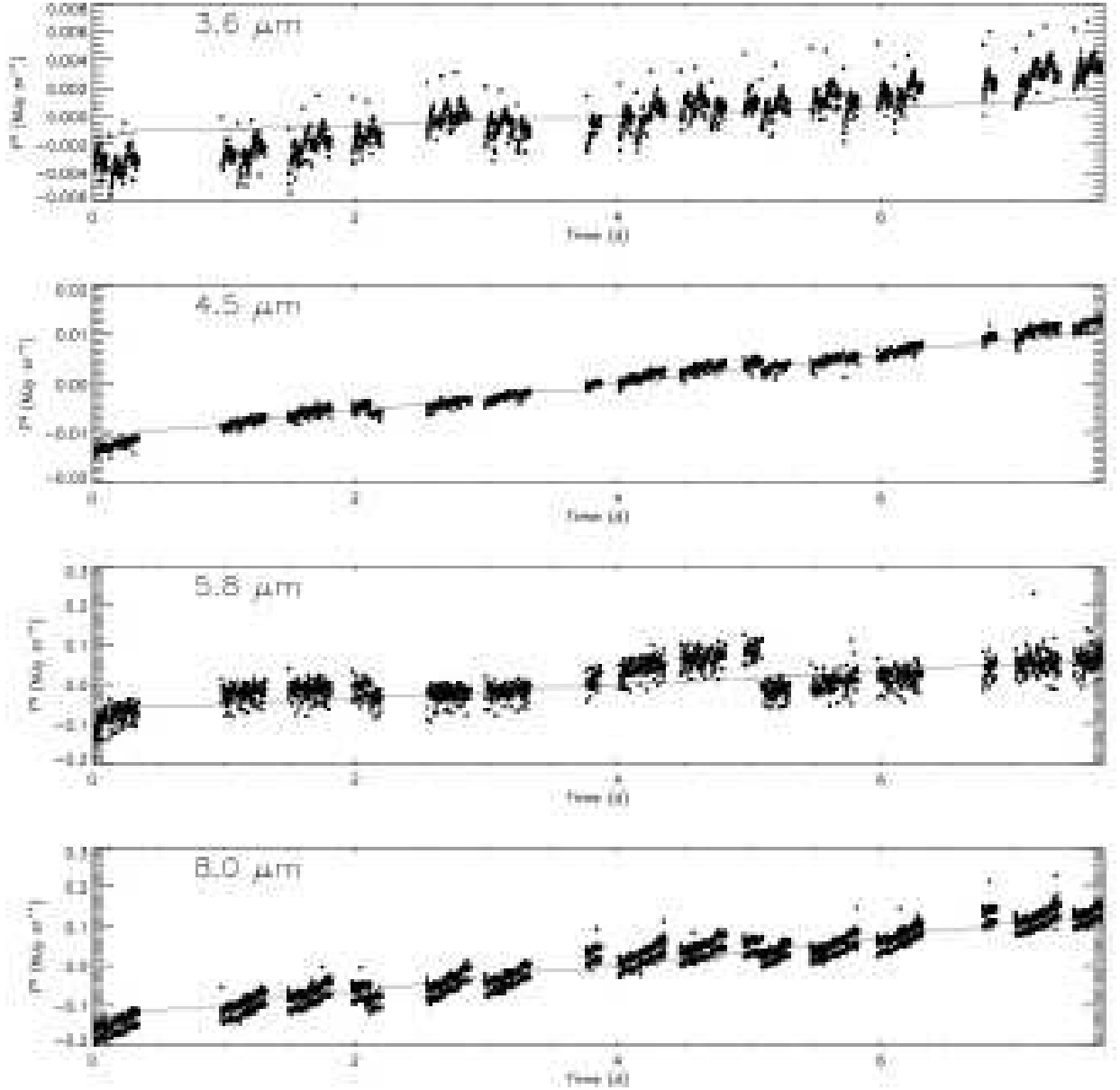


Fig. 4.— Variable offset terms F^q (dots) per frame derived by the self-calibration are plotted as a function of time since the start of the CDFS-e1 observations. The general trend of the changes in F^q correlates well with that expected for the zodiacal light as estimated by the ZODY_EST keyword values from the BCD headers (shown as solid lines). Smaller variations and jumps with respect to this trend are due to instrumental changes. The infrequent and nearly periodic outliers are the result of changes in IRAC’s dark frame (the “first frame effect”).

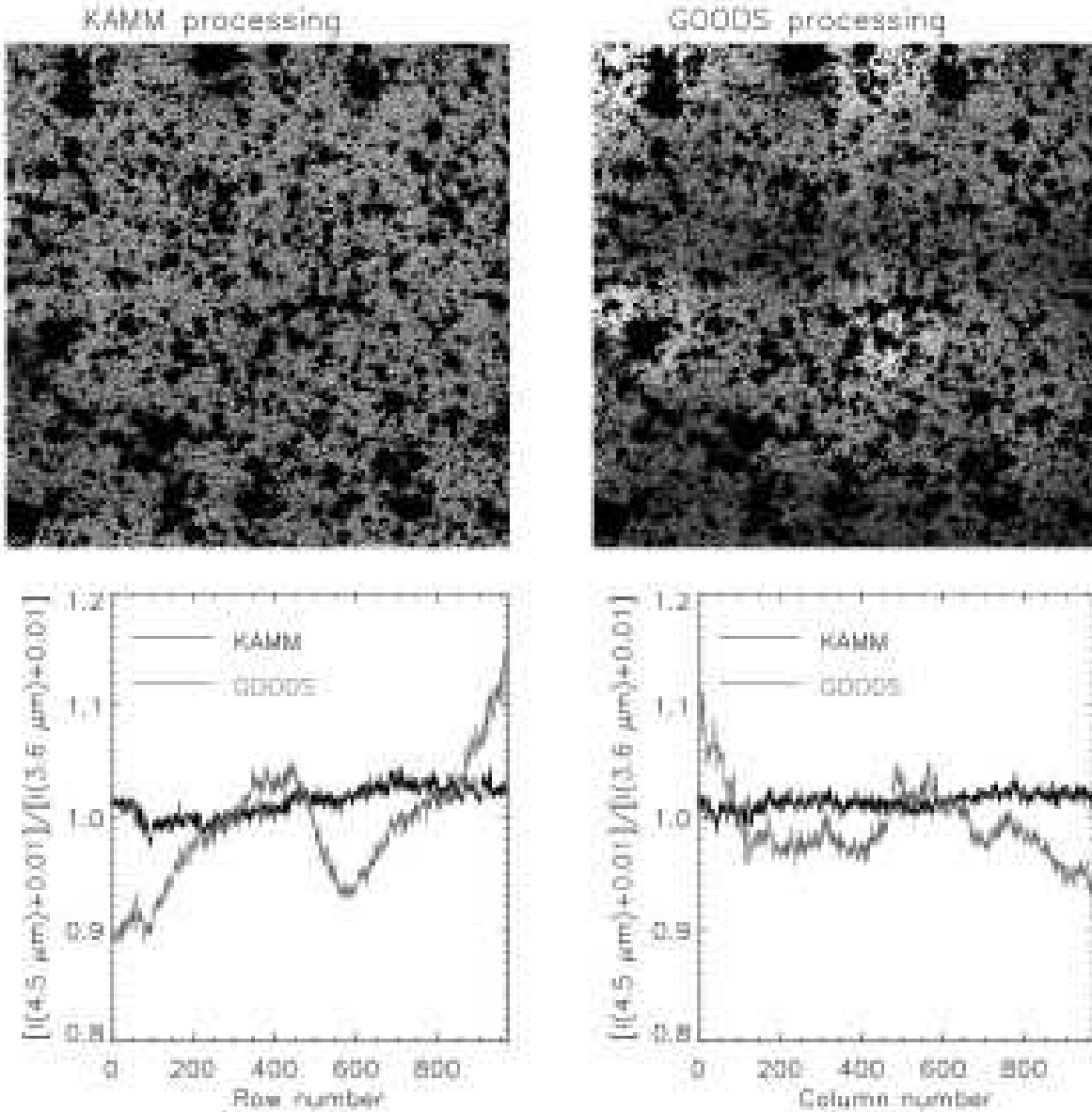


Fig. 5.— Ratio of $4.5 \mu\text{m} / 3.6 \mu\text{m}$ CDFS-e1 images for the KAMM processing and the GOODS processing ($v \ 0.30$). Bright sources in the images have been masked identically, but no model has been subtracted from either. One or both channels of the GOODS data contain a large scale artifact that reveals the 2×2 mosaicked coverage of the field. The lower panels compare median intensities across each ratio image as a function of row and column. Small offsets are added to the ratios so that the ratios are always positive with a mean near 1. The images on the right are clearly problematic in uncovering faint diffuse signal but were used in CIB analysis of Cooray et al. (2007). The pattern seen in the GOODS processing is related to the calibration of the detector offsets, as shown in Fig. 23 and discussed in §4.3.

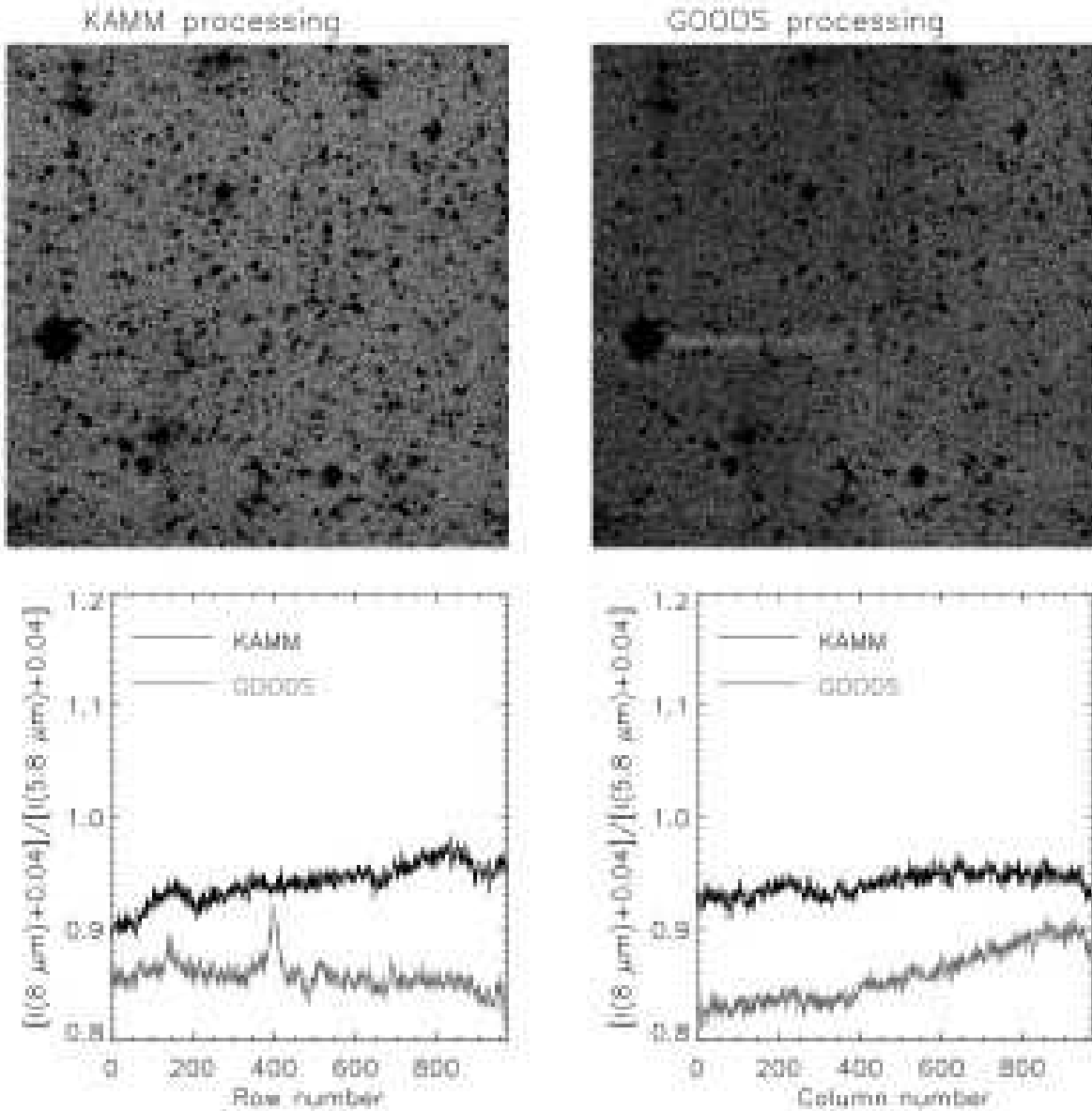


Fig. 6.— Ratio of $8.0 \mu\text{m} / 5.8 \mu\text{m}$ CDFS-e1 images for the KAMM processing and the GOODS processing (v 0.30). Bright sources in the images have been masked identically, but no model has been subtracted from either. The lower panels compare median intensities across each ratio image as a function of row and column. Small offsets are added to the ratios so that the ratios are always positive.

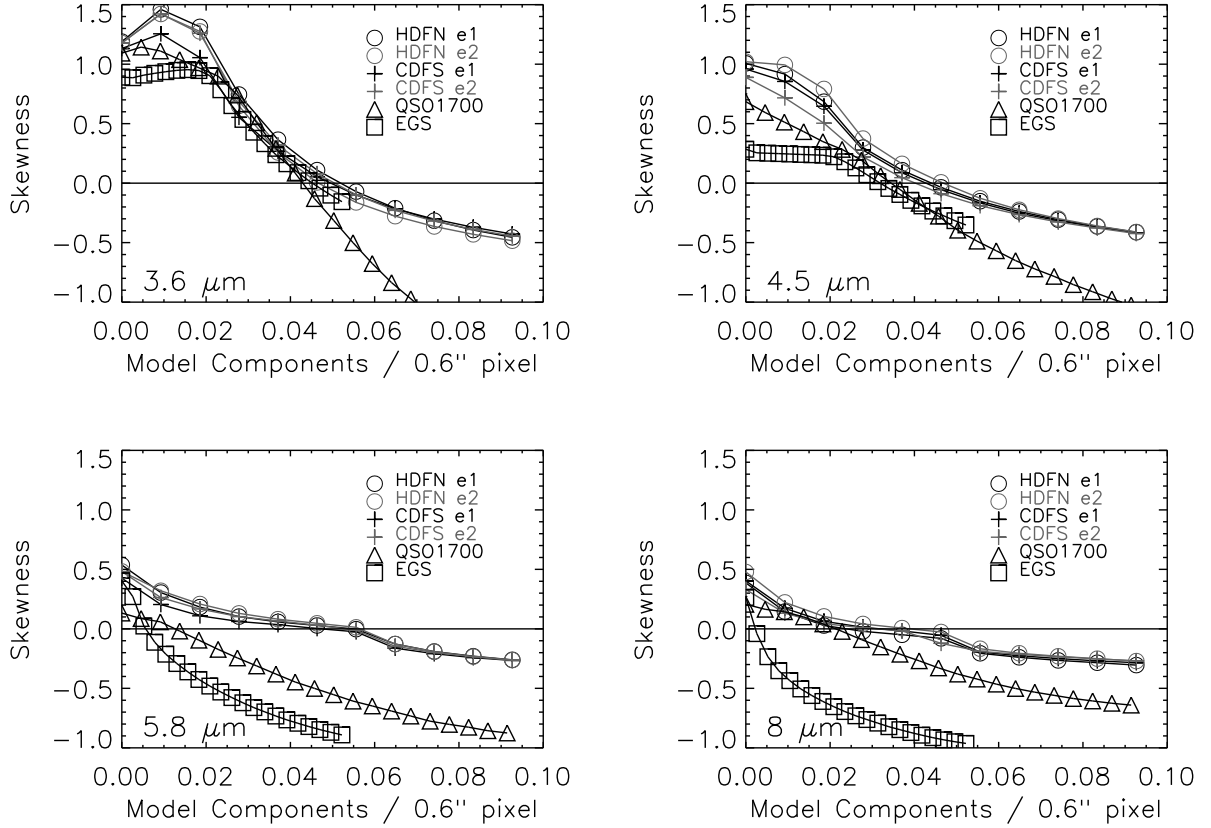


Fig. 7.— The skewness of the distribution of pixel intensities for the model-subtracted fields, as a function of the density of model components (the number of components subtracted by the model divided by the area of the field). The symbols denote intervals of 3000 model components for the QSO 1700 and EGS fields, and 120000 components for the other fields. Models that yield negative skewness are likely too deep, and are increasingly attacking random noise rather than actual sources.

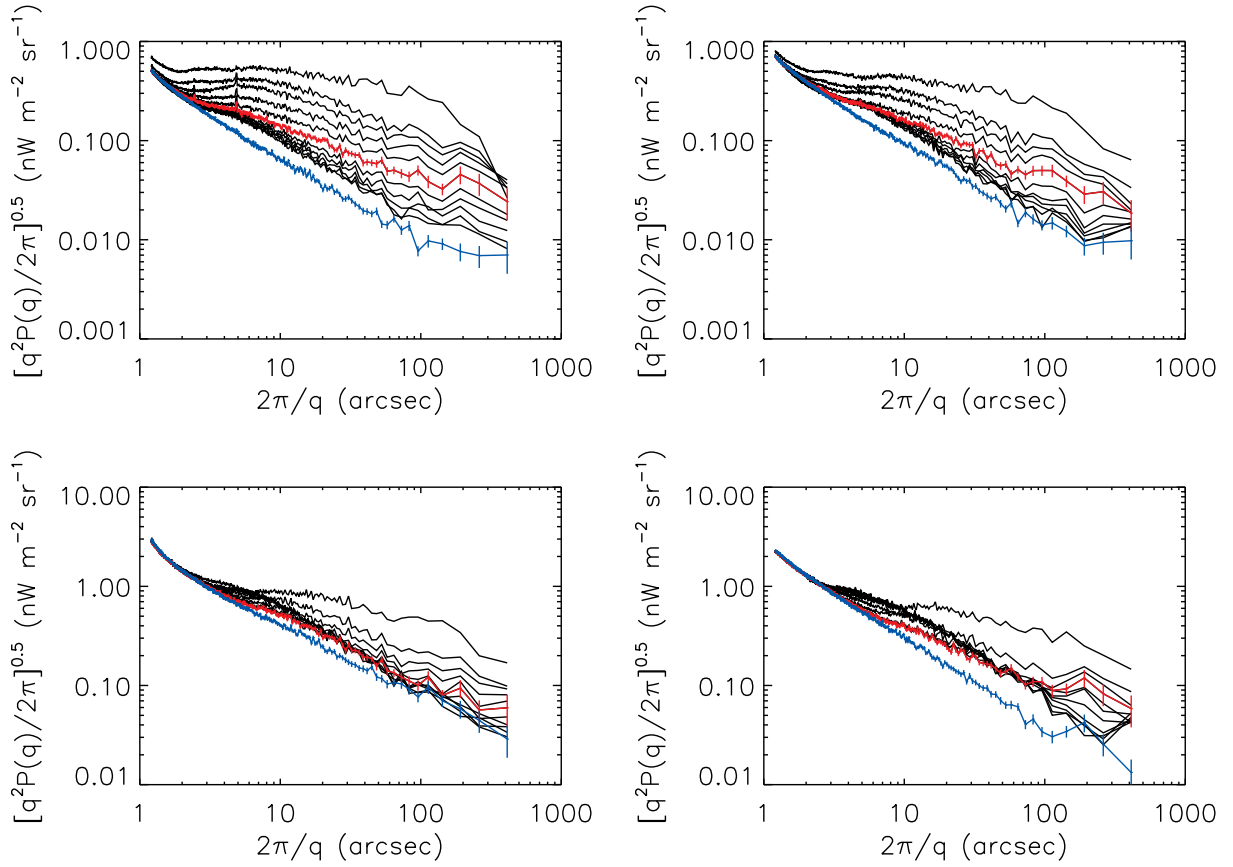


Fig. 8.— Fluctuation spectra as a function of model depth for the CDFS epoch 1 field. The red line indicates the optimal (zero skewness) model. The blue line indicates the $(A-B)/2$ noise fluctuations. The relative uncertainties at each model depth are similar to those that are depicted for the optimal model. Left to right and top to bottom are results for 3.6, 4.5, 5.8, and 8 μm respectively.

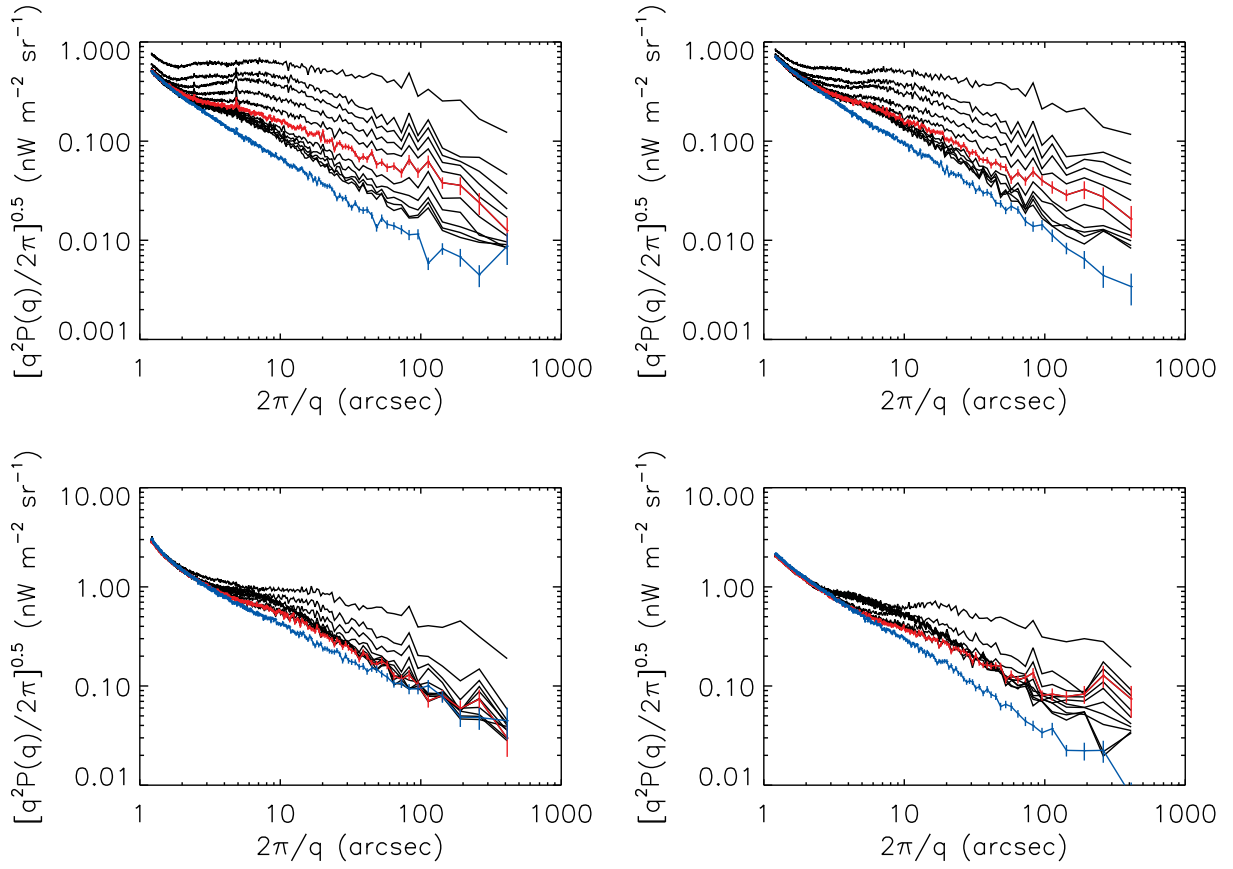


Fig. 9.— Same as Fig. 8, except for the CDFS epoch 2 field.

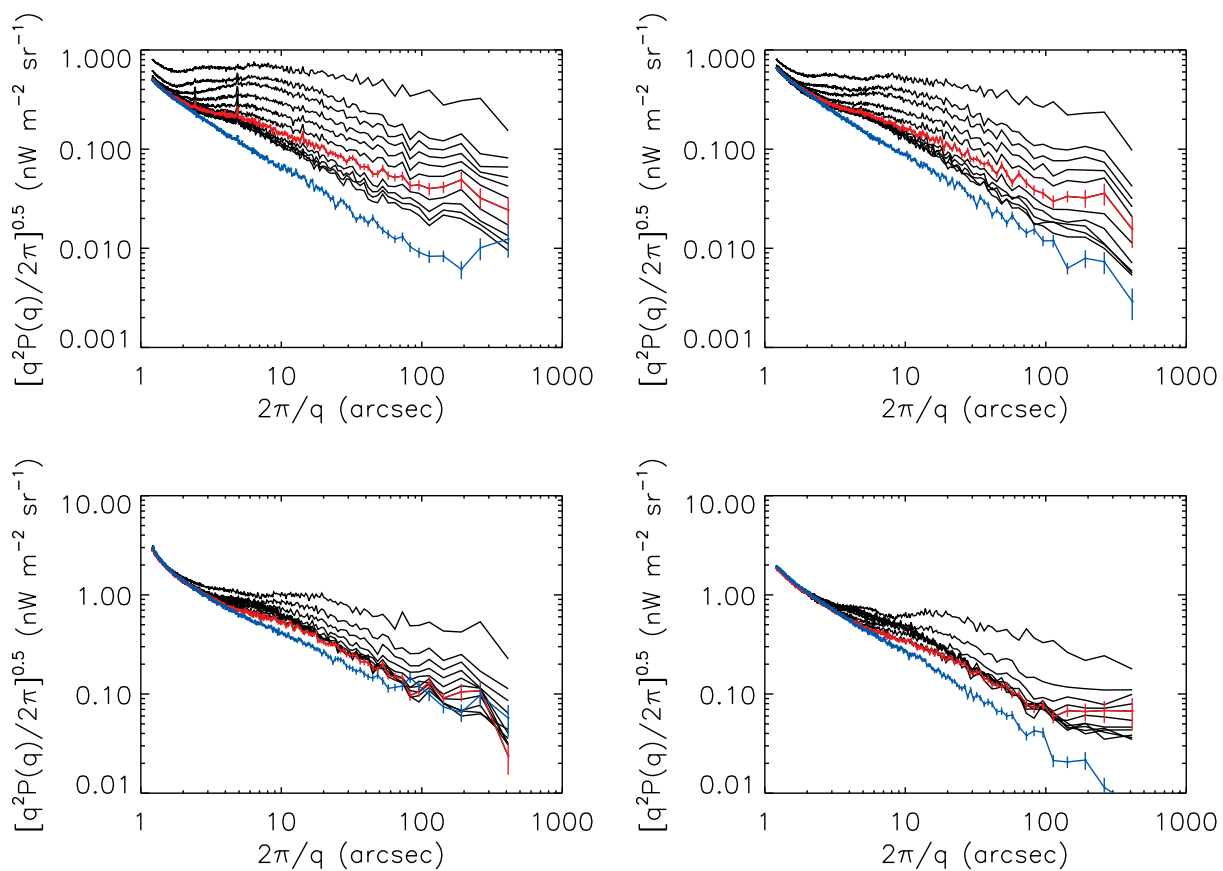


Fig. 10.— Same as Fig. 8, except for the HDFN epoch 1 field.

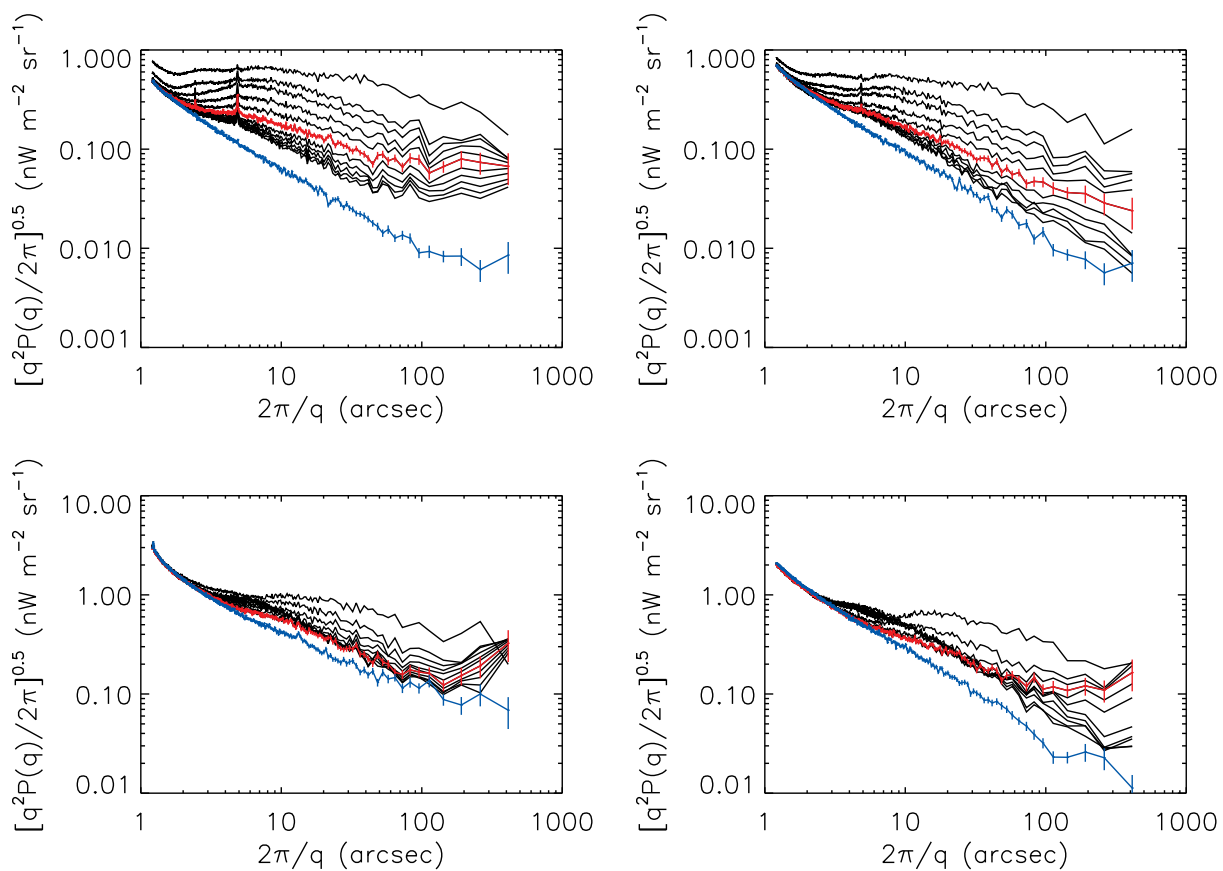


Fig. 11.— Same as Fig. 8, except for the HDFN epoch 2 field.

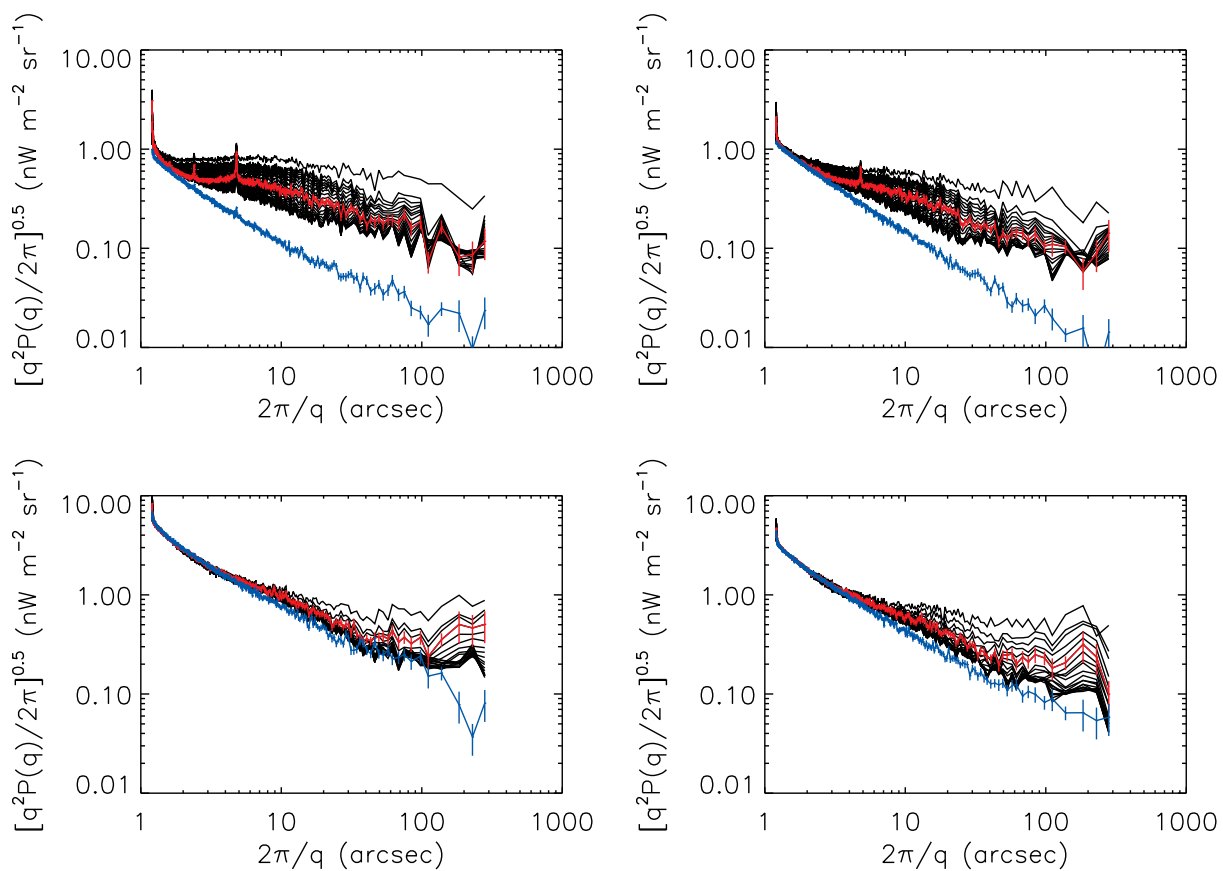


Fig. 12.— Same as Fig. 8, except for the QSO 1700 field.

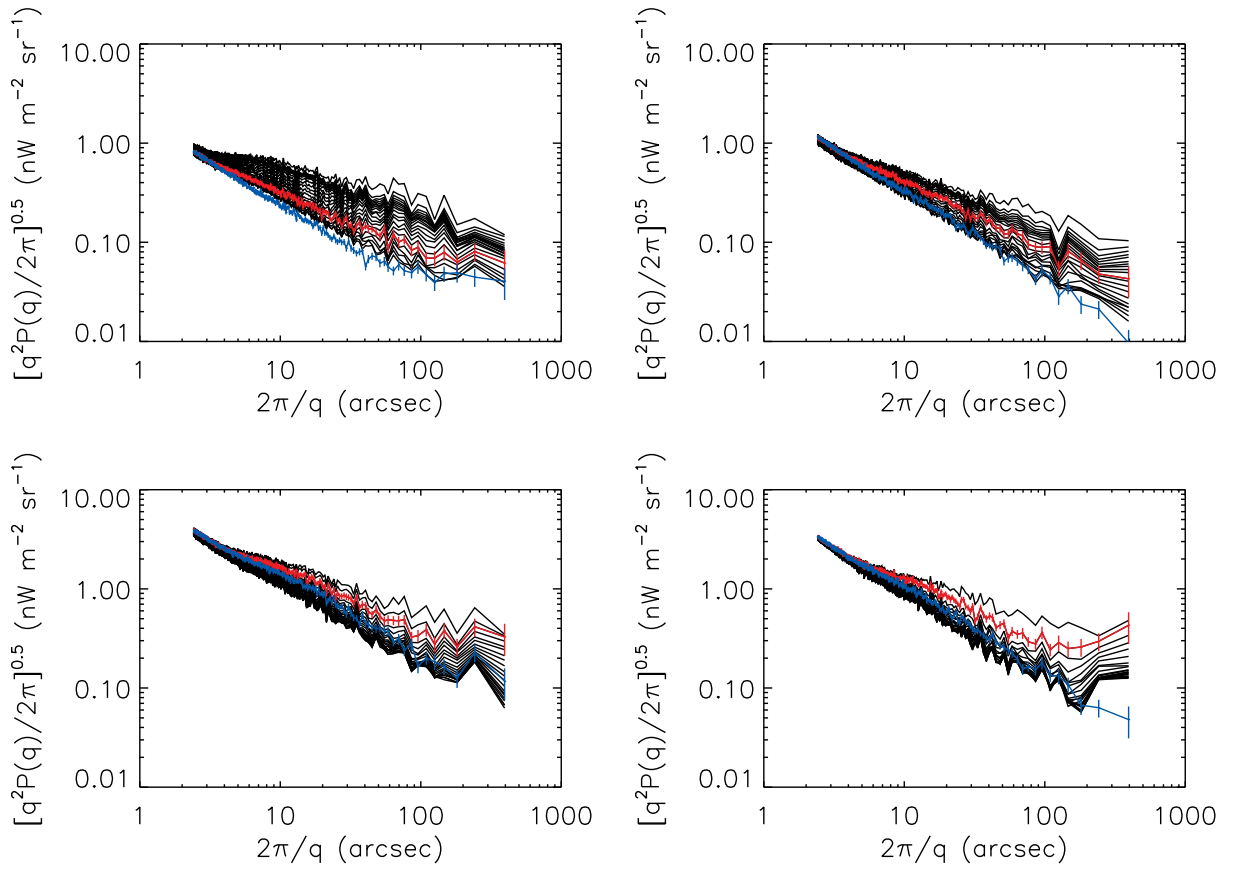


Fig. 13.— Same as Fig. 8, except for the EGS field.

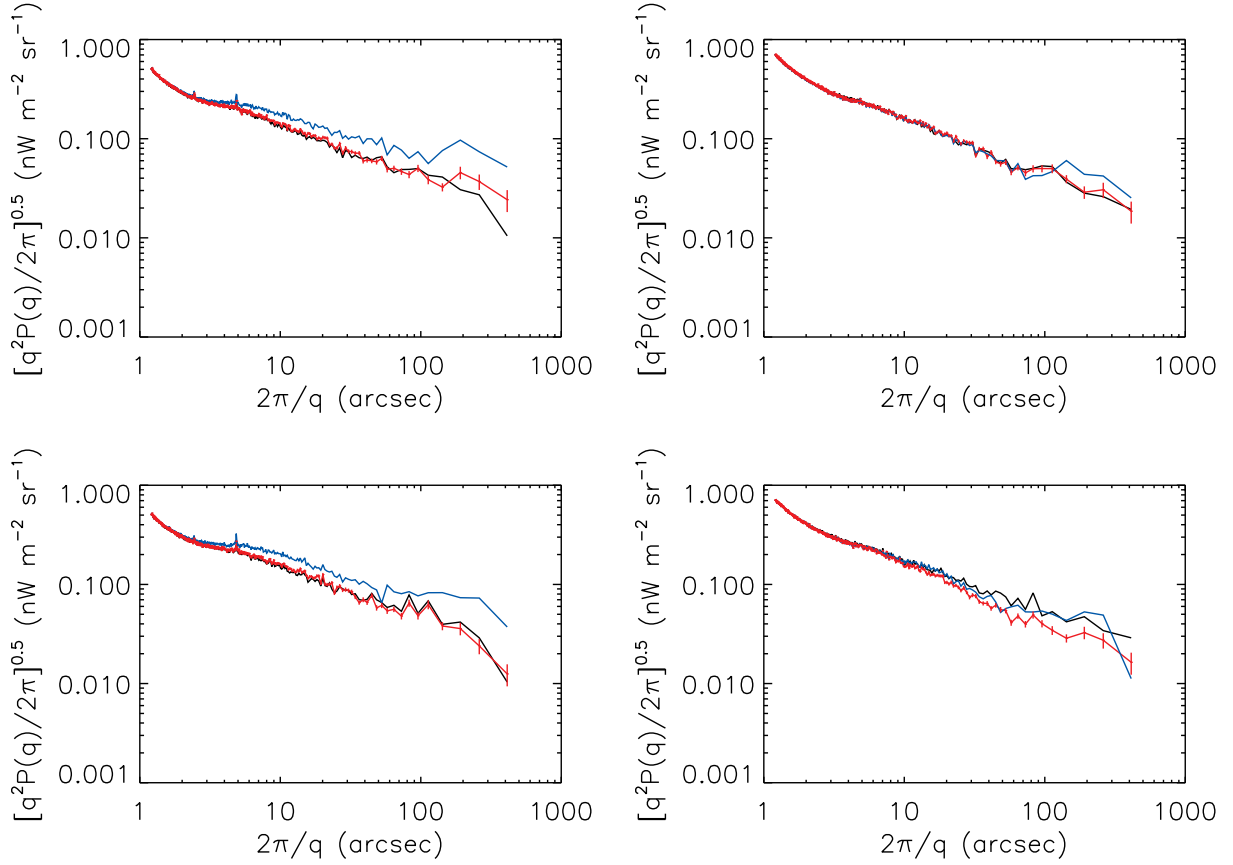


Fig. 14.— Fluctuation spectra as a function of PRF for the CDFS fields. The epoch 1 fields are shown in the top row, while epoch 2 are shown in the bottom. The left column shows $3.6 \mu\text{m}$ results, with $4.5 \mu\text{m}$ results in the right column. The red line indicates the optimal (zero skewness) model. The blue line indicates the wider PRF ($PRF^{0.95}$). The black line indicates the narrower PRF ($PRF^{1.05}$). A wider PRF would have been less effective at modeling and removing resolved sources at $3.6 \mu\text{m}$.

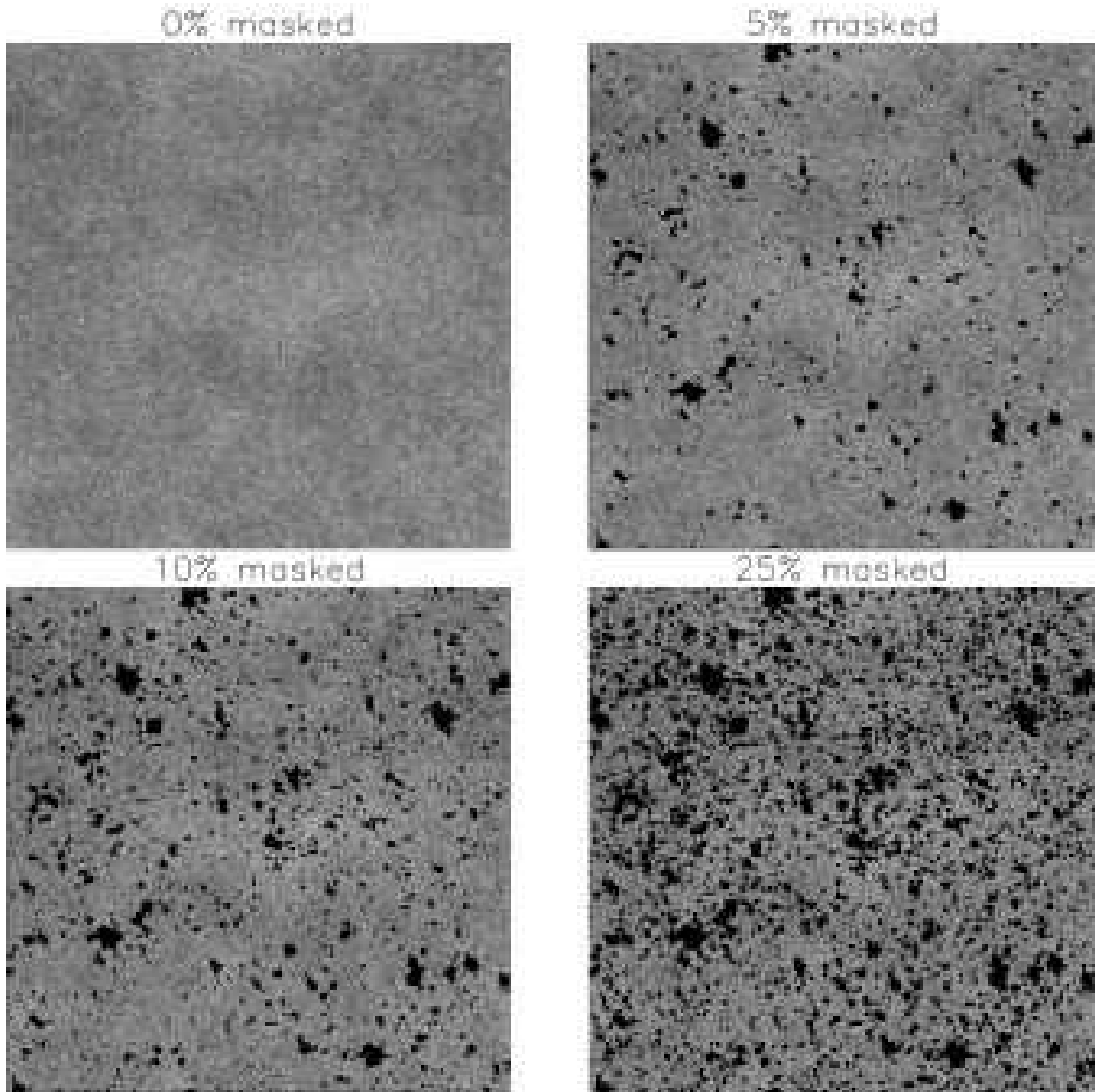


Fig. 15.— Simulated images containing large scales structure, shot noise, and instrument noise (but not with individually resolved sources), shown without any masking and with masking at 5, 10 and 25%. The 25% mask is from the actual observations, and the other masks are derived from it.

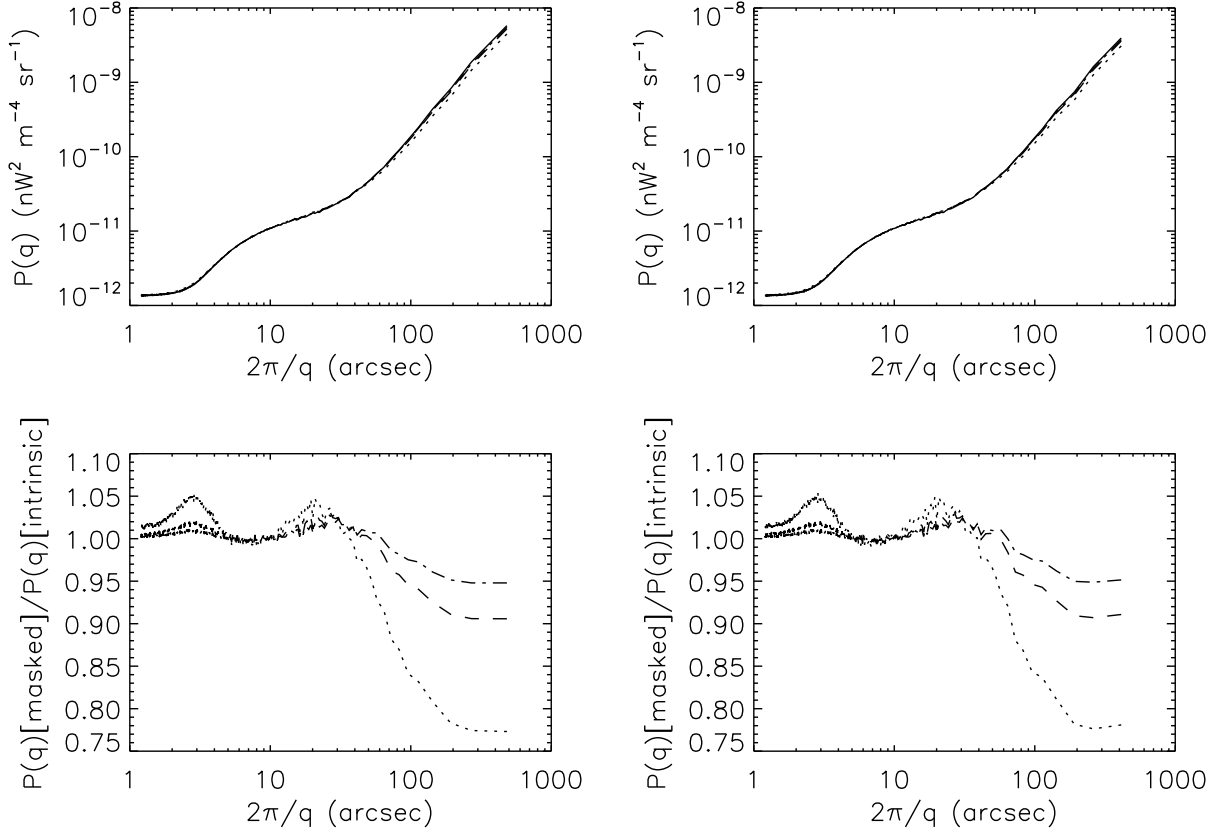


Fig. 16.— Mean power spectra of 160 simulated images with various amounts of masking (0% masked = solid lines, 5% masked = dot-dashed lines, 10% masked = dashed lines, 25% masked = dotted lines). The power spectra on the left include all power, while those on the right exclude power along the axes of the Fourier transforms. The lower panels reveal finer detail by normalizing the masked power spectra by the unmasked power spectra. At much higher levels of masking, a correlation function analysis would be immune from the spurious drop in large scale power that would occur in the power spectrum calculation (e.g. Kashlinsky 2007).

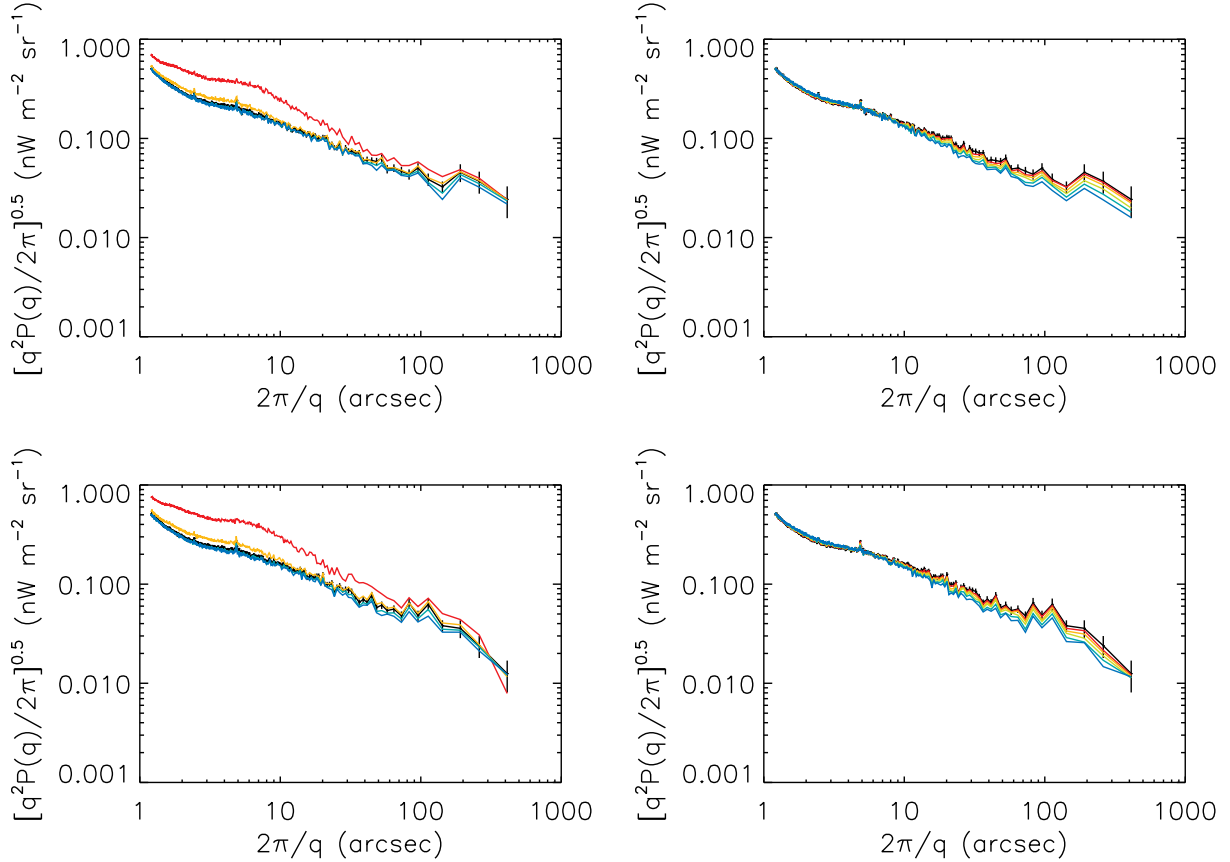


Fig. 17.— Fluctuation spectra of the CDFS field at $3.6 \mu\text{m}$ for various modifications of the source masking. The epoch 1 fields are shown in the top row, while epoch 2 are shown in the bottom. In the left column the black line represents the standard result. The orange and red lines indicate results where the clipping mask has been eroded by 1 and 2 pixels respectively, (i.e. decreasing amounts of clipped data). The green and blue lines indicate results where the clipping mask has been dilated by 1 and 2 pixels respectively, (i.e. increasing amounts of clipped data). In the right column the black line again represents the standard result. The red, orange, yellow, green and blue lines indicate results when an additional randomly placed 3×3 pixel masks are applied covering 10, 20, 30, 40, and 50 % of the total area respectively.

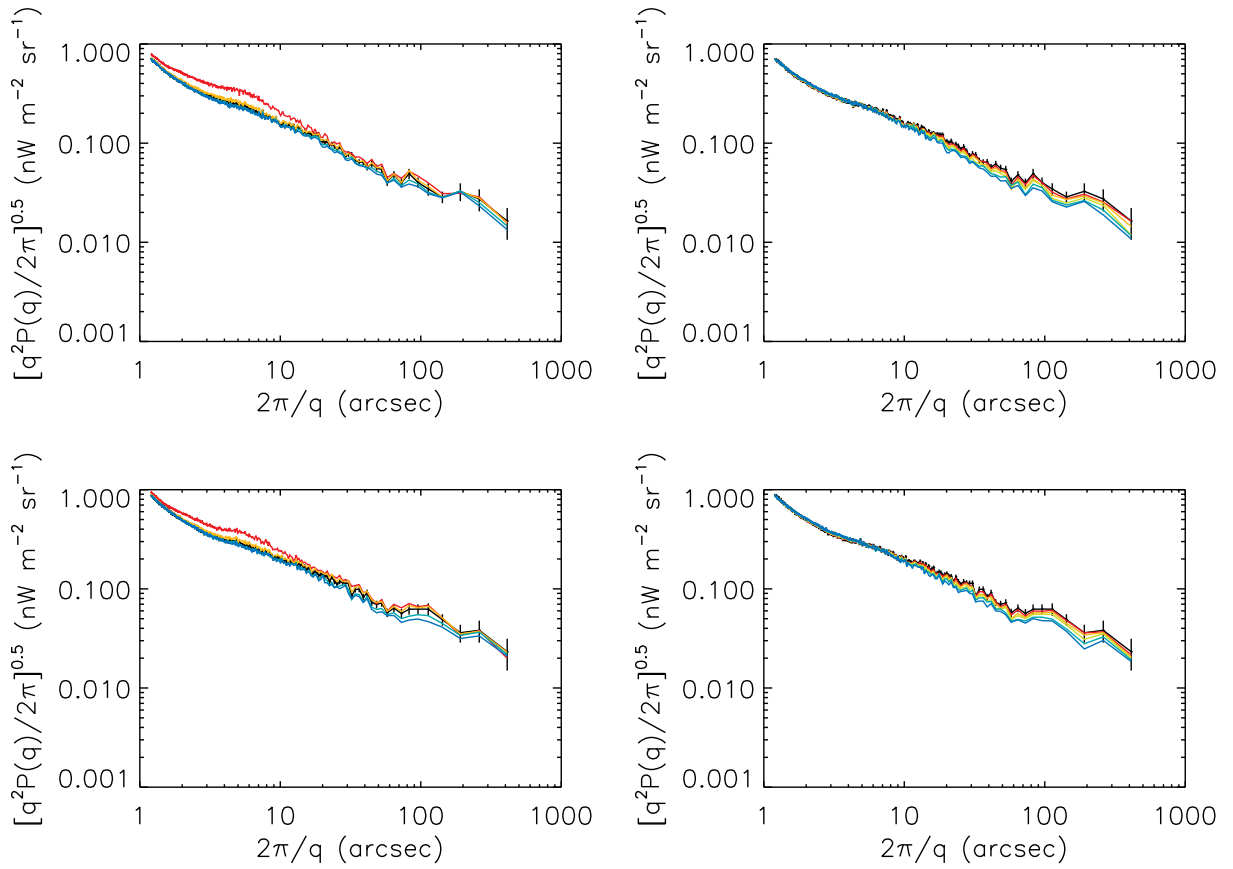


Fig. 18.— Same as Fig. 17, except for 4.5 μm .

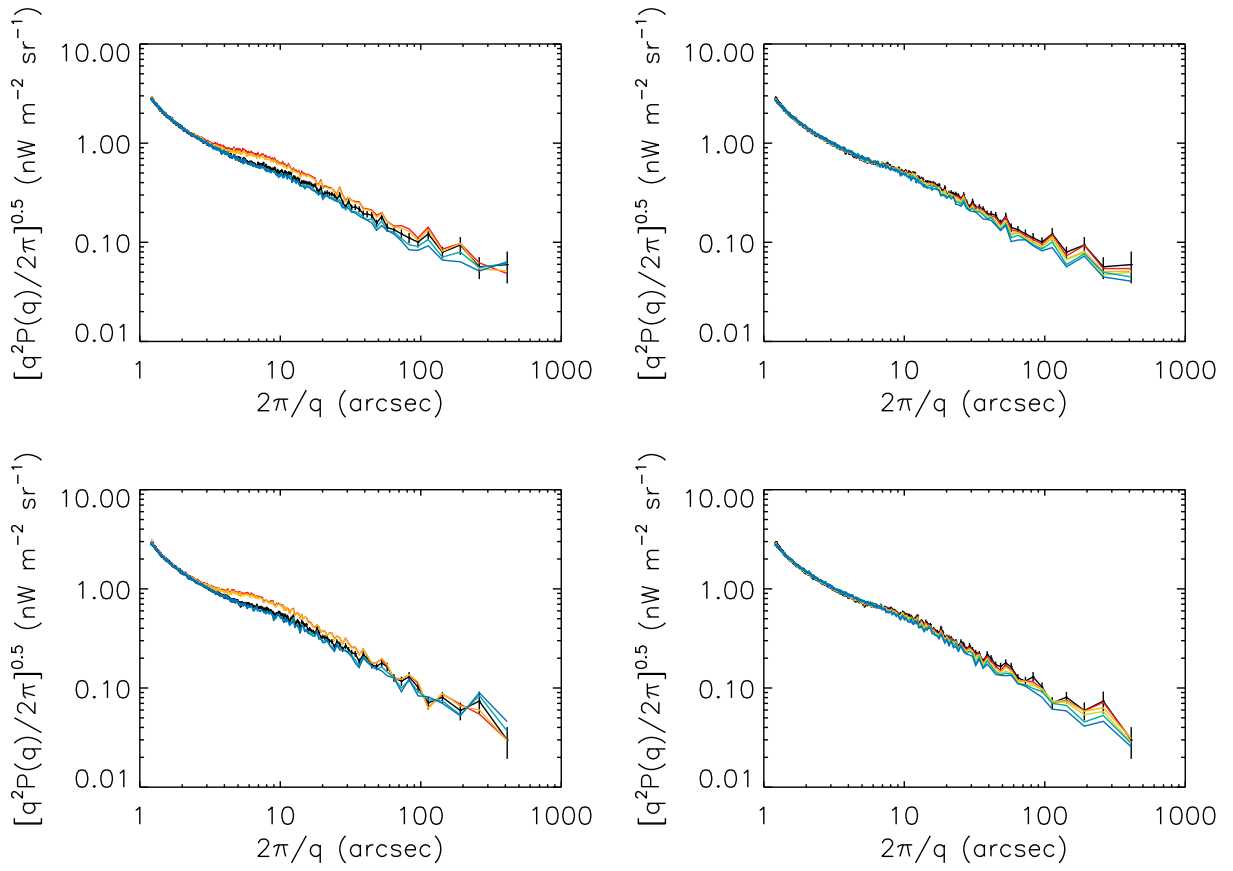


Fig. 19.— Same as Fig. 17, except for 5.8 μm .

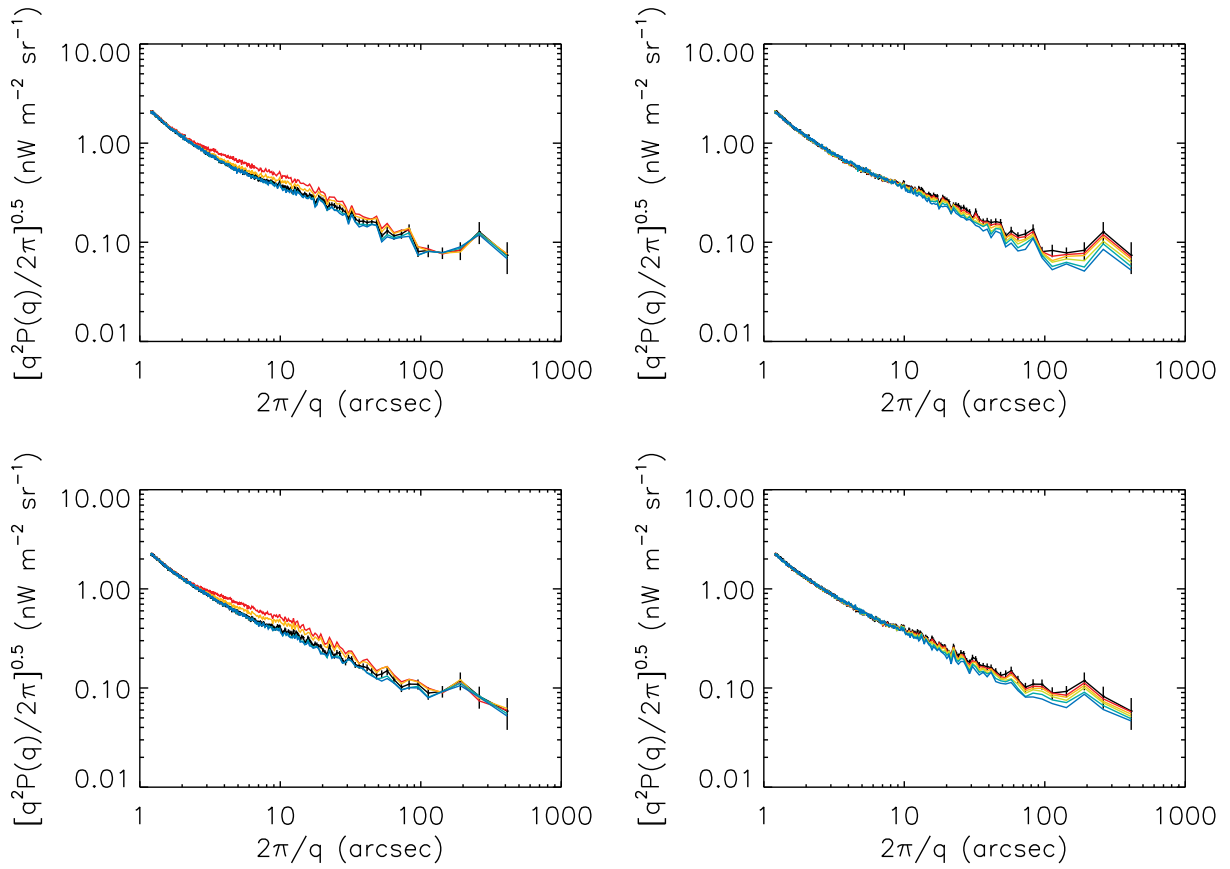


Fig. 20.— Same as Fig. 17, except for $8 \mu\text{m}$.

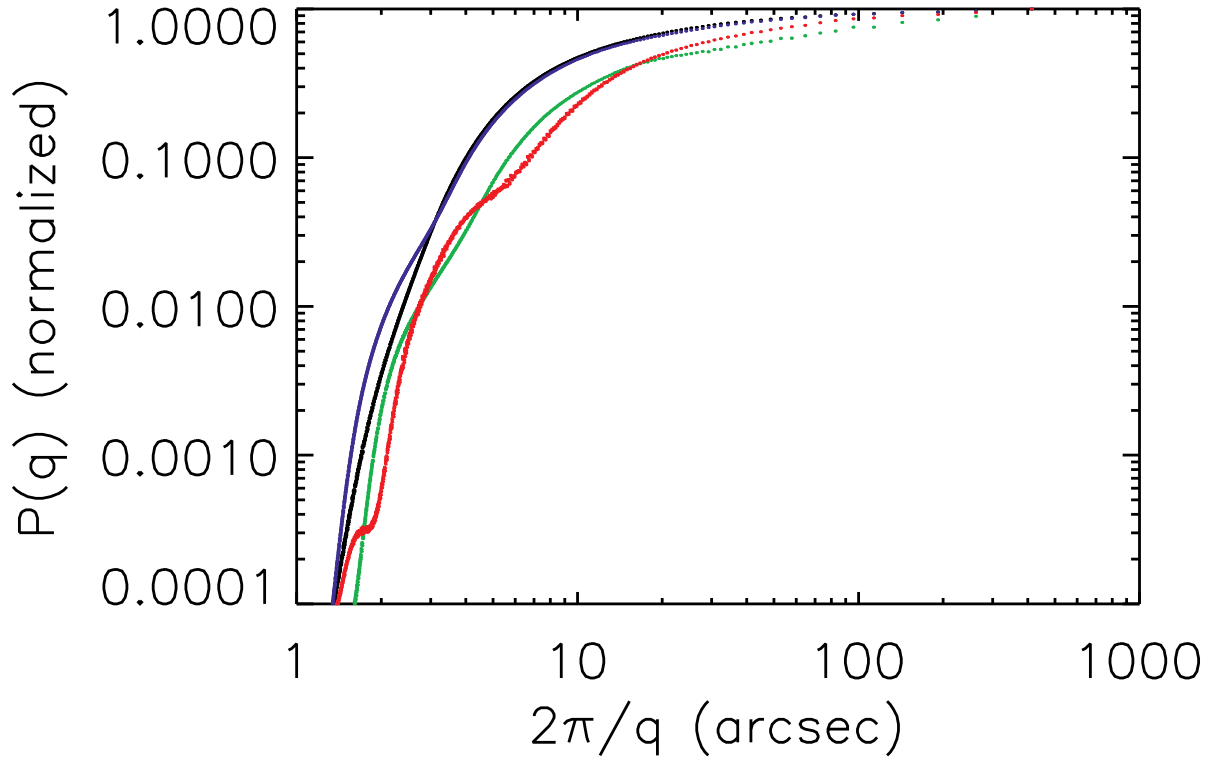


Fig. 21.— Power spectra of the IRAC PRFs. Black, blue, green, and red symbols represent 3.6, 4.6, 5.8 and 8 μm PRFs respectively. Celestial components of the power spectrum will be modulated by these functions; other (e.g. instrumental) components of the power spectrum will not.

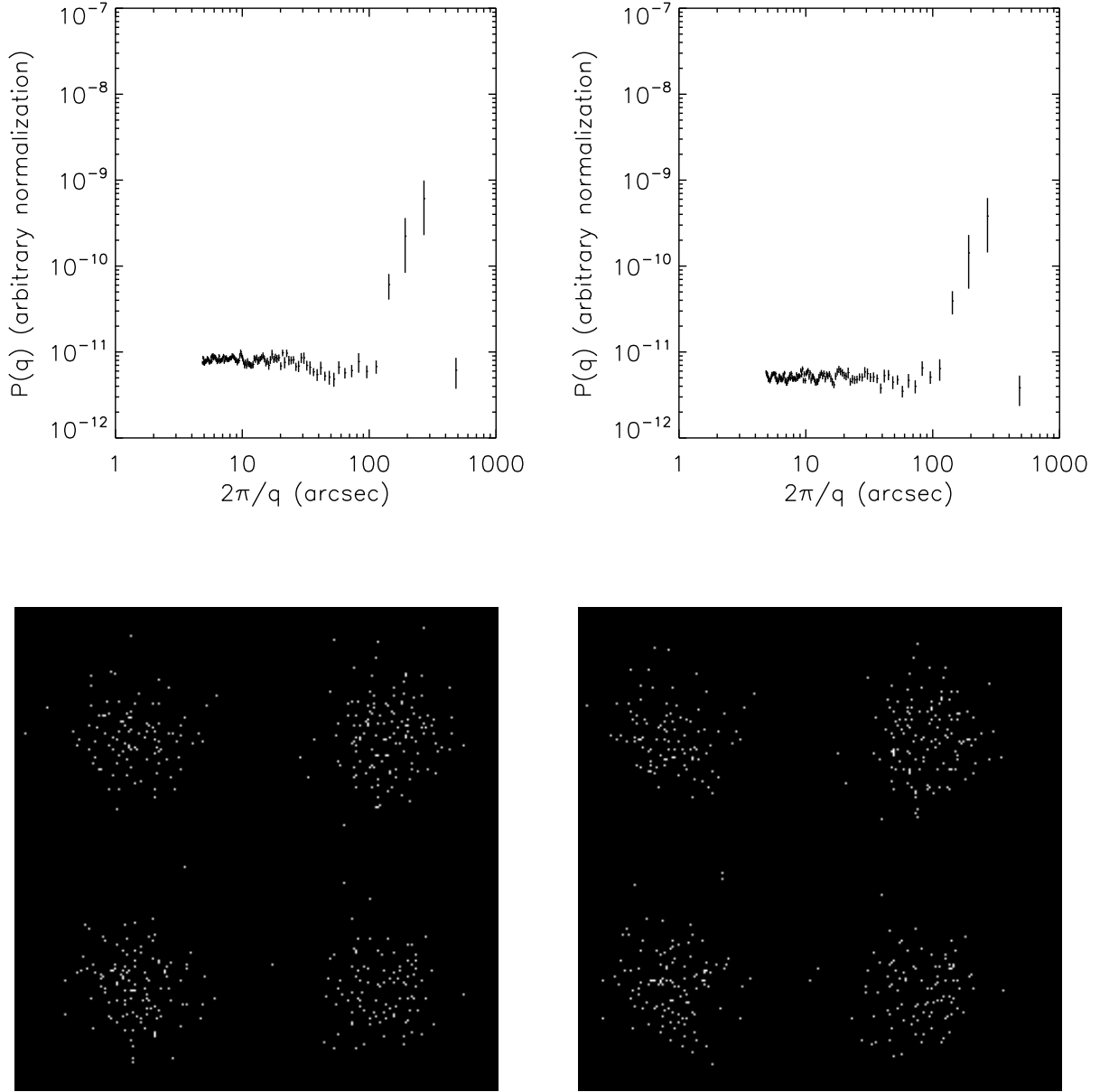


Fig. 22.— Power spectra of the CDFS-e1 dither patterns at 3.6 (left) and 4.5 (right) μm . Excess power appears only at scales 150 – 330'', which is caused by the clustering of pointings within the 2×2 instrument fields of view required to mosaic the entire field. The lower panels depict the net dither patterns for all AORs covering this field.

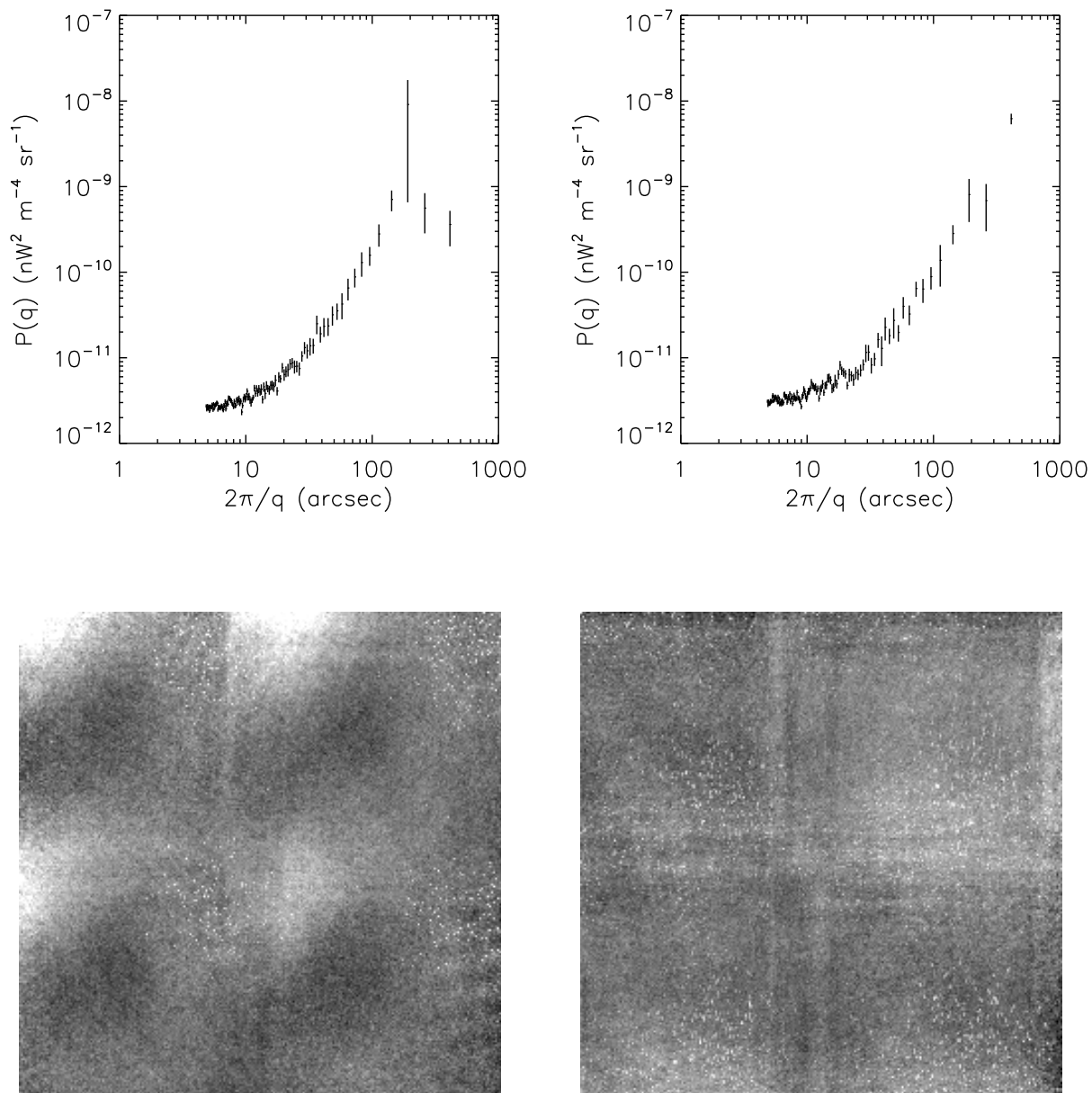


Fig. 23.— Power spectra of the CDFS-e1 offsets at 3.6 (left) and 4.5 (right) μm , as reprojected onto the sky by the net dither pattern (Fig. 22). These artificial images are shown in the bottom row, with the corresponding power spectra at the top (range = $[-1,1]$ $\text{nW m}^{-1} \text{sr}^{-2}$). Note the strong similarities with the GOODS-processed image in Fig. 5.

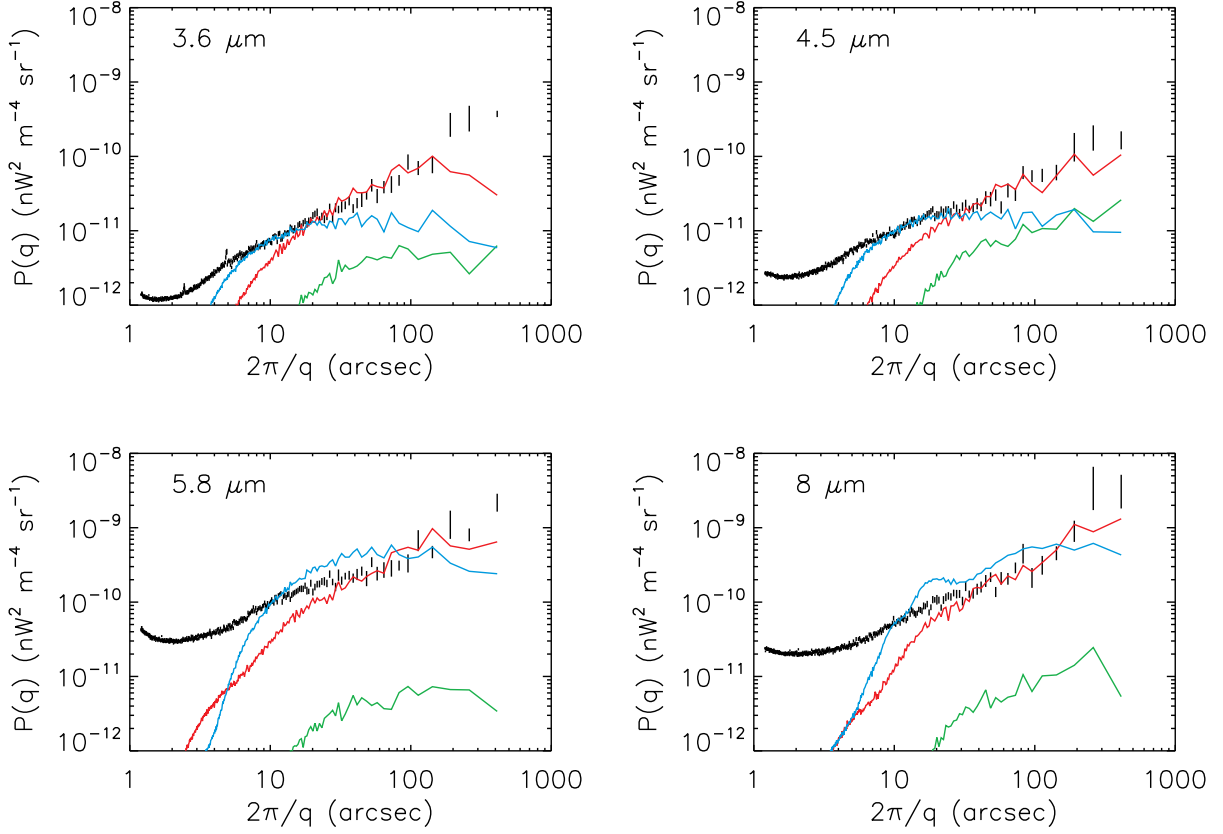


Fig. 24.— Power spectra of artificial CDFS-e1 images compared to that of the actual CIB. The black points with 1σ error bars are the CIB power spectrum. The red line indicates the power spectrum of the clipping mask, arbitrarily normalized to match at scales $2\pi/q > 30''$. The cyan line indicates the power spectrum of the sources that are masked (i.e. using the inverse of the nominal clipping mask), arbitrarily normalized to match at scales $8'' < 2\pi/q < 15''$. The green line indicates the power spectrum of the “halo” test image, based on the clipping mask. In this case, the power is appropriately scaled according to the (small) correlation between the halo image and the actual CIB fluctuations.

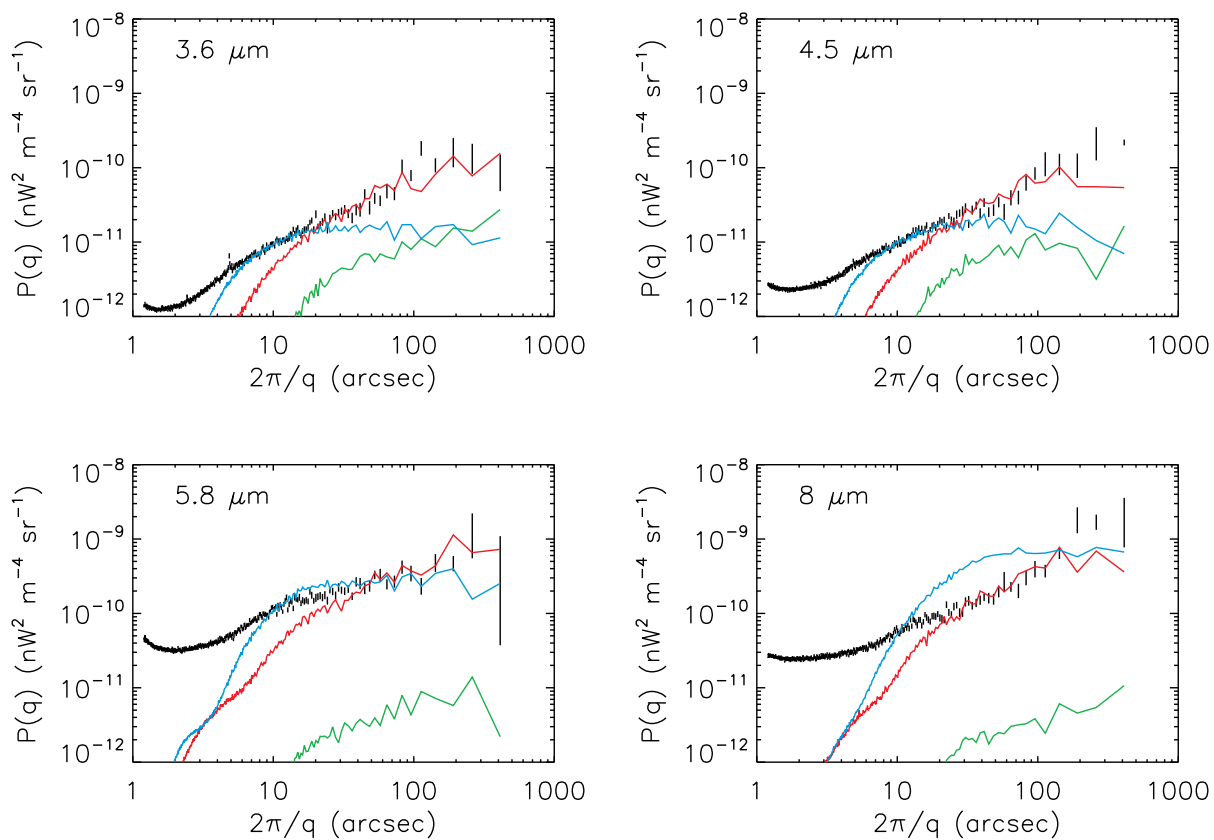


Fig. 25.— Same as Fig. 24, except for the CDFS-e2 field.

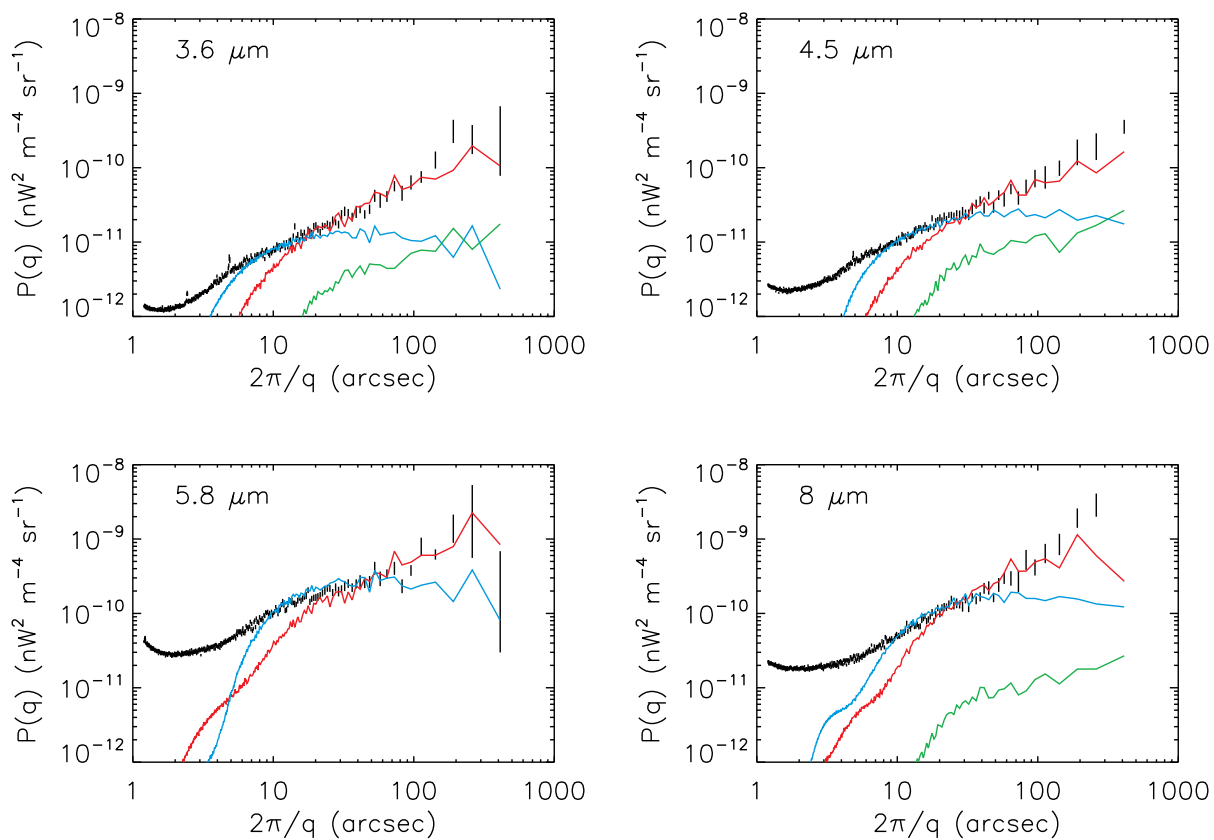


Fig. 26.— Same as Fig. 24, except for the HDFN-e1 field.

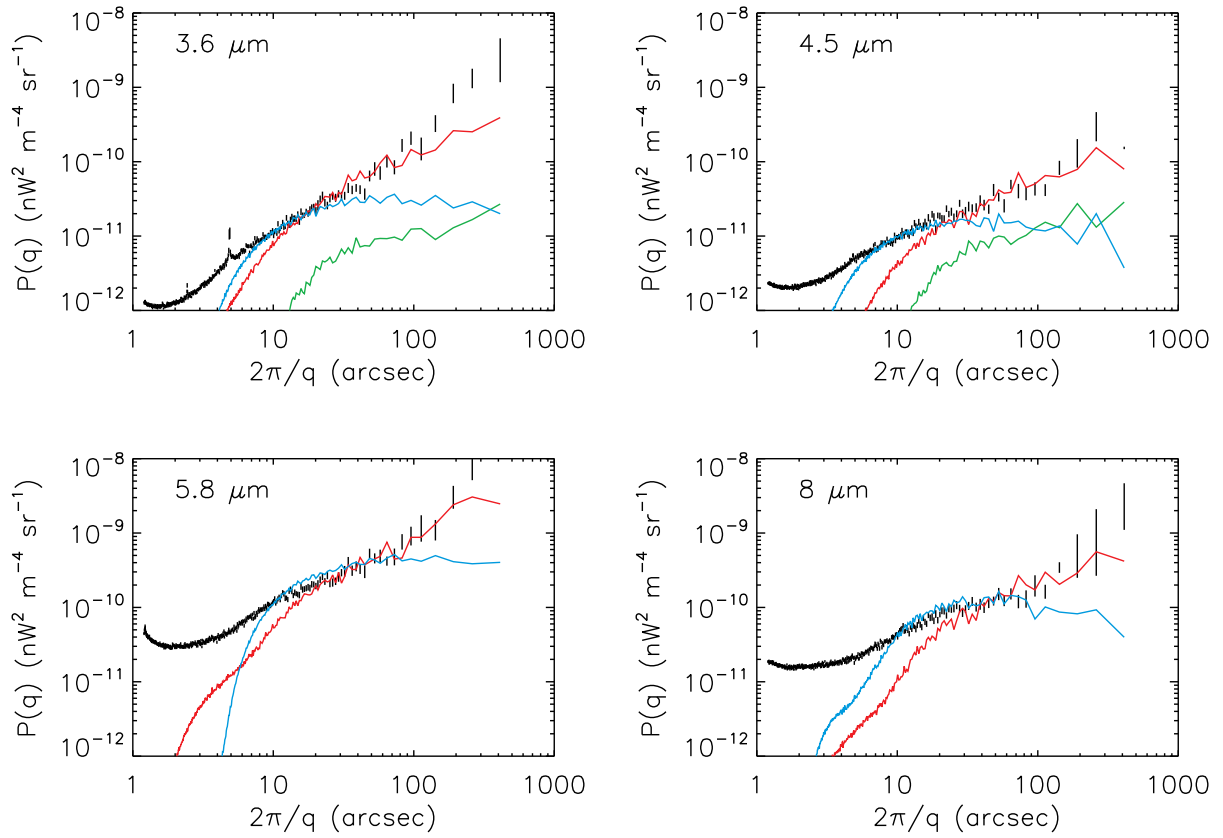


Fig. 27.— Same as Fig. 24, except for the HDFN-e2 field.

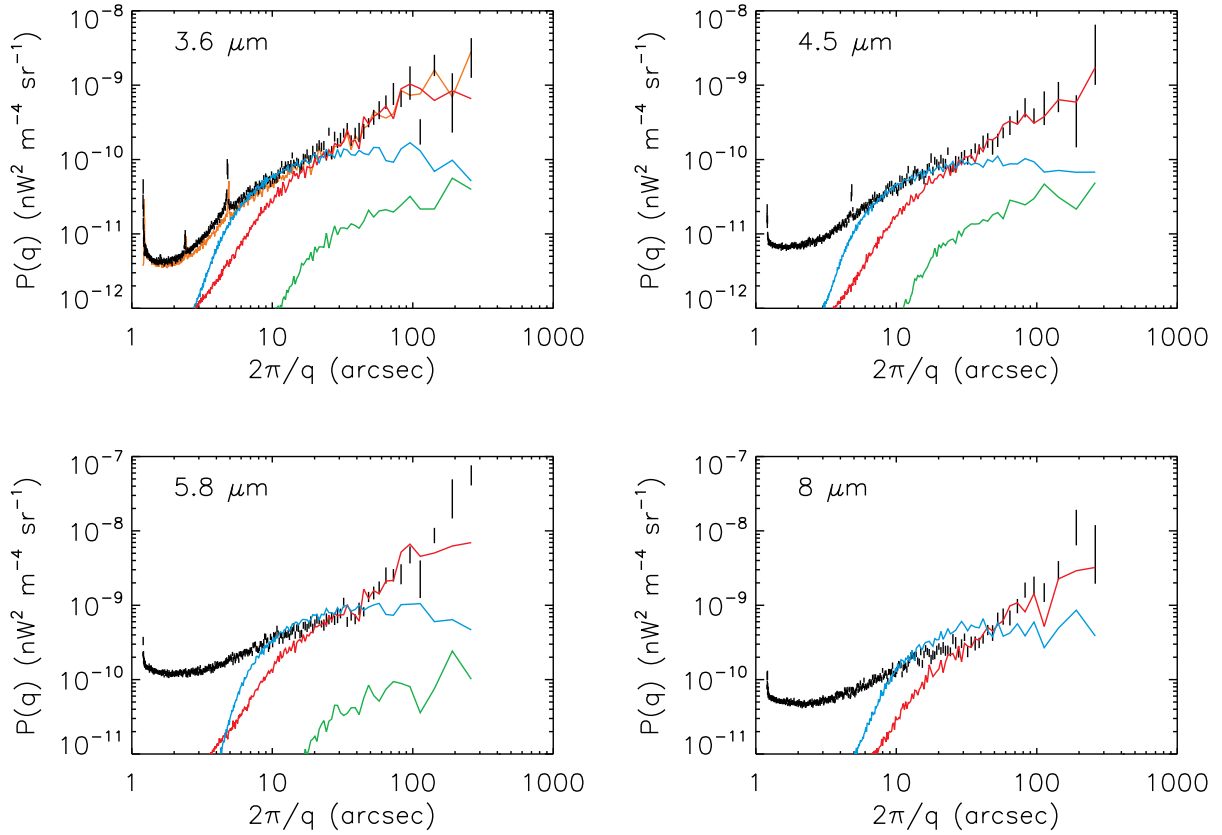


Fig. 28.— Same as Fig. 24, except for the QSO 1700 field. The additional orange line in the $3.6 \mu\text{m}$ panel shows the power spectrum derived when the processing starts with BCD frames (as for the other fields) rather than the raw data. Differences are generally $< 2\sigma$, except at scales $2'' < 2\pi/q < 10''$.

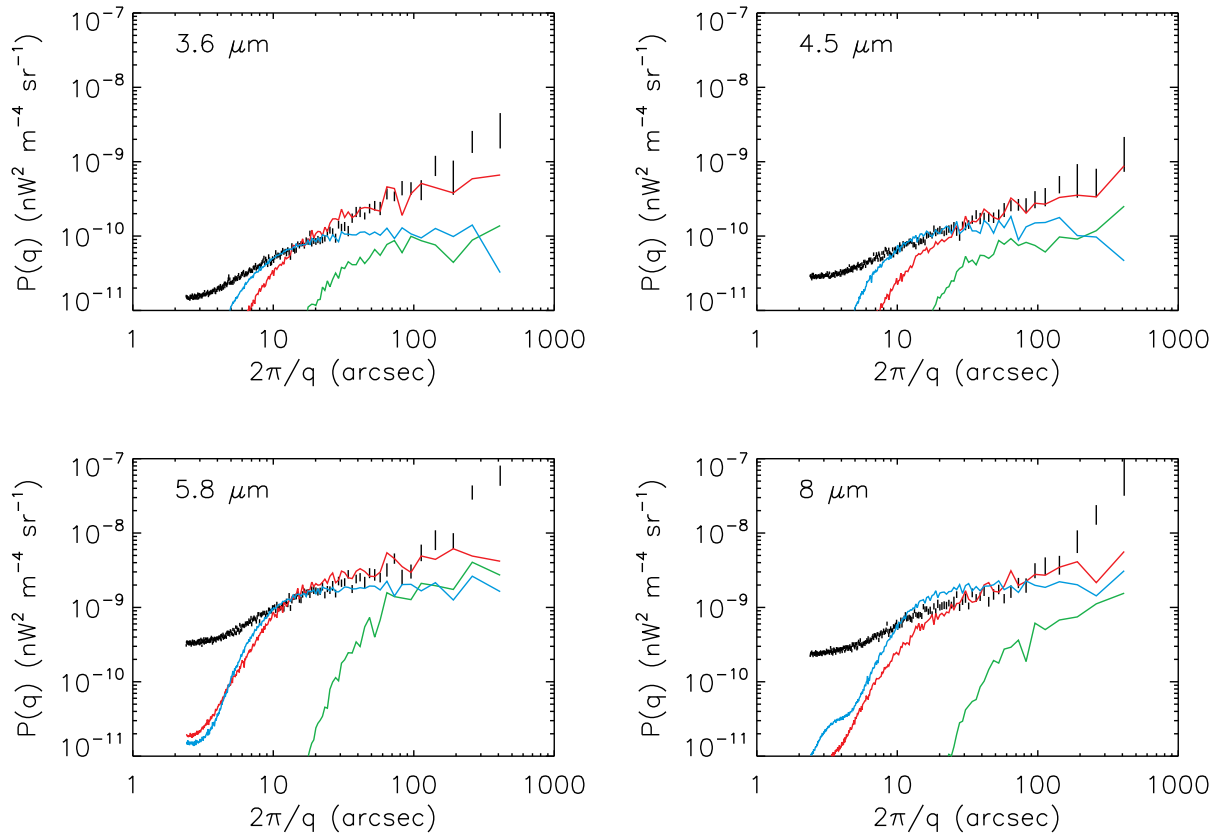


Fig. 29.— Same as Fig. 24, except for the EGS field.

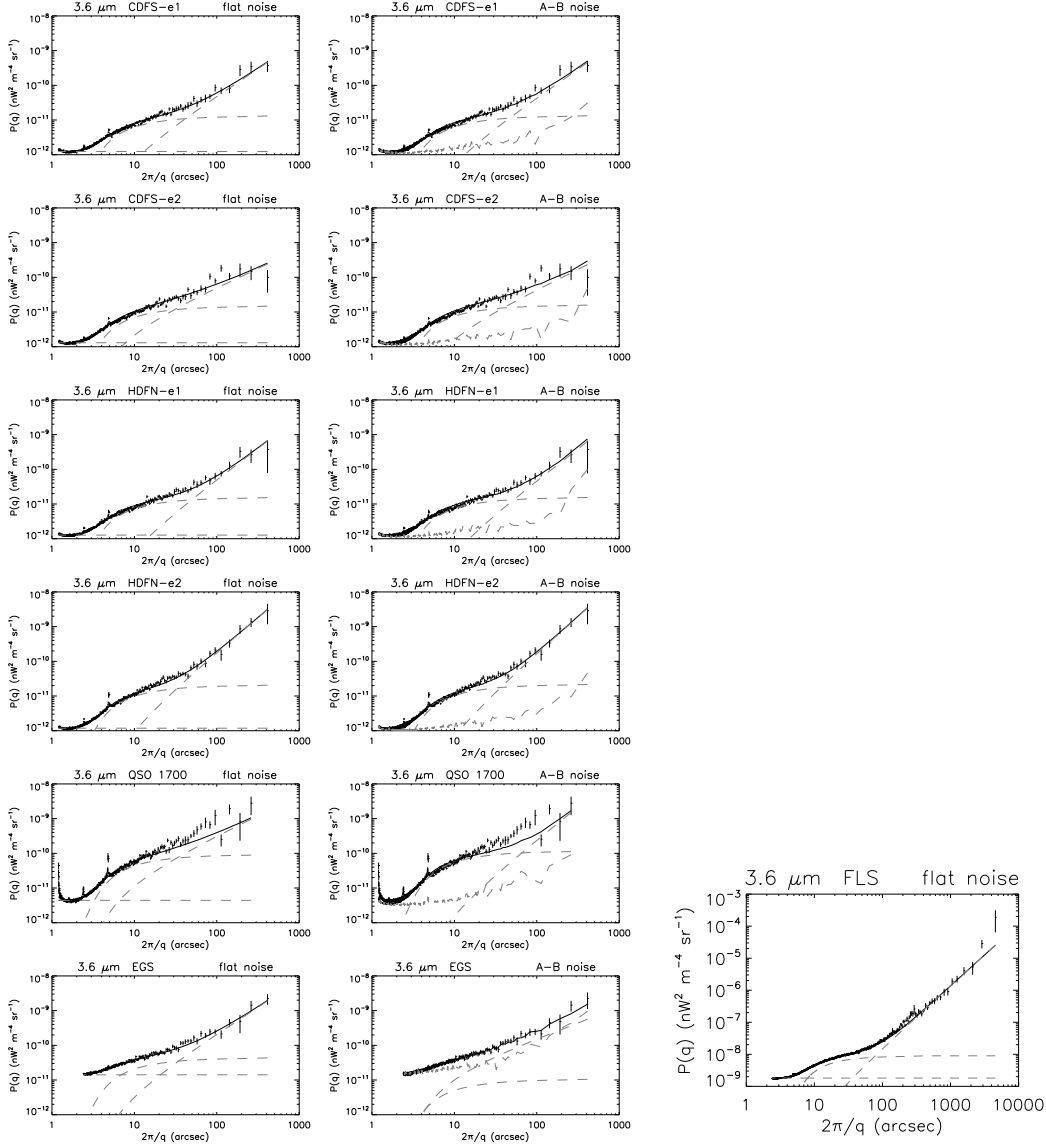


Fig. 30.— Fits to the $3.6 \mu\text{m}$ power spectra for our six main fields, and the FLS. The left column shows fits as characterized by Equation (4): (a) flat instrument noise components, (b) a flat shot noise component convolved with the PRF, and (c) a power law component, also convolved with the PRF. The solid line indicates the sum of these three components (dashed lines). The middle column shows the fits as characterized by Equation (5), where the measured $(A-B)/2$ noise takes the place of the flat instrument noise component. The FLS result for the flat noise fit is shown separately, as it spans a different range of angular scale and power than the other fields.

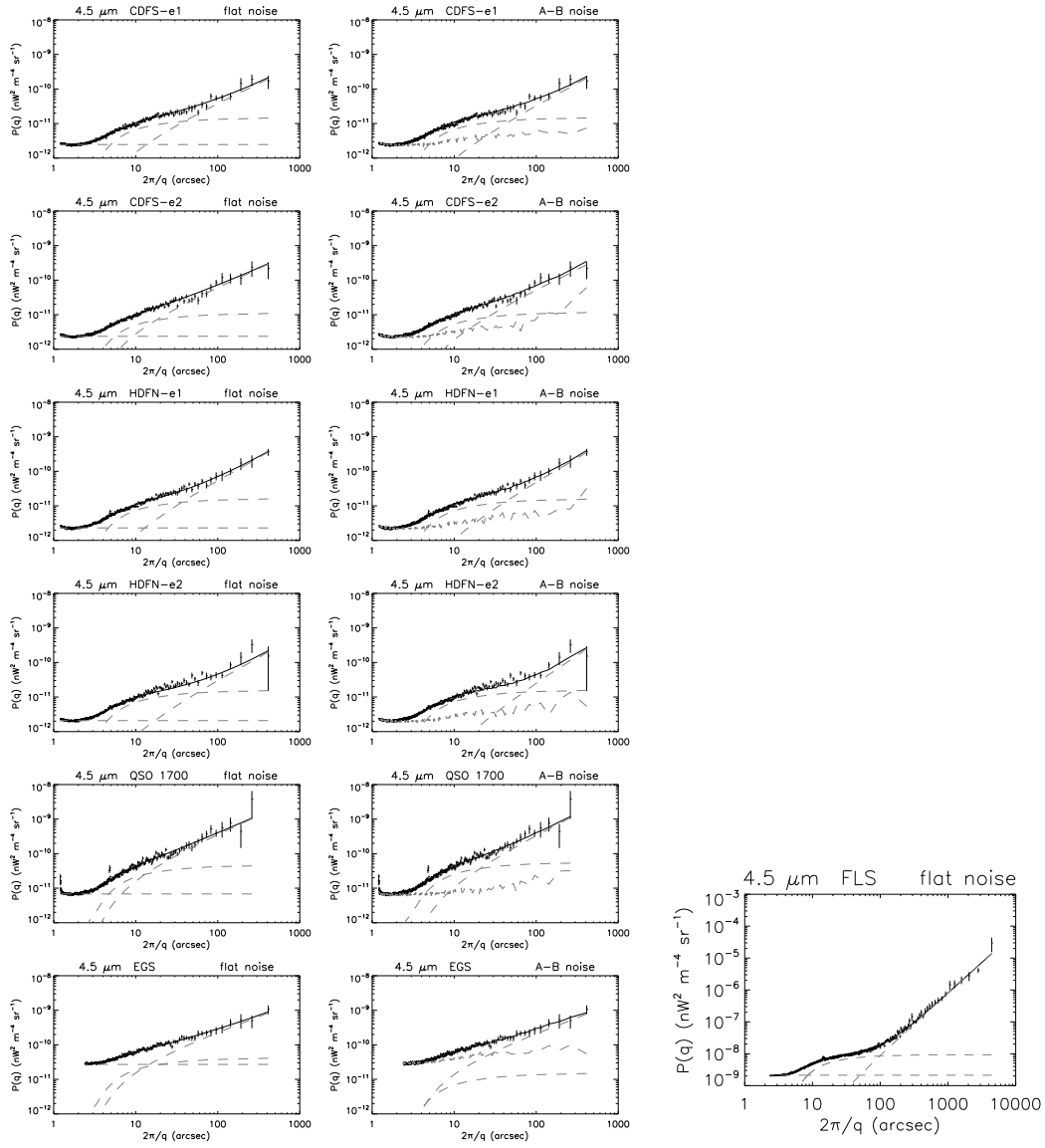


Fig. 31.— Same as Fig. 30, except for 4.5 μm .

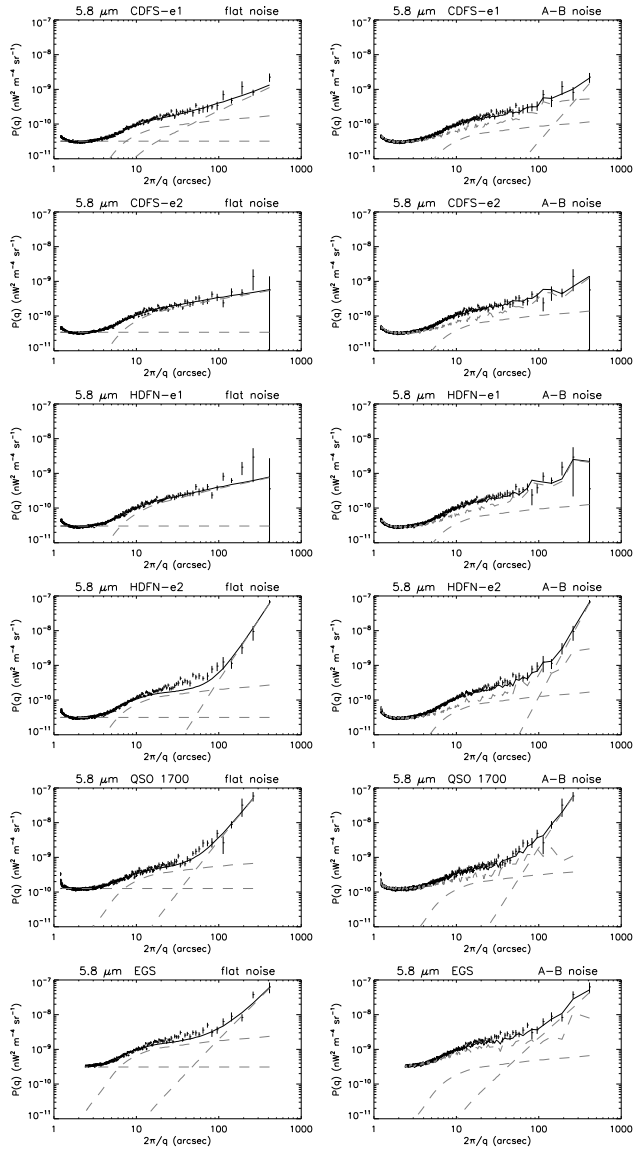


Fig. 32.— Same as Fig. 30, except for $5.8 \mu\text{m}$, and without FLS results.

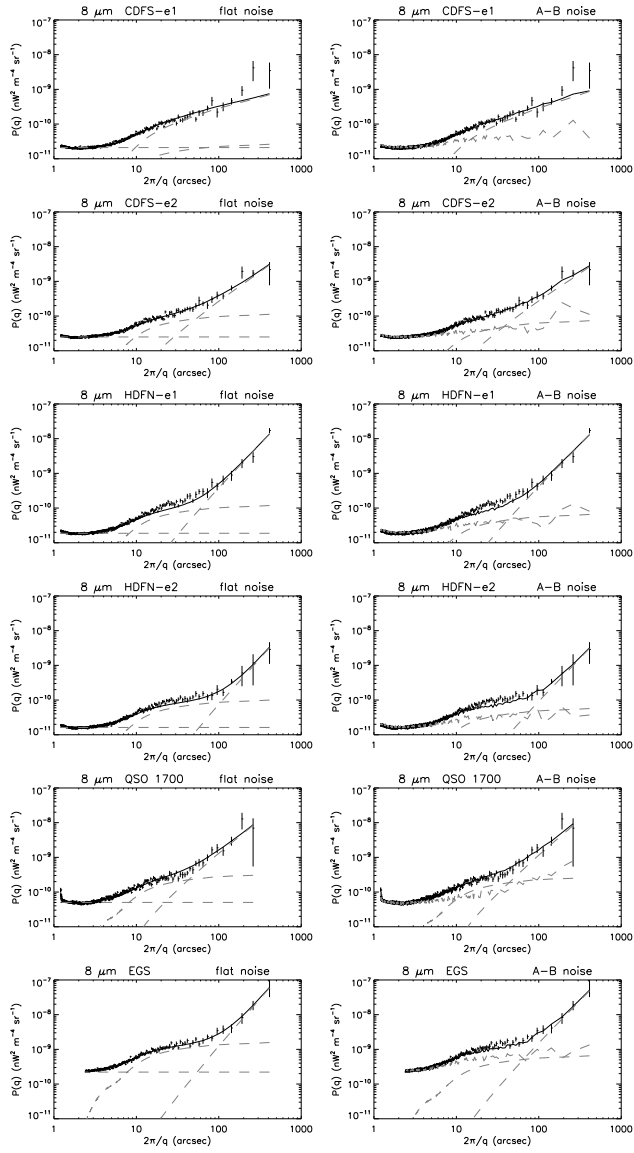


Fig. 33.— Same as Fig. 30, except for $8 \mu\text{m}$, and without FLS results.

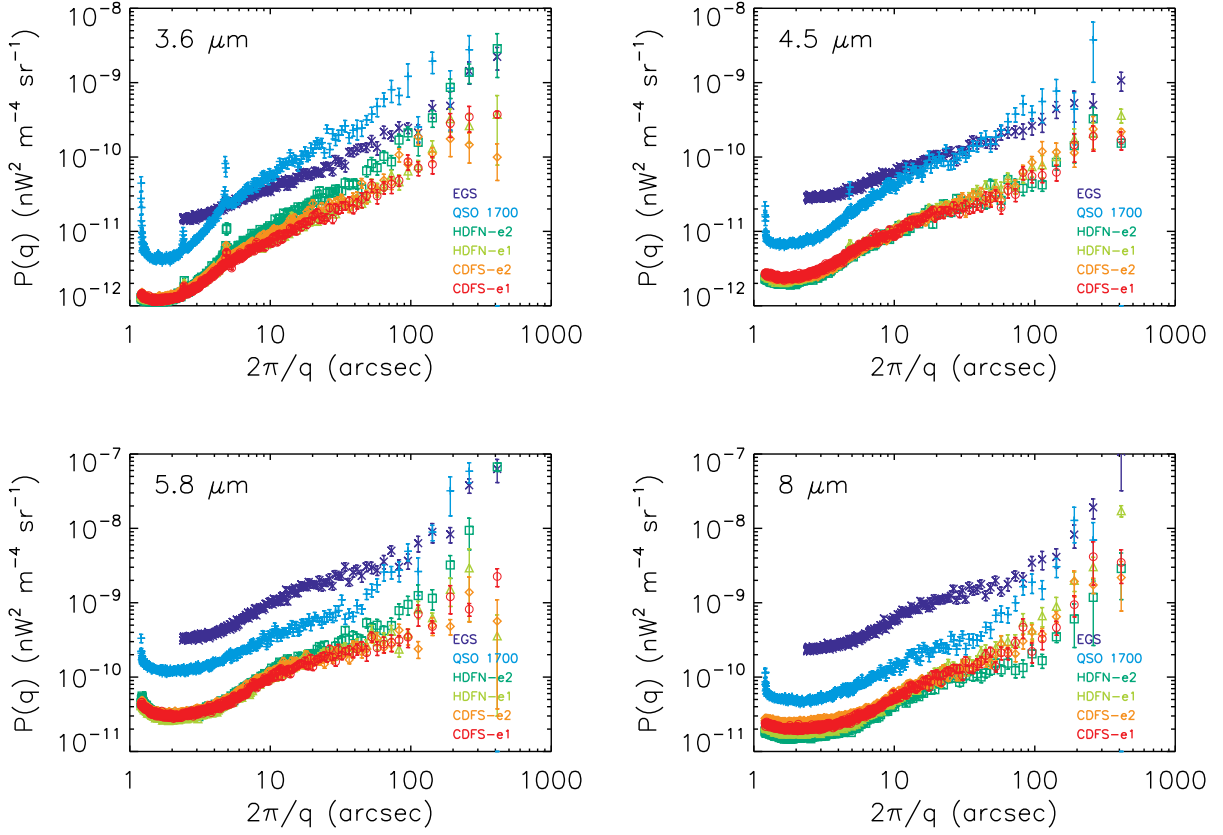


Fig. 34.— Final power spectra for the different fields. This figure provides a more visual comparison of similarities and difference between the power spectra than the numerical details of Tables 3 and 4. The FLS results are not shown due to their different ranges of spatial scale and power.

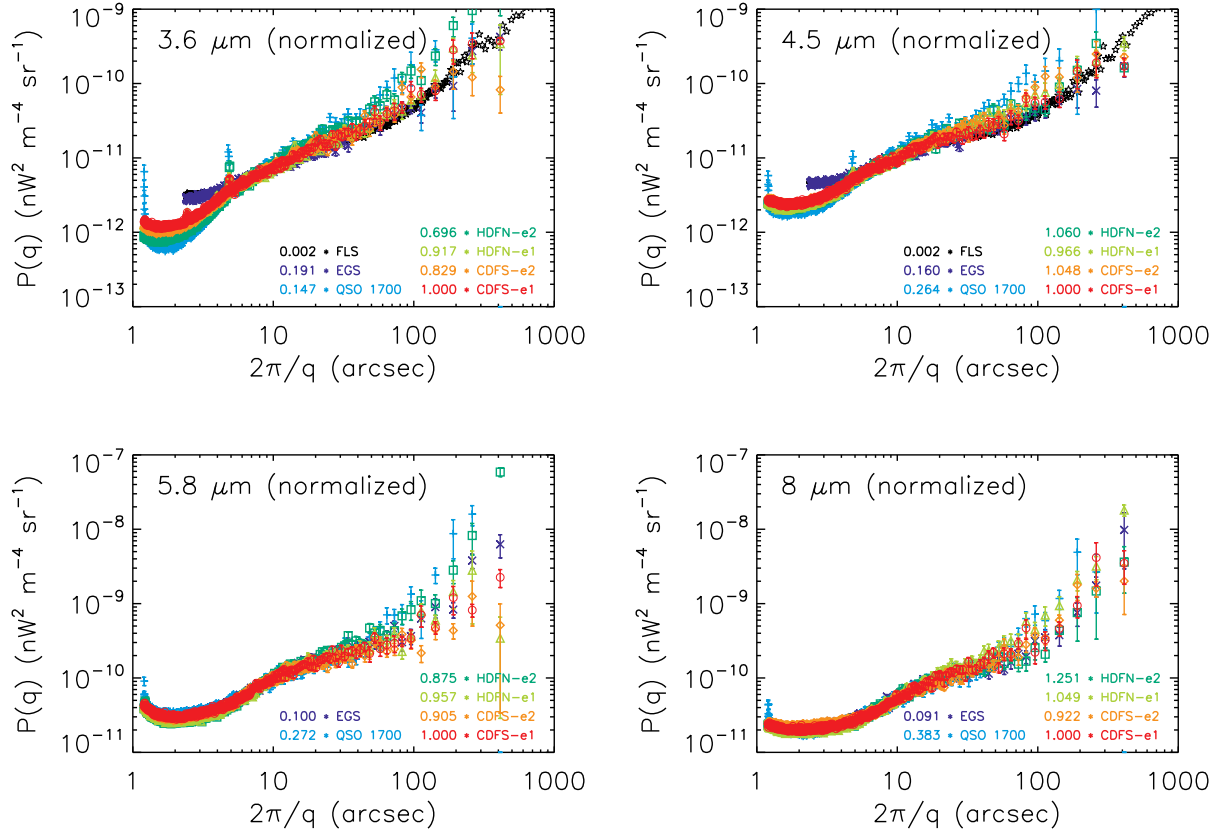


Fig. 35.— Final power spectra for the different fields, after normalizing all spectra to match that of the CDFS-e1 at $2\pi/q > 5''$. The figure legends cite the normalization factors required for each field.

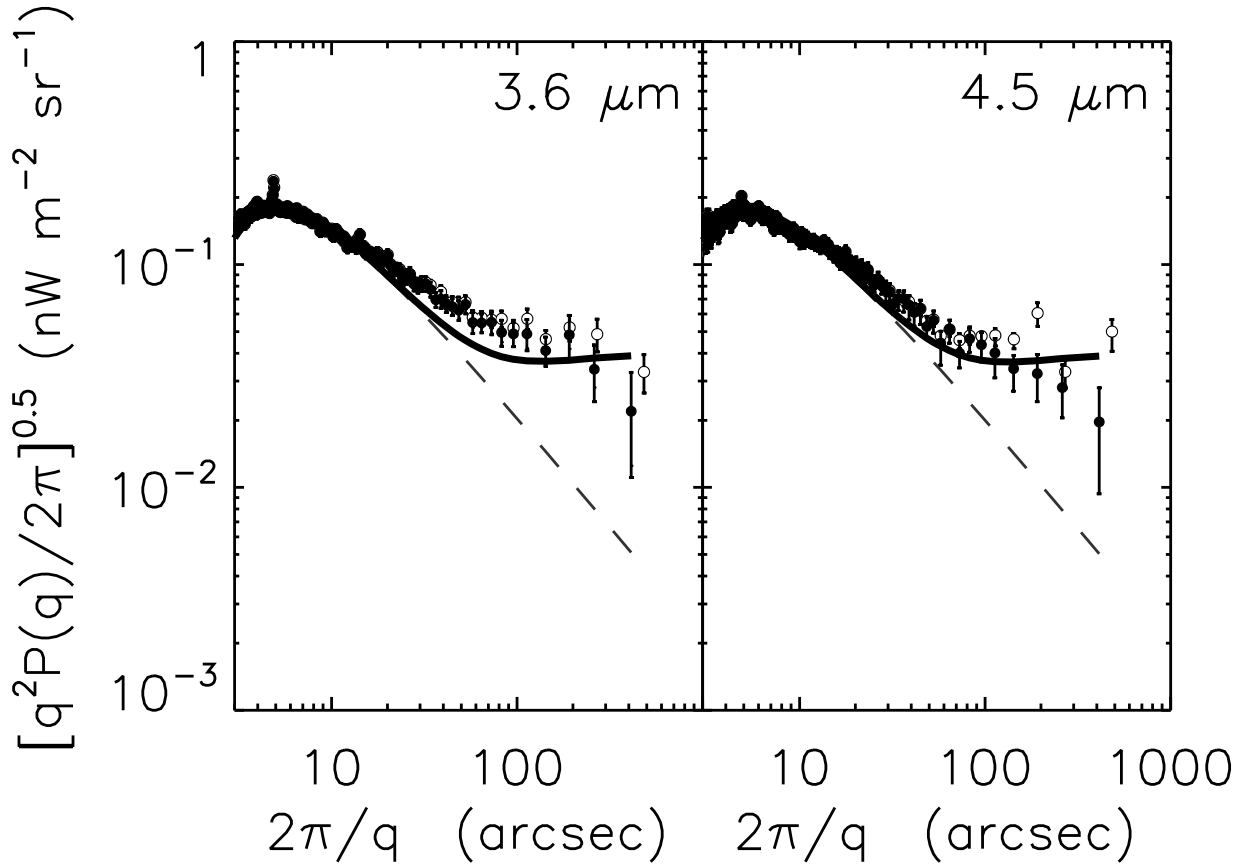


Fig. 36.— Average power spectra for the four source-clipped and model-subtracted GOODS fields at 3.6 and 4.5 μm . The filled black circles indicate results when power along the Fourier transform axes is excluded. The open circles indicate results when power along the Fourier transform axes is retained. Error bars correspond to 1- σ uncertainties. The dashed line indicates a fit to the shot noise at small angular scales. The thick solid line represents a simple model fit to the data assuming emissions originate at high z with the concordance ΛCDM model. The amplitudes of the large-scale component are identical at 3.6 and 4.5 μm indicating that the color of the arcminute-scale fluctuations is approximately flat. (See text for details.)

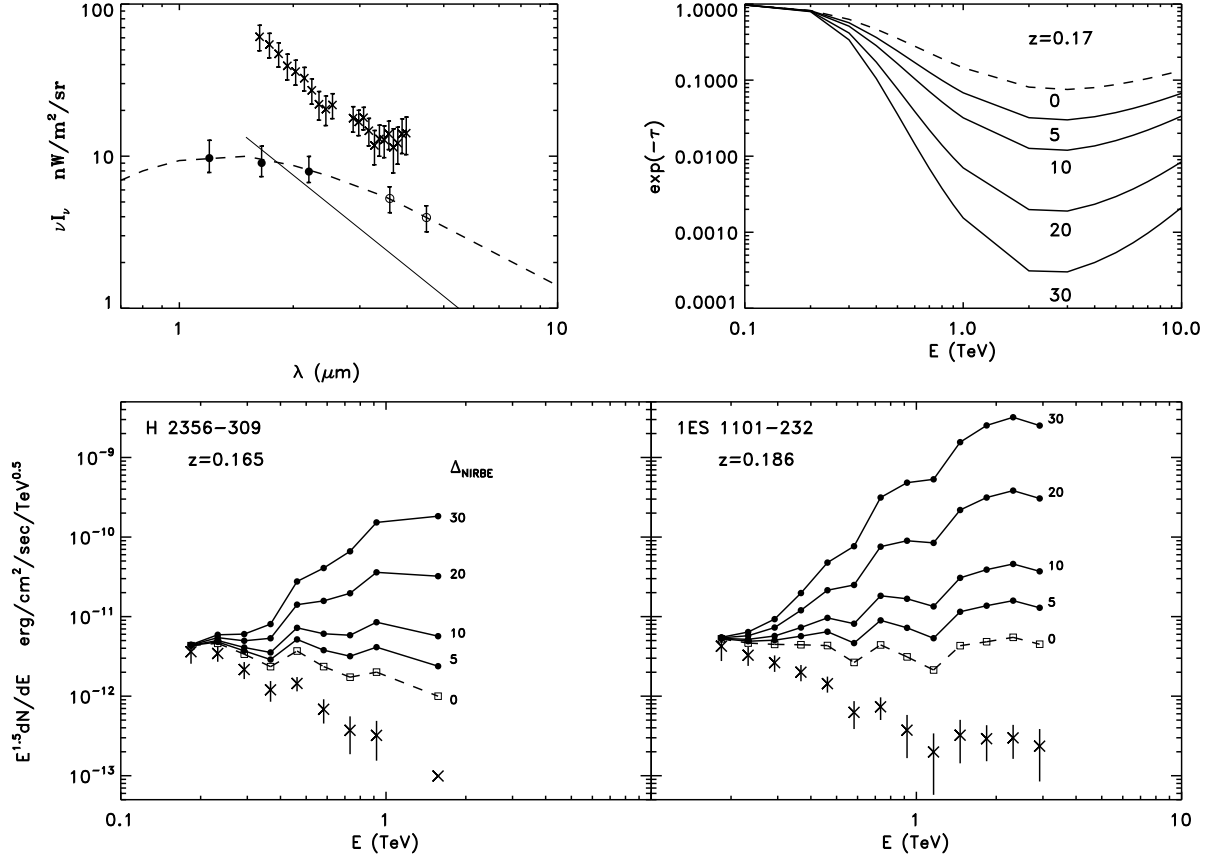


Fig. 37.— *Top*: (Left) Circles show the net observed fluxes from deep galaxy counts from Fig. 9 of Kashlinsky (2005a and references therein). Dashed line is the interpolated CIB from these galaxies used in the calculation. Crosses correspond to the *IRTS* measurements from Matsumoto et al. (2005). Solid line shows the modeled NIRBE from Pop III with $\nu I_\nu \propto \lambda^{-\alpha}$, $\alpha = 2$, and a Lyman cutoff, normalized to the integrated flux of $\Delta_{\text{NIRBE}} = 10 \text{ nW m}^{-2} \text{ sr}^{-1}$. (Right) Attenuation factor for a source at $z=0.17$ over the range of energies of HESS for CIB with the shown value of NIRBE from Pop III, Δ_{NIRBE} in $\text{nW m}^{-2} \text{ sr}^{-1}$. Note that at $z \simeq 0.2$ the most sensitive range for probing NIRBE is around 2 TeV. *Bottom*: HESS measured spectra for the two blazars (Aharonian et al. 2005) are shown with crosses. Open squares correspond to the intrinsic spectra in the absence of any NIRBE (dashed line in top left panel). Circles show the spectra corrected for additional absorption due to CIB photons produced at $z > 10$ and the NIRBE values shown near each line.

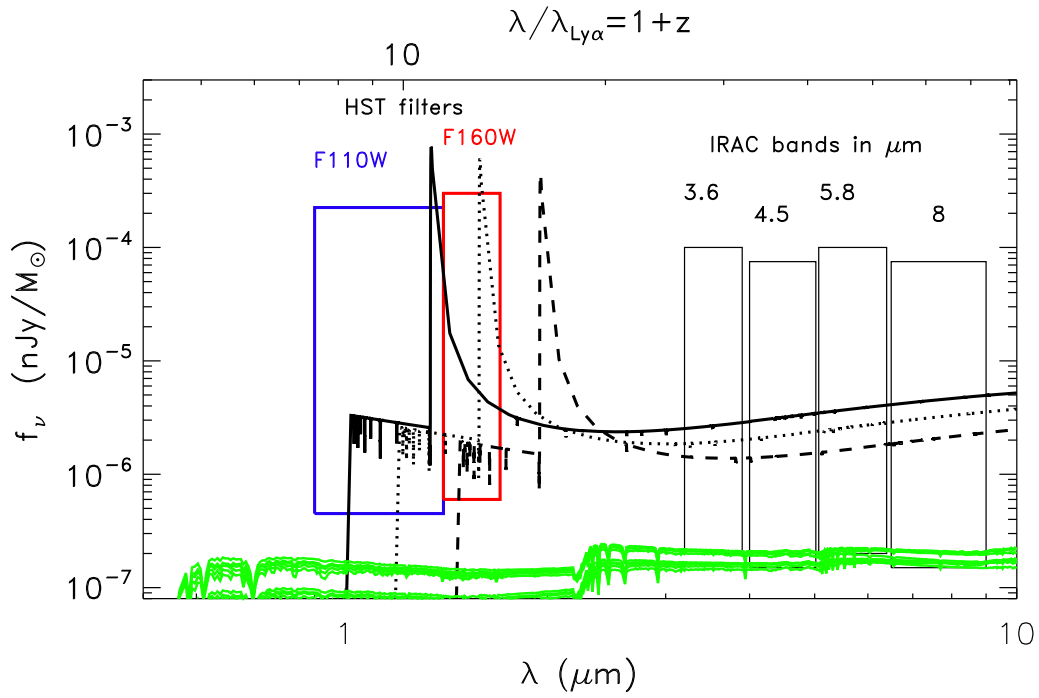


Fig. 38.— The spectra from Pop III systems are shown for $z=10$ (thick solid line), 12 (dotted) and 15 (dashed). The lines are drawn from Santos et al. (2002) for the case when processing of the radiation takes place in the gas inside the nebula. The *HST* and IRAC filters are shown. Green lines show the flux spectra for star-bursts at $z=5$ with the Salpeter-Scalo IMF and ages of 0.5 and 1 Gyr; the lines span metallicities from 0 to $5 \times 10^{-3} Z_{\odot}$.

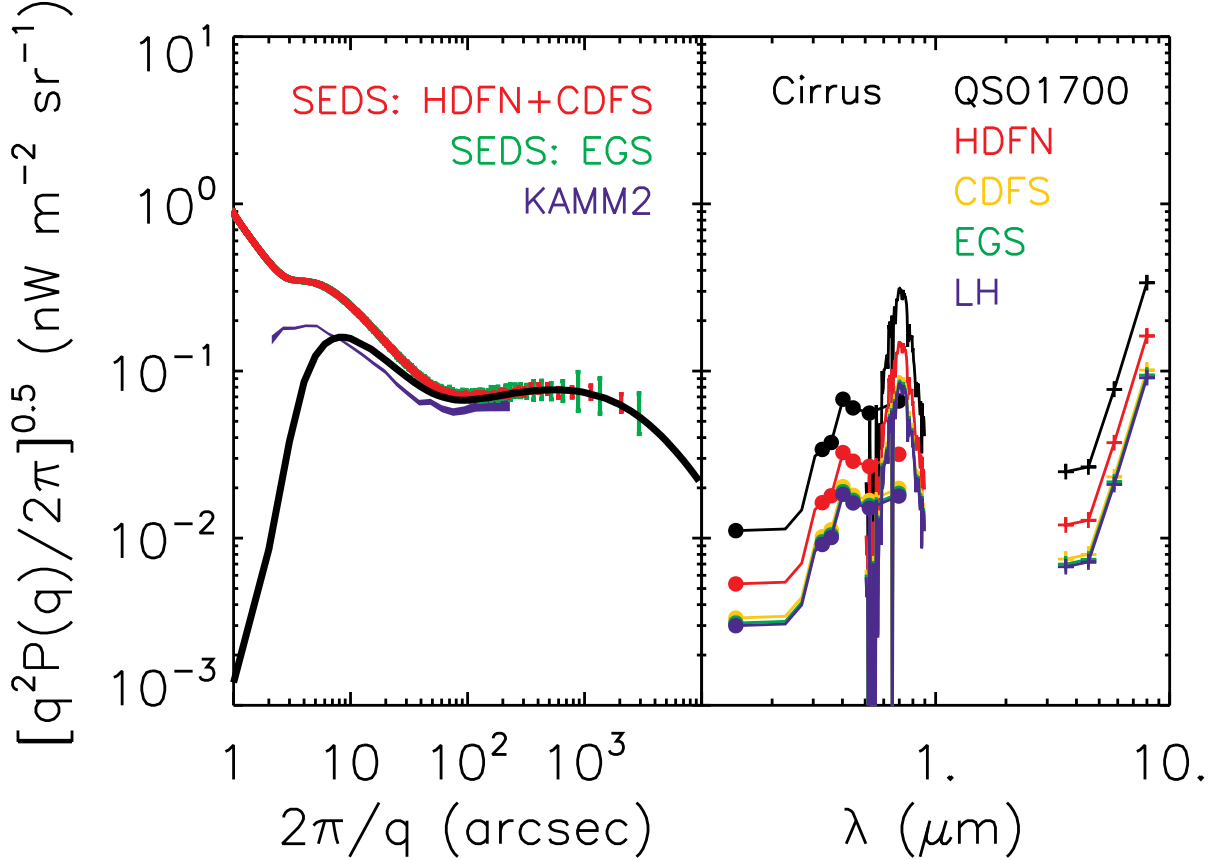


Fig. 39.— Expectations for measurements of CIB fluctuations at larger angular scales, and limitations due to interstellar dust. The left panel compares present CIB fluctuation measurements in the GOODS fields (blue line; KAMM2), with the expected results (red and green points with error bars) that may be obtained from the *Spitzer* SEDS project which will cover wider regions nearly as deeply. The larger fields should begin to reveal the $\sim 1000''$ peak in the fluctuation spectrum that is expected if the fluctuations are dominated by the first luminous stars in the Universe (black line). For several different fields characterized by different H I column density, the right panel shows the estimated noise level (expected to be nearly flat, or independent of q) due to thermal emission at IRAC wavelengths (adapted from Arendt et al. 1998), and due to extended red emission (ERE; Gordon et al. 1998) at $\sim 0.7 \mu\text{m}$. At shorter UV and visible wavelengths, scattered starlight becomes important (Leinert et al. 1998; Haikala et al. 1995; Mattila 1990; Guhathakurta & Tyson 1989; Toller 1981). The wavelength range from 1 - $5 \mu\text{m}$ is a window where minimal contamination by the ISM is expected.

Table 1. Background Fluctuation Data Sets

Field	Analyzed Field Size (arcmin)	Image Pixel Scale (arcsec)	Integration Time (hr)	Expected 3σ Sensitivity (AB mag)			
				$3.6\mu\text{m}$	$4.5\mu\text{m}$	$5.8\mu\text{m}$	$8\mu\text{m}$
GOODS ¹	9.7×9.7	0.6	~21	26.9	26.1	24.0	23.8
QSO 1700	11.5×5.1	0.6	~ 7.8	26.3	25.6	23.5	23.3
EGS ²	12.8×7.7	1.2	1.4	25.4	24.7	22.6	22.4
FLS	108×108	1.2	0.017	22.3	19.4	20.0	19.9

¹HDFN-e1, HDFN-e2, CDFSe-1, CDFS-e2

²“patch 4”, epoch 2

Table 2. Background Analysis Checks

Issue	Test	Result	Reference
1. Excess power on preferred axes?	Compare power spectra before and after blanking axes	Ignoring power on the FFT axes can mitigate artifacts	Fig. 2, §3.2
2. Self-calibration effectiveness?	Compare different channels Compare to GOODS processing	Self-calibration does remove some artificial patterns	Figs. 3-6, §4.1
3. Optimal depth for resolved source models?	Check residual skewness and correlation with model	Zero skewness is most robust and simplest criterion	Figs. 7-13, §4.2
4. Correct PRF for resolved source models?	Test with modified PRFs	PRF at $4.5\mu\text{m}$ may be slightly too sharp, but not a problem	Fig. 14, §4.2
5. Sensitivity to clipping fraction?	Alter clipping masks and add random clipping	Little sensitivity to variation of masked area	Figs. 17-20, §4.2
6. Results related to dither pattern?	Calculate power spectrum of dither pattern	Very unlike power spectrum of residual intensity	Fig. 22, §4.3
7. Results related to dither pattern + calibration?	Calculate power spectrum of dithered detector offset	Calibration errors would yield distinct large scale power	Fig. 23, §4.3
8. Results related to foreground sources and mask?	Calculate power spectrum of foreground sources, mask, “halo” image	Test power is too flat, or too weak to produce observed large scale power	Figs. 24-29, §4.3
9. Similar results in different fields?	Compare parameterized fits to different power spectra	Large scale power has similar shape in different fields, but scales with shot noise (depth)	Figs. 30-35, §5 Tables 3-5
10. Similar structure at different wavelengths?	Calculate cross-correlation coefficients and colors	Significant correlation and constant color indicate celestial origin at 3.6 and $4.5\mu\text{m}$	KAMM1
11. Possible zodiacal light structures?	Constrain by re-observation at different epochs	Indicates that fluctuations in zodiacal light are smaller than those in the observed background	KAMM1
12. Possible ISM (cirrus) structures?	Constrain by observations of regions at various H I column density	ISM could dominate large-scale fluctuations at $8\mu\text{m}$, but should be unimportant at shorter λ	KAMM1

